UNIVERSIDAD NACIONAL DE COLOMBIA

NUMERICAL EVALUATION OF CONCRETE TIME-DEPENDENT EFFECTS ON URBAN COFFERDAMS

Dumas Alejandro Aguirre Molina

Universidad Nacional de Colombia

Facultad de Minas, Departamento de Ingeniería Civil

Medellín, Colombia

2017

NUMERICAL EVALUATION OF CONCRETE TIME-DEPENDENT EFFECTS ON URBAN COFFERDAMS

Dumas Alejandro Aguirre Molina

Research thesis presented as partial requirement to obtain the title of:

Magister of Science – Geotechnics

Director:

David G. Zapata-Medina, Ph.D.

Codirector:

Luis G. Arboleda-Monsalve, Ph.D.

Research line:

Urban excavations

Universidad Nacional de Colombia

Facultad de Minas, Departamento de Ingeniería Civil

Medellín, Colombia

2017

To my beloved son Alejandro Aguirre, inspiration,
strength and hope of my life.

Acknowledgments

First of all, I want to express my greatest gratitude to my God, for giving me health and strength to successfully reach my magister degree. I want to especially thank my research director, Professor David G. Zapata Medina, for giving me since my arrival at the Faculty of Mines his invaluable knowledge, time and dedication, his advice to define priorities helped me to focus on academic activities and make possible the completion of this research.

I would also like to express my gratitude to Professor Luis G. Arboleda Monsalve for his research orientation and support in decision-making, mainly for the technical resources invested and for giving me the opportunity to work with my research colleague Felipe Uribe, his help was very important for the understanding of the project.

Thanks to my beloved mother Luz Patricia Molina and my brother Jonathan Aguirre, for always believing in me, their words of encouragement helped me to get up in crucial moments. In a very special way to my darling girlfriend Laura Castiblanco, who patiently endure my strenuous study and work schedules during 4 years, his wonderful company, his unconditional help and above all his true love were my support in this difficult path.

I also want to thank my classmates Jaime Mercado, Carellys Vergara and Alejandro Velásquez with whom I spent countless hours of academic work, I admire and value them. Finally, and no less important, I want to thank my friends and colleagues, Daniel Valencia and Leonardo Herrera for their constant support.

Abstract

Current construction methods for high-rise buildings combine a temporary cofferdam structure with top-down excavation techniques. The cofferdam allows the construction of the building rigid concrete core foundations in deep competent soil. In urban areas, excavation-induced ground movements must be controlled to protect adjacent infrastructure. Typically, urban cofferdams limit ground deformations via circular ring beam bracings made of either steel profiles or cast-in-place reinforced concrete. Concrete ring beams are nowadays becoming popular as they are directly placed in contact with the sheet piles, eliminating potential gaps between the lateral bracings and the retaining wall, and presumably reducing the amount of excavation-induced ground deformations. This research work presents a parametric study to evaluate time-dependent effects in an urban cofferdam braced with reinforced concrete ring beams. This is the first time where a fully couple numerical approach, considering aging, creep and shrinkage effects in the concrete along with advanced constitutive soil models to adequately represent consolidation and non-linear soil behavior, is presented. The parametric study is based on a numerical model calibrated and validated against field performance data collected during the construction of an urban cofferdam braced with seven reinforced concrete ring beams. The numerical approach proposed in this work allowed to isolate concrete time-dependent effects and the impact of related construction activities. It was found that aging effects were the most important concrete time-dependent component in the cofferdam performance. Aging induced-deformations for the considered case represent about 15% of the total horizontal displacements as calculated from the base model. Creep and shrinkage effects contribute around 6 and 3 %, respectively.

Keywords: Excavations, cofferdams, reinforced concrete, creep, shrinkage, aging, time-dependent effects, numerical modeling.

Resumen

Los métodos de construcción actuales para rascacielos combinan un cofferdam como estructura temporal con técnicas de excavación ascendente-descendente. Los cofferdam permiten la construcción del núcleo rígido de concreto de las fundaciones del edificio en suelo competente profundo. En áreas urbanas, deformaciones en el suelo son inducidas por excavaciones, las cuales deben ser controladas para proteger infraestructuras adyacentes. Típicamente, los cofferdam urbanos limitan deformaciones en el suelo mediante sistemas de arrostramiento de vigas circulares de acero o de concreto reforzado armado en sitio. Vigas circulares de concreto se están haciendo cada día más populares ya que quedan en contacto con las tablestacas, eliminando potenciales holguras entre el arrostramiento lateral y el muro de contención, y presumiblemente reduciendo la cantidad de deformaciones inducidas en el terreno por la excavación. Este trabajo de investigación presenta un estudio paramétrico para evaluar los efectos dependientes del tiempo en un cofferdam urbano arriostrado con vigas circulares de concreto reforzado. Esta es la primera vez que se presenta un enfoque numérico completamente acoplado, que considera los efectos de maduración, fluencia y contracción en el concreto, junto con avanzados modelos constitutivos del suelo para representar adecuadamente la consolidación y comportamiento no lineal del suelo. El estudio paramétrico está basado en un modelo numérico calibrado y validado con datos y mediciones de campo recopilados durante la construcción de un cofferdam urbano arriostrado con siete vigas circulares de concreto reforzado. El enfoque numérico propuesto en este trabajo permitió aislar los efectos dependientes del tiempo en el concreto, y la influencia de actividades de construcción relacionadas. Se encontró que el componente de la maduración en el concreto es el de mayor importancia en los efectos dependientes del tiempo para el desempeño del cofferdam. Las deformaciones inducidas por maduración para el caso considerado representan alrededor del 15 % de los desplazamientos horizontales calculados a partir del modelo base. Los efectos de fluencia y contracción contribuyen alrededor del 6 y 3 %, respectivamente.

Palabras Clave: excavación, cofferdams, concreto reforzado, fluencia, contracción, maduración, efectos dependientes del tiempo, modelación numérica

Table of Contents

List of figures

Pag.

List of tables

Pag.

1. INTRODUCTION

During the past decades, urban growth population has increased exponentially. About 55 percent of the world population are nowadays concentrated in urban centers, and it is expected that 70 percent of the world population will be urban by 2050 (United Nations 2007). Consequently, development land in crowded cities has become very limited and expensive, a trend that is expected to continue. The increasing demand for real estate has led to the use of the underground space and the construction of high-rise buildings to maximize square footage. This is the case of cities like New York, San Francisco, Los Angeles and Chicago among others, where natural barriers such us oceans, lakes, mountains or rivers precluded the city expansion.

Current construction methods for high-rise buildings combine a temporary cofferdam structure with top-down excavation techniques. The cofferdam is built following a bottom-up sequence using sheet piles as the retaining wall. The main purpose of the temporary cofferdam is to allow the construction of the building rigid concrete core in deep competent soil. The building basement area is then constructed using a top-down methodology propping a perimeter slurry wall with the basement floor slabs. From the project planning perspective, this method presents significant benefits in construction times as the main excavation activities are removed from the critical path of the construction project (Puller 1998; Finno et al. 2014)(Arboleda-Monsalve et al. 2017). However, it also has some disadvantages as additional ground movements related to the inherent nature of the cofferdam construction are generated.

When using deep excavations in urban areas, excessive excavation-induced movements are a major concern. This is because they can lead to significant displacements and rotations in adjacent structures causing damage or the possible collapse of such structures. Therefore, accurate predictions of lateral wall deflections and surface settlements are important design criteria in the analysis and design of excavation support systems. Usually, the design of high-rise buildings combining a

temporary cofferdam structure with a main top-down excavation does not consider the ground movements induced by the cofferdam construction due to the temporary nature of the cofferdam structure. Recently, Arboleda et al. (2017) presented the performance of two cofferdam case histories built in similar geological conditions. One cofferdam employed segmental steel ring beams as bracing system while the second used reinforced concrete ring beams. The performance data showed that cofferdam construction-induced movements can be significant. Arboleda et al. (2017) also described the construction issues that affected their performance, some of which are related to the inherent nature of the cofferdam construction. Among them are the slack in the sheet pile interlock connection, the coupling between steel ring beams and the perimeter sheet pile wall, and concrete time-dependent and temperature effects when concrete ring beams are used.

This research work uses the data presented by (Arboleda-Monsalve et al. 2017) to numerically evaluate time-dependent effects in an urban cofferdam braced with reinforced concrete ring beams. This is the first time where a fully couple numerical approach, considering aging, creep and shrinkage effects is the concrete along with advanced constitutive soil models to adequately represent the non-linear soil behavior, is presented.

1.1 Statement of the Problem

Cofferdams are conventionally defined as temporary offshore structures mostly used for land reclamation purposes. The typical design of cofferdams is mainly based on methods of limit equilibrium. For external stability, overturning, slippage, bearing capacity and seepage modes of failure are evaluated. For internal stability, the design checks structural solicitations in the different elements of the system. When cofferdams are built in urban areas, excavation-induced ground movements must be controlled to protect adjacent infrastructure. Typically, urban cofferdams limit ground deformations via circular ring beam bracings that provide strength and stiffness to the structure. Typically, segmental steel ring beams have been chosen over cast-in-place reinforced concrete ring beams as steel elements can be rapidly installed speeding up the cofferdam construction. For cast-in-place reinforced concrete ring beams, enough curing time must be allowed before the excavation can proceed (Puller 1998). However, they potentially reduce the amount of excavation-induced ground deformations as they are directly placed in contact with the sheet piles, eliminating potential gaps between the lateral bracings and the retaining wall.

Traditional design methods for excavation-support systems usually neglect time-dependent effects when evaluating their performance and impact on adjacent infrastructure. Additionally, variations in environmental conditions, such as temperature and relative moisture, make construction conditions differ from those assumed during the design process. (Arboleda-monsalve et al. 2015), using a SAP2000 three-dimensional finite element model and field performance data, studied concrete time-dependent effects on a 5-level top-down excavation propped with concrete floor slabs. (Arboleda-monsalve et al. 2015) reported that about 30% of the total horizontal displacements recorded during the excavation construction were caused by creep, shrinkage and aging, with shrinkage being the most important effect in terms of deformation contribution.

More recently, Arboleda et al. (2017) presented the performance of an anonymous cofferdam project located in the city of Chicago, IL and braced with seven reinforced concrete ring beams. It was used as a temporary structure to allow the construction of the rigid concrete core of a 610-m-high skyscraper in deep competent soil. The cofferdam had a depth of 23 m and a diameter of 33.2 m. Its construction began in December 2007 and partially ended in January 2008. The seasonal variations induced very low curing temperatures in the concrete during the cofferdam construction. Additionally, the field records show accelerated cycles of excavations. These effects, added to the inherent time-dependent nature of the concrete, had a direct impact on the cofferdam performance. However, their quantification, solely based on performance data, is very difficult as the recorded deformations include the coupled effects of soil non-linearity, soil consolidation, concrete time-dependency, variations of temperature, maturity and excavation sequence.

The detailed case history data presented by Arboleda et al. (2017) and the latest implementation in Plaxis b.v. of advanced concrete constitutive models that can account for time-dependent strength, stiffness, creep and shrinkage [e.g. the shotcrete model by (Schädlich and Schweiger 2014a)] present a unique opportunity to evaluate and quantify the aforementioned effects.

1.2 Objectives of the Research

The main objective of this research is to numerically evaluate and quantify time-dependent effects on the performance of urban cofferdams braced with reinforced concrete ring beams.

The specific objectives of this work included:

- Evaluate the field performance of an anonymous cofferdam located in Chicago, IL and braced with concrete ring beams. Performance data includes inclinometer measurements, construction sequencing, temperature records, subsoil exploration and concrete compressive strength tests.
- Define constitutive parameters for the Hardening Soil, Hypoplasticity Clay and Shotcrete models based on available soil characterization, temperature records and concrete compressive strength tests completed during the cofferdam construction.
- Establish procedures to calibrate the Shotcrete constitutive model parameters to accurately represent the concrete behavior for geotechnical applications.
- Create a numerical model of the cofferdam construction under axisymmetric conditions in the software Plaxis 2D including the coupled effects of concrete time-dependency and soil non-linearity and consolidation.
- Validate the numerical model with the measured performance of the cofferdam construction.
- Conduct a parametric analysis to isolate the effects of concrete aging, creep and shrinkage on the lateral displacements of cofferdam structures.

1.3 Relevance of Research

Excavation performance analysis and geotechnical modeling by means of finite element has extensively been treated in recent years (Gallant 2011)(Orazalin and Whittle 2014)(Sarabia 2012)(Zapata-medina 2012)(Arboleda-Monsalve et al. 2017), However, research works quantifying the effects of concrete time-dependency coupled with the non-linear behavior of the soil are a very scarce. This research shed some light in terms of quantifying the abovementioned effects and determining their contribution to the excavation-induced ground movements around urban cofferdams braced with concrete ring beams. This work also establishes procedures to calibrate the Shotcrete constitutive model parameters to accurately represent the concrete behavior for geotechnical applications.

For future excavation projects with similar conditions, this research will allow to prevent or foresee excessive excavation-induced ground deformations and possible damage to adjacent structures or nearby utilities. It will be reflected in safer excavation projects and considerable economical savings

typically expended in repairs and mitigation of excavation-induced damage to adjacent infrastructure.

1.4 Content of Thesis

Chapter 2 of this document presents technical background related to urban cofferdam and concrete time-dependent effects. Initially, the cofferdam definition and fundamental concepts are presented. Then, the case of an urban cofferdam at an anonymous site is summarized. Subsequently, a complete review of methods to evaluate concrete time-dependent effects (i.e., aging, creep and shrinkage) is presented. Finally, the theoretical principles and controlling parameters of the constitutive models used in this research to represent the non-linear soil and concrete behavior are included.

Chapter 3 presents, in detailed manner, the numerical analysis of the construction of an urban cofferdam located at an anonymous site in Chicago, IL. The assumed geotechnical characteristics, concrete time-dependent parameters and construction sequence are fully described. The results are compared with performance data obtained during construction and presented in terms of lateral displacements and excess pore water pressures.

Chapter 4 presents the results of a parametric study completed to isolate and quantify the concrete time-dependent effects on the cofferdam performance.

Chapter 5 summarizes this research and presents conclusions and recommendations.

2. TECHNICAL BACKGROUND

2.1 Cofferdams

Urban cofferdam is defined as a temporary structure which is constructed with sheet piles and an internal bracing support system, which provide lateral retention of earth, and avoid the passage of fluids to the work place. The sheet piles are placed in place with an impact hammer or vibratory pile driver, and the bracing support system is usually placed as the excavation progresses, typically steel or concrete ring beams. Originally its application was in coastal areas, where it was sought to prevent the passage of water to the work area inside the cofferdam, and also to gain work area above the water level by filling with granular material the inside of the cofferdam, see **Figure 2-1**. The word "cofferdam" comes from "coffer" meaning box, indicating a dam in the shape of a box (Nemati 2005).

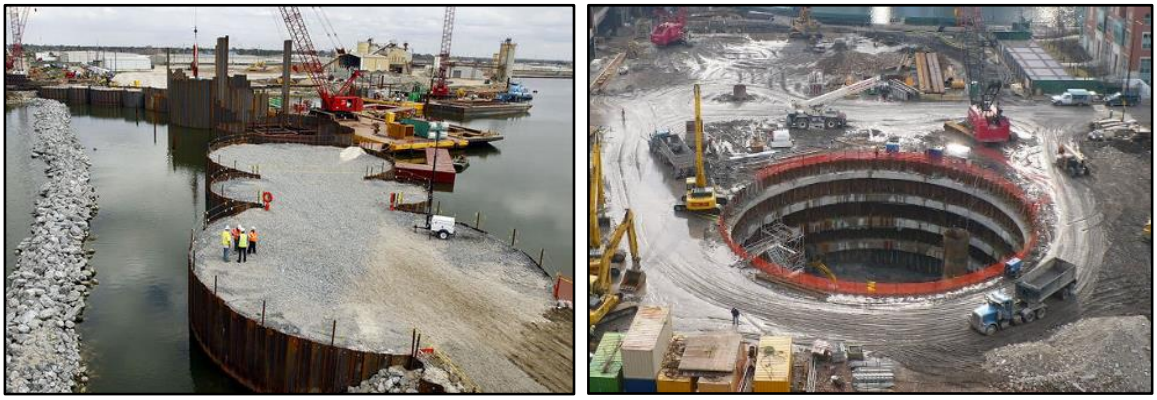

Figure 2-1. Original (Manitowoc 2017) and current cofferdam applications.

Cofferdam design is a structure, soil and water interaction problem, consequently, the imposed loads by hydrostatic or hydrodynamic forces due to flow generated when modifying the pressure heads in the system. Additionally, surcharges applied to the cofferdam by construction equipment such as cranes, drilling rigs or operation equipment should be considered in the analysis models, from the

beginning of the installation of the sheet piles to the construction of the brace systemin support. (Clough and Kuppusamy 1985) report cofferdam analysis based on field instrumentation in the Lock and Dam 26 Mississippi River project, the observed performance led them to propose procedures based on 2D finite elements in axisymmetric, vertical-slice and plane-strain conditions to approximate the behavior of these structures, see **Figure 2-2**.

In these pioneering models in geotechnical engineering, to capture the stress-strain response the incremental nonlinear constitutive model of hyperbolic relation (Duncan et al. 1980) was used, with which they obtained results consistent with the observed trends. Problem associated with orthotropic stiffness were identified by strain gage in the field instrumentation program and tensile tests on an interlocked PSX-32 sheet pile, see **Figure 2-3** related to the natural slack in the interlocks of sheet piles that generate a non-linear early tension behavior in sheet piles due to the development of initial tension (Clough and Kuppusamy 1985), which lead to additional lateral deformations in the cofferdam. Elastic bilinear springs were implemented in the interlocks under the concept E-ratio, which allowed to simulate the reduction of horizontal stiffness, results that were compared with the observed performance were obtained.

Current research continues to try to solve this problem of interaction between sheet piles, (Uribe-Henao and Arboleda-Monsalve 2016) implemented multilinear link elements to model the interlocks, which allow to model translational and rotational stiffness in the axial and bending plane. the stiffness properties associated with these elements correspond to those of the interlock filling material, material that arrives there during the installation process, to get specific information on this topic, refer to (Uribe-Henao and Arboleda-Monsalve 2016) and (Gallant 2011), who conclude that this effect has a great impact on the performance of the cofferdam. Also can be consulted , (Wissmann et al. 2003) and (Schmieg and Vielsack 2002) for more information about connection between sheet piles.

The vast majority of academic literature consulted, reports case studies of cofferdam applications in marine environments, application that as already explained requires the filling of the cofferdam, subjecting the sheet piles interlocks to tension forces. Contrarily, little information has been found about the use of cofferdam in urban environments, which are the focus of this research, however, recently (Arboleda-Monsalve 2014) reports the case of the OMPW excavation in the city of Chicago as one of the most studied cases due to the wealth of soil information, structural elements and records of field instrumentation, which considered inclinometers, piezometers and settlement control points.

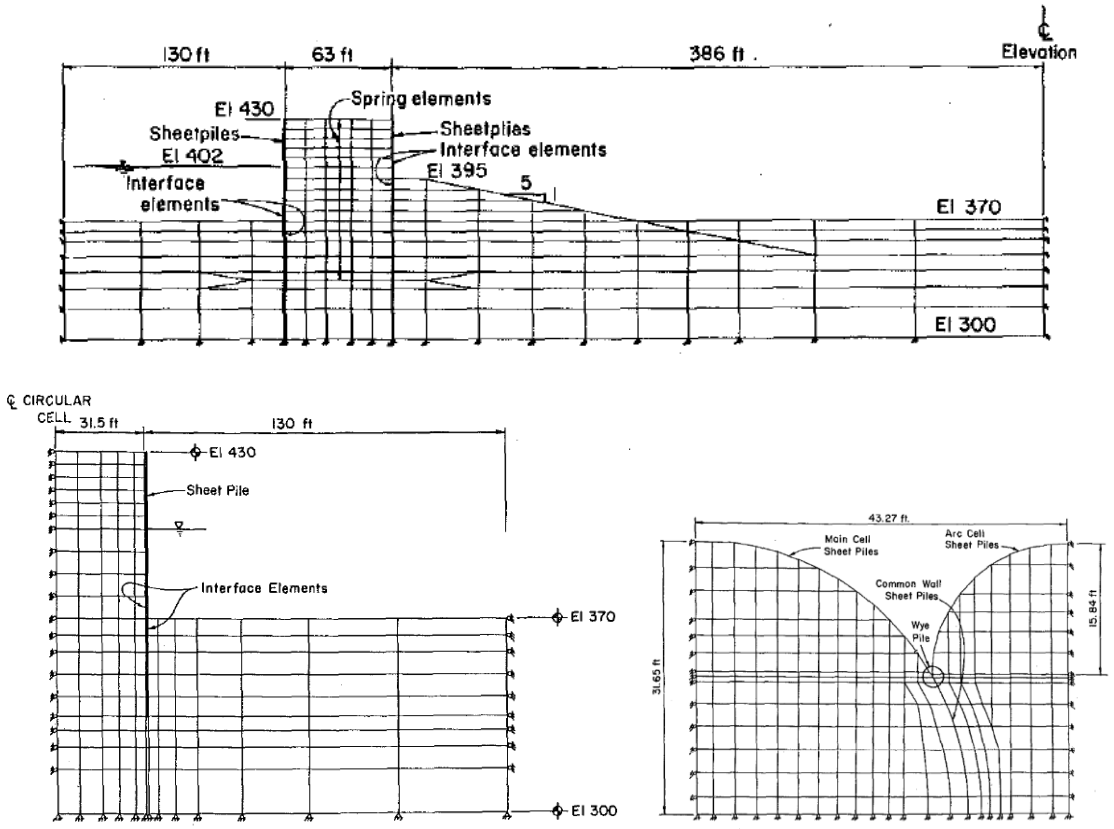

Figure 2-2. Axisymmetric, vertical-slice and plane-strain element finite 2D models. Taken from (Clough and Kuppusamy 1985)

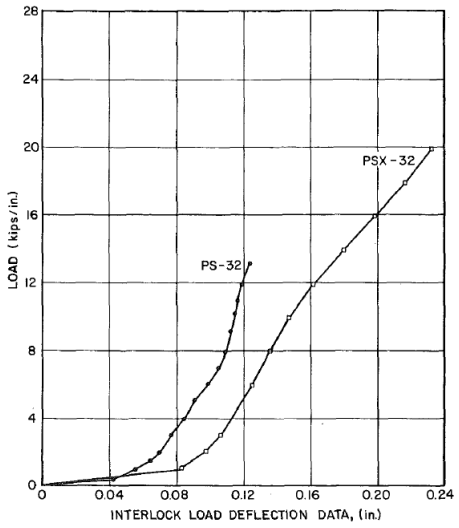

Figure 2-3. Translational stiffness of and interlocked PS-32 and PSX-32 sheet pile. Taken from (Clough and Kuppusamy 1985)

2.2 Performance of Urban Cofferdam at Anonymous Site

2.2.1 Site Specifications

The research site is located in downtown Chicago. The project consists on the construction of a 610-m high structure, which in its architectural design contemplates eight levels of parking garage. This project had as a critical route the construction of the central concrete core, so that an urban cofferdam was built, which allowed to excavate to a suitable depth for construction of the foundation system.

2.2.2 Site Geology and Stratigraphy

According to (Peck, 1954) Chicago's soil consists on a great clay mass deposited during geological age through the ice cover extended on the continent; is common to find in some localities clay layers covered by sand layers, which were deposited when Michigan Lake extended over Chicago area. Clay layers are found stratified defining advance series and glacier retreat; until now, in this area six (6) advance series have been identified, and glacier front retreat.

Surface geological conditions generally consist on sand deposits underlies by a first layer of rigid clay which generates a crust over softer clay layers. However, the stiffness of these layers tends to increase with depth until the bed rock. These soft clays have generally a thickness of 30 feet and consist on successive layers of Tilitas (Till), which are defined as unclassified glacial sediments, until reaching the rocky mantle which consists on a sedimentary rock named Niagaran Limolite (The Niagaran Limestone).

The last period of the Pleistocene age was characterized by several climatic changes and continental ice cover processes, of which there is evidence of backward and advance movement in the north of the United States of at least four great glaciers. The most recent glacier known as Wisconsin left deposits of sufficient thickness to be treated as important at the moment of making foundation designs in Chicago area. The Wisconsin Glacier was conformed by four stages, of which Cary sub stage was identified on the Chicago area, this stage consists on the deposition of six layers of Till: Valparaiso, Tinley, Park Ridge, Deerfield, Blodgett and Highland Park, see **Table 2-1**. Each one represents an advance and retreat step in the front of the glacier, identified from its terminal moraines.

Table 2-1. Consistency and texture of clay in Till layers. (Adapted from table 2 (Peck, 1954))

Till layer	Compressive strength[kPa]	Texture
Valparaiso	1053.37	Stratified gravelly Till with extreme lateral variability.
Tinley	95.76– 1053.37	Gravelly, clayey silty Till.
Park Ridge	172.37 – 335.16	Sandy clay Till with numerous sand and silt seams.
Deerfield	33.52 – 100.55	Uniform clay Till except for stratification near base.
Blodgett	19.15 – 57.46	Complex deposit of clay Till, silt and lacustrine clay.
Highland Park	95.76 – 1053.37	Stony clay Till, pockets of sand and gravel.

Figure 2-4 shows the local stratigraphy, where the soil profile is formed by a layer of an urban fill that was found on the surface was uncontrollably executed with the debris coming from the great fire of the city of Chicago in 1871 (Arboleda-Monsalve 2014). This layer is located from +2.40 to +0.80 CCD. Then there is a large layer of loose to dense sands from +0.80 to -7.60 CCD. Underlying these sands is the Wisconsin Glacier, where the soft clay layer (Blodgett) is found from -7.60 to -10.60 CCD and then the medium clay layer (Deerfield) from -10.60 to -14.90 CCD. Underlying these layers is the stiff clay (Park Ridge) layer that takes place from -14.90 to -20.20 CCD. Finally, the hard clays layer (Tinley and Valparaiso) are presented from -20.20 to -30 CCD.

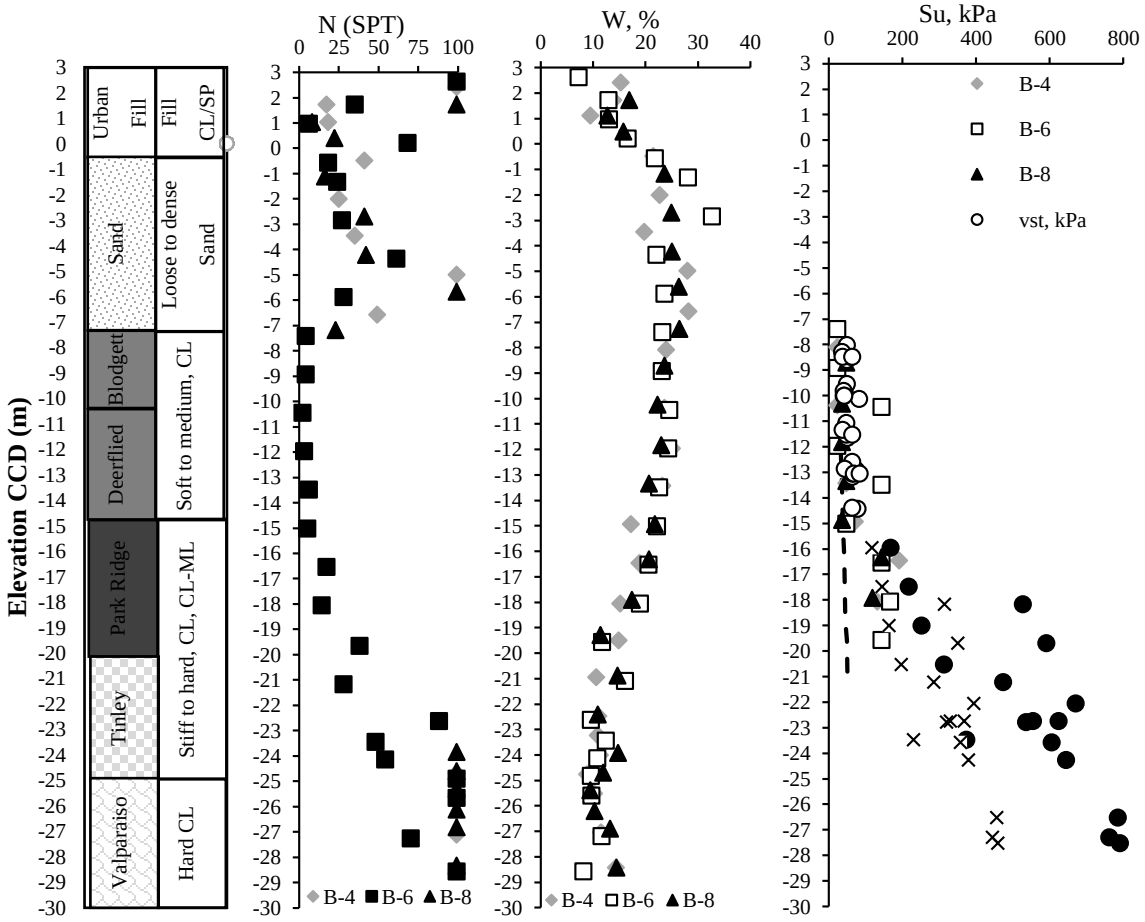

Figure 2-4. Local profile Stratigraphy

2.2.3 Groundwater Conditions

In Chicago city, the groundwater conditions are strongly altered by Michigan lake and the construction of the deep tunnel of Chicago (Sarabia, 2012). Due to the construction of the tunnel and the pumping system, a decrease in the total hydraulic head at the top of the rock formation has been generated. The tunnel system is located approximately 100 m below the city street level and part of this system runs under the Chicago River. In the vicinity between lake Michigan and the branches of the deep tunnel of Chicago there is an almost constant head of water of -14.5 m CCD. This hydraulic head was identified by measurements of water levels in the upper strata of the bedrock. The sample presented in **Table 2-2** exposes a sampling that gives sustenance to a constant head of water which indicates that the bedrock water level has reached hydraulic equilibrium and it is in a steady state condition. Typical measurements of the phreatic surface made within the superficial urban fill material roughly coincide with the river or lake levels (0 to 1.5m CCD).

Table 2-2. Chicago bedrock ground water table elevation (Sarabia, 2012))

Location	Water Elevation, m CCD	Date
18th St. And Calumet Av.	-13.4	2004/09/27
111 Wacker Dr.	-15.2	1998
79 E Wacker Dr.	-14.7	2008/01/06
1 N Wacker Dr.	-14.5	1999
Roosevelt Rd. And Michigan Av.	-14.9	1997/01/11
79 East Wacker Dr.	-14.7	2005/06/14
300 N LaSalle St.	-14.1	2005/01/11

Figure 2-5 shows the measurements of pore pressures taken on the PB-7 and PB-11 piezometers installed in the project and additionally the measurements presented by (Sarabia, 2012). The pore pressures were obtained by measurements taken on vibration wire piezometers installed in the soft to medium clay layers. Materials that make up the typical laminate profile of Chicago. The downward seepage flow is identified by the deviation shown in the figure between the hydrostatic line of pore pressure and the measurement points in the field, Soldier Field, 14th, PB-7 and PB-11.

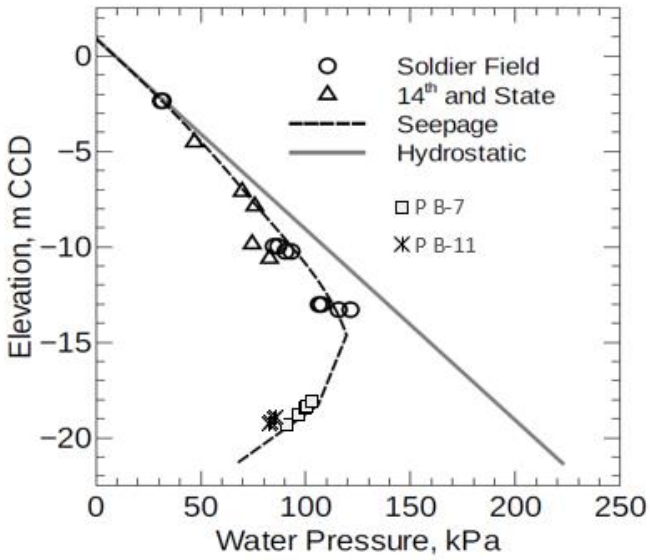

Figure 2-5. Pore water pressures measured at the project site (PB-7 and PB-11) and measurements from nearby projects (Sarabia, 2012).

2.2.4 Excavation Support System

In this project several systems of retaining walls and two modalities of excavation and construction were implemented. In the construction of the perimeter of the project it is planned to use the top-down technique that supports the retaining walls in the basement floor slabs and the types of retaining walls designed for the perimeter are called slurry wall, drilled pier wall, secant pile wall in the basement slabs, see **Figure 2-6**. The construction of a foundation system of the rigid core of the structure made up of 20 core caissons that cross great clay mass and reach the deep rocky limestone mantle, was defined as the starting point of the critical route for the project, consequently, it was possible to use a temporary cofferdam to reach the base level for the construction of the core caissons system. To evaluate the lateral ground movements throughout the excavation, an inclinometer was installed at NW side of cofferdam.

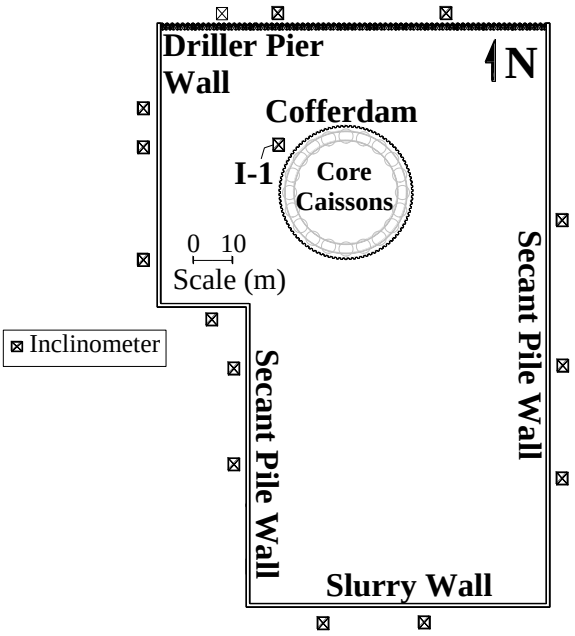

Figure 2-6. Plan view, inclinometer locations (Arboleda-Monsalve et al. 2017)

Interlocked modular pieces of PZ-27 steel sections conform the circular sheet pile wall with an internal diameter of 33.2 m, see **Figure 2-7**. The sheet pile wall driven to elevation -21m CCD (Chicago City Datum) is laterally supported with seven reinforced concrete ring beams, see **Figure 2-8**. As a vertical support to the rings was implemented a profile of steel AT, which was welded to a steel plate that once had a series of bolts welded, and as additional support had another series bolt welded to the sheet piles placed in position horizontal, see **Figure 2-9**. The ring beams were cast-in-place as the excavation proceeded and spaced every 3 m approximately.

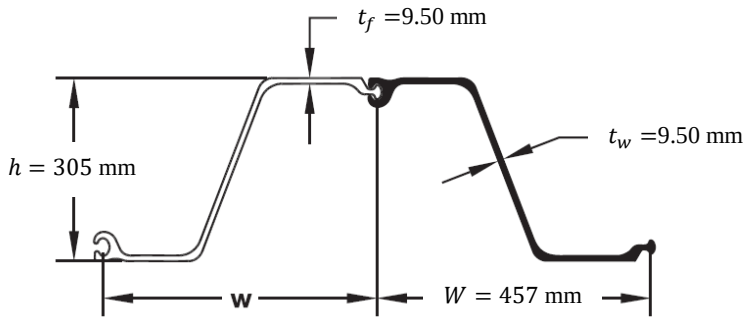

Figure 2-7. Technical specifications PZ-27 Hot Rolled Steel Sheet Pile (Taken and adapted from (Skylinesteel, 2017))

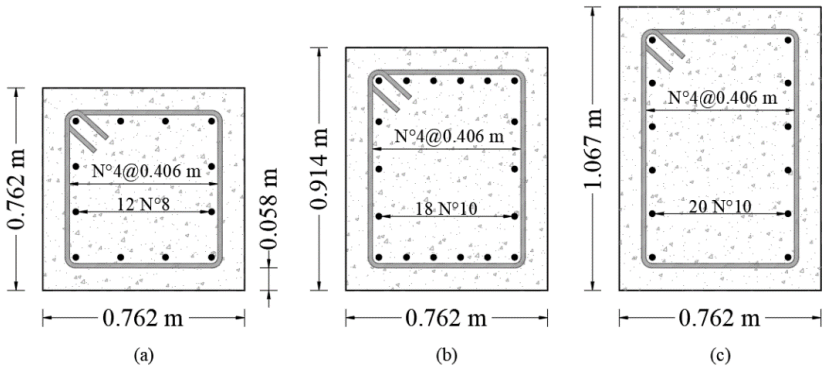

Figure 2-8. Ring Beams Cross section (a) Ring Beams 1-7, (b) Ring Beams 2-6 and (c) Ring Beams 3 to 5.

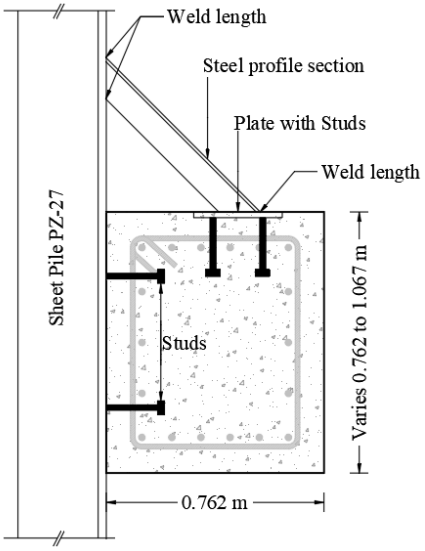

Figure 2-9. Ring beam support in cofferdam.

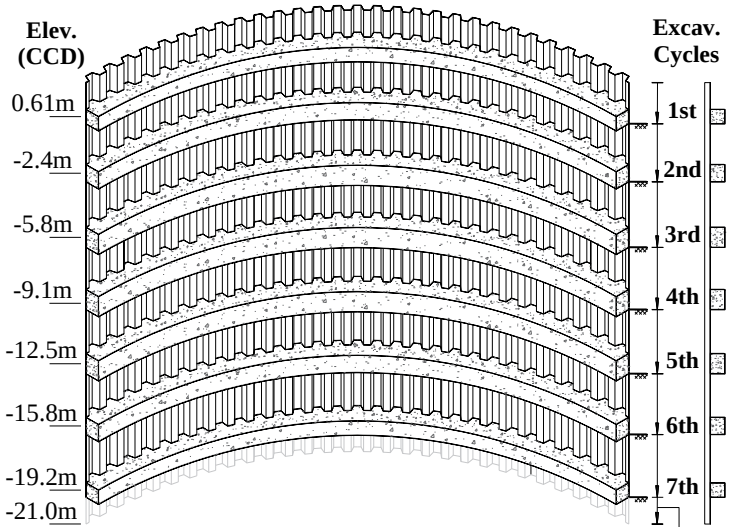

Figure 2-10. Urban cofferdam schematic elevation view (Arboleda-Monsalve et al. 2017)

The first level of bracing was cast at 0.60 m CCD (1.8 m below the ground surface), second level at -2.40 m CCD, third level at -5.80 m CCD, fourth level at -9.10 m CCD, fifth level at -12.50 m CCD, sixth level at -15.80 m CCD and the seventh and last at -19.20 m CCD, see **Figure 2-10**.

2.2.5 Staged Construction Sequence

The construction sequence was defined from inclinometer registers, concrete and excavation reports, and mainly from construction activities photography register. The last one allowed to adjust excavation times and depths of, which varied with respect to the construction works record. **Table 2-3** shows the estimated dates of each phase of construction of the cofferdam, according to the photographic record of the project.

A summary of the construction sequence containing the concrete casting dates of the rings and excavation dates is given in these dates show curing periods of 2 days after casting rings to initiate the excavation phase to the base of the underlying ring, in this way transmitting loading to the ring, which had not reached the design resistance. This accelerated cycle of soil removal and ring beam placement made that additional ground movements occurred (Arboleda-Monsalve 2017).

From **Figure 2-11** to **Figure 2-18** the photographic record of the project is presented, which was the key to understanding the construction of the cofferdam, along this one can observe the seasonal variations of the climate, a fundamental factor to analyze the time-dependent effects on the concrete rings.

Table 2-3. Time line construction

Stage Construction		Time line				Sequence	
		Intial	Final	Time		Start	End
#		mm/dd/yyyy	mm/dd/yyyy	Plaxis	day	day	day
1	**SPInst.**	12/10/2007	26/11/2007		46	1	46
2	**Ex-1**	26/11/2007	29/11/2007	7	4	46	49
3	**RB-1**	29/11/2007	3/12/2007	2	5	49	53
4		3/12/2007	7/12/2007	4	4	54	57
	Ex-2	7/12/2007	8/12/2007	1	1	58	58
		8/12/2007	9/12/2007	3	2	58	59
5	**RB-2**	9/12/2007	11/12/2007	2	3	59	61
6		11/12/2007	15/12/2007	4	4	62	65
	Ex-3	15/12/2007	17/12/2007	2	2	66	67
		17/12/2007	18/12/2007	5	2	67	68
7	**RB-3**	18/12/2007	26/12/2007	6	9	68	76
8		26/12/2007	30/12/2007	4	4	77	80
	Ex-4	30/12/2007	1/01/2008	2	2	81	82
		1/01/2008	3/01/2008	6	3	82	84
9	**RB-4**	3/01/2008	5/01/2008	0.1	3	84	86
10		5/01/2008	8/01/2008	2.9	3	87	89
	Ex-5	8/01/2008	9/01/2008	1	1	90	90
		9/01/2008	11/01/2008	5	3	90	92
11	**RB-5**	11/01/2008	14/01/2008	0.1	4	92	95
12		14/01/2008	20/01/2008	7.9	6	96	101
	Ex-6	20/01/2008	23/01/2008	3	3	102	104
		23/01/2008	25/01/2008	7	3	104	106
13	**RB-6**	25/01/2008	28/01/2008	0.1	4	106	109
14	**Caissons**	5/02/2008	13/08/2008	190.9	191	117	307
15	**Ex-7**	9/08/2008	10/08/2008	2.75	2	303	304
16	**RB-7**	13/08/2008	13/08/2008	0.25	1	307	307

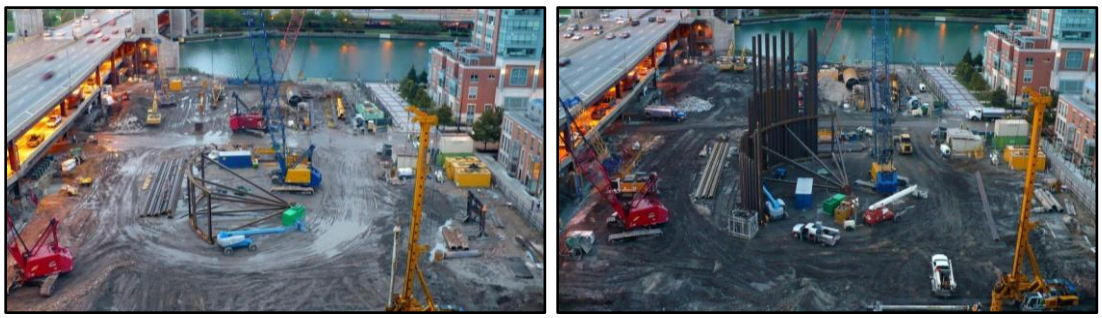

Figure 2-11. Installation of guides and sheet pile driving (from +2.4 to -21 CCD)

Figure 2-12. End of sheet pile driving and first excavation (from +2.4 to +0.219 CCD)

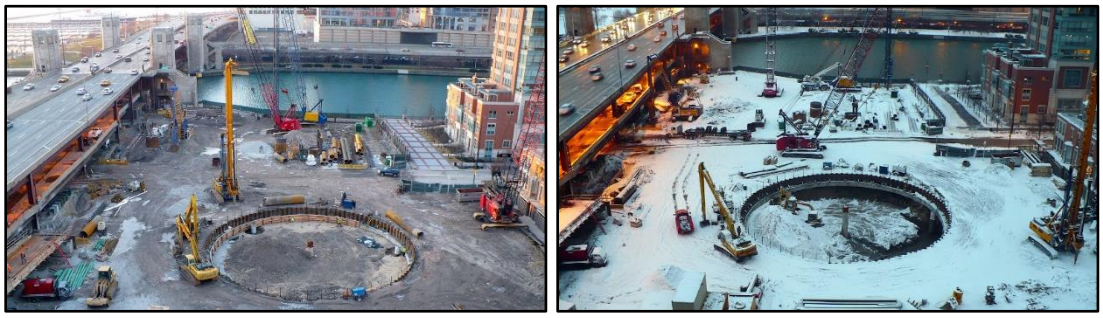

Figure 2-13. Castings concrete RB1 and Second excavation (from +0.219 to -2.857 CCD)

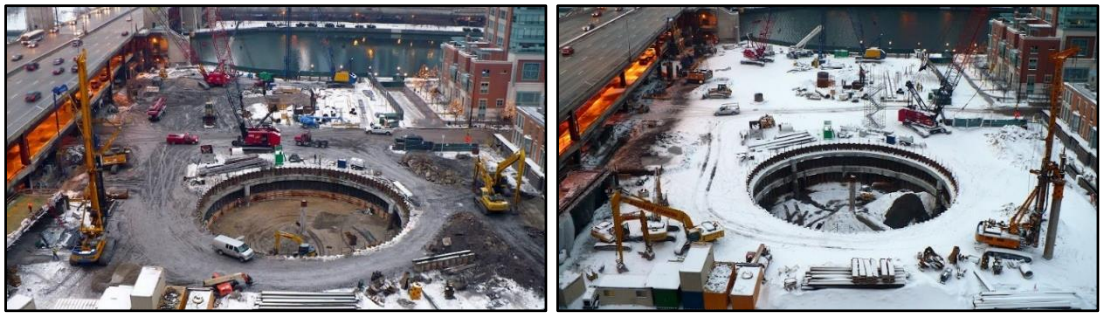

Figure 2-14. Castings concrete RB 2 and third excavation (from -2.857 to -6.333 CCD)

Figure 2-15. Castings concrete RB3 and fourth excavation (from -6.333 to -9.633 CCD)

Figure 2-16. Castings concrete RB4 and fifth excavation (from -9.633 to -13.03 CCD)

Figure 2-17. Castings concrete RB5 and sixth excavation (from -13.03 to -16.26 CCD)

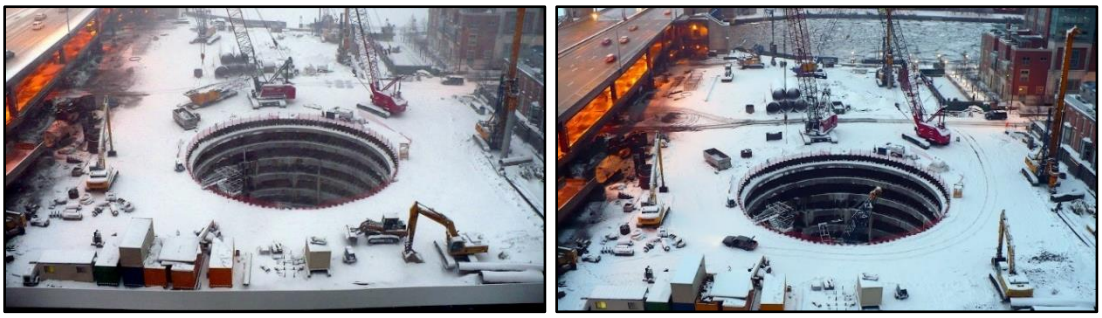

Figure 2-18. Castings concrete RB6 and caissons drilling.

2.2.6 Observed Performance

Figure 2-21 shows observed field performance data, soil stratigraphic and a cofferdam cross section with concrete ring beams elevation. Part a) presents construction sequence associated with excavation levels and cast-in-place concrete ring beams elevations. Part b) shows inclinometer I-1 registers installed in cofferdam perimeter, this inclinometer presents data fort all excavation stages. The construction sequence records show in detail the installation sheet piles time intervals and the successive excavation stages and cast-in-place concrete ring beams. Also, the incremental lateral displacement since la excavation 6 until cofferdam construction end and an additional time interval is presented.

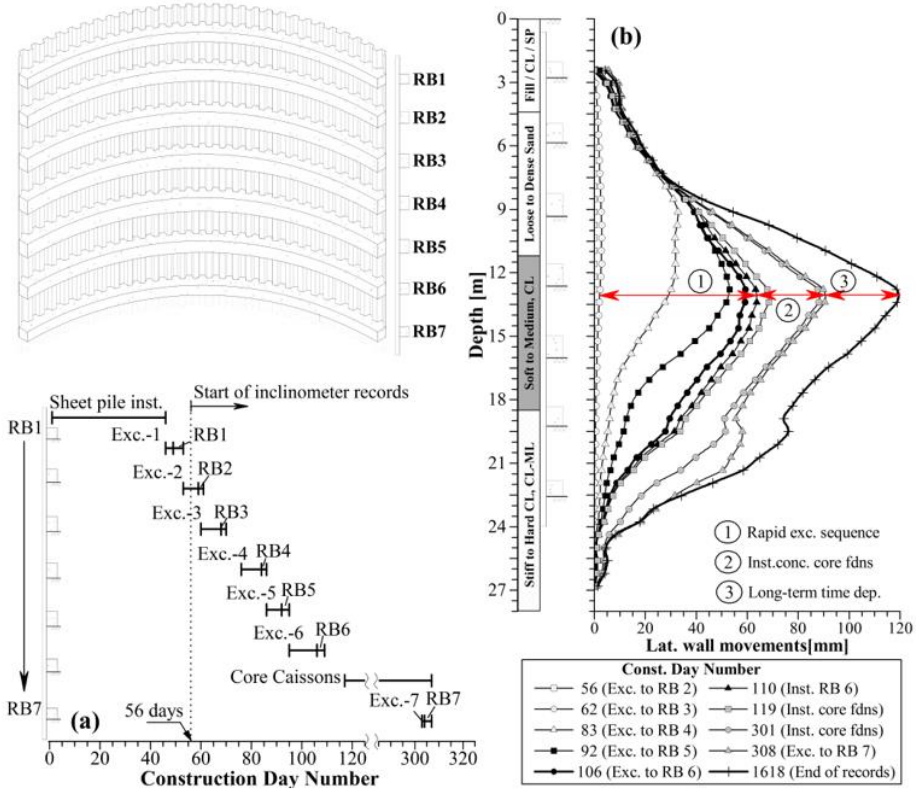

Figure 2-19. Observed performance of cofferdam at anonymous site a) cofferdam layout and construction sequence; and b) lateral wall movements (Uribe-Henao et al. 2017).

The cofferdam construction started with sheet piles driving, this activity took 46 days. Subsequently, accelerated cycles of soil removal and concrete ring beams installations were executed since +2.40 CCD until to reaching excavation 6 at level -16.26 CCD. At this point, the excavation activities were temporarily suspended to install deep foundations until day 301, where the excavation continued until the -19.58 CCD level.

Figure 2-21 b) shows the lateral displacement measured in the inclinometer I-1. On the maximum lateral deformation shown in this figure, 3 analysis sections were marked with circle numbers 1,2 and 3. The mark with circle number 1 corresponds to the lateral displacements recorded from excavation 2 to excavation 6, at this point a cumulative deformation of 59.3 mm was obtained. Later, circle number 2 section shows the lateral displacement register during the install deep foundations, at the end of this stage the lateral displacement registered was 88.1 mm. Finally, at day 1618 the inclinometer registered 118.8 mm as the maximum lateral displacement that the bracing support system suffered. More information about the observed field performance is presented by (Arboleda-Monsalve et al. 2017) and (Uribe-Henao et al. 2017).

Figure 2-20shows lateral displacements according to time construction in days. Displacement curves for ring beams 1 to 7 are detailed since sheet piles installation until concrete core foundation construction and an additional time in which inclinometer I-1 registered more information.

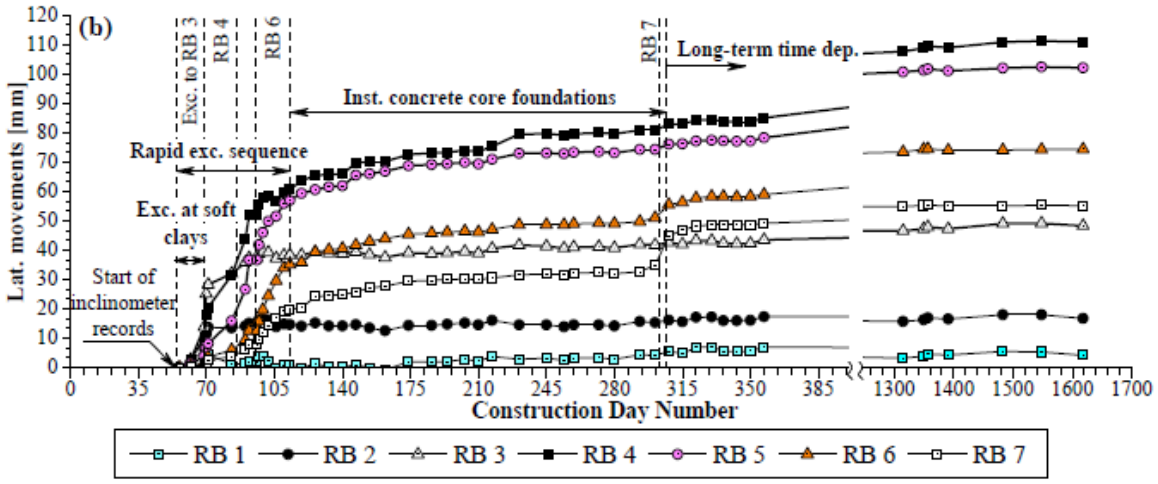

Figure 2-20. Observed lateral movements over construction timeline (Uribe-Henao et al. 2017).

2.3 Concrete Time-Dependent Effects

The concrete time-dependent effects studied in this research are creep, shrinkage and aging. The creep is defined as the increase of strain in hardened concrete, when it is subjected to a sustained load. It can be obtained from the difference between the total deformations and the initial elastic deformations. Shrinkage is the decrease in volume of concrete over time, which occurs after the hardening. The decrease in volume is the response of the concrete to changes in humidity and physico-chemical, which occur internally and are not associated with external actions, and aging effect is the development of stiffness and strength with time in the concrete.

These effects have been included in this research by following fédération internationale du béton code (2010). According to (Mola & Pellegrini, 2012) the fib Model Code 2010 improved formulations that define the concrete long-term behavior model under service life loading conditions. There is also included a method to take into account the effects of temperature on the time of loading, as well as modified values for the creep coefficient, in a non-linear form.

2.3.1 Development of Strength with Time

Table 2-5 shows the results of the tests of resistance to the compression that were realized to random samples of the concrete of the rings 1 to 5. In the same graph, the concrete resistance prediction curve is presented, which according to (fib Model Code, 2010) can be theoretically estimated at various ages fcm(t) using the equation (1) as a function of concrete age t and strength class of cement, for a curing process under a controlled temperature of 20°C. The results of the 28 days compressive strength tests yielded 55.5 MPa for ring beams 1 and 7, 53.5 MPa for ring beams 2 and 6 and finally 65.3 MPa for ring beams 3 to 5. **Table 2-4** shows coefficient s to be used in equation (2).

$$\mathrm{fcm(t)} = \beta\mathrm{cc(t)fcm} \quad (1)$$

$$\beta\mathrm{cc(t)} = \exp\left[s\left(1-\sqrt{\frac{28}{t}}\right)\right] \quad (2)$$

Where:

- fcm(t) is the mean compressive strength in MPa at an age t in days.
- fcm is the mean compressive strength in MPa at an age of 28 days.
- βcc(t) is a function to describe the strength development with time.

- t is the concrete age in days adjusted taking into account the temperature during curing.
- s is a coefficient which depends on the strength class of cement.

Table 2-4. Coefficient s (Adapted from table 5.1-9 (fib Model Code, 2010)).

***fcm* [MPa]**	**Strength class of cement**	***s***
≤60	32.5 N	0.38
≤60	32.5 R, 42.5 N	0.25
≤60	42.5 R, 52.5 N, 52.5 R	0.20
>60	all classes	0.20

Table 2-5. Compressive strength for concrete ring beam 1 to 5 obtained from laboratory test.

Ring Beam 1		Ring Beam 2		Ring Beam 3		Ring Beam 4		Ring Beam 5		Ring Beam 6		Ring Beam 7	
t	f'_c	t	f'_c	t	f'_c	t	f'_c	t	f'_c	t	f'_c	t	f'_c
days	MPa	days	MPa	days	MPa	days	MPa	days	MPa	days	MPa	days	MPa
0	0	0	0	0	0	0	0	0	0.0	data not available		data not available	
4	36.5	3	31.3	3	48.9	7	51.1	7	48.0				
5	35.5	4	38.7	7	48.0	14	60.4	56	66.8				
7	41.3	7	42.1	14	61.2	28	62.7						
14	46.4	14	48.4	28	65.3	56	68.1						
28	55.5	28	53.5	56	67.9								
56	59.8	56	54.8										
		91	59.5										

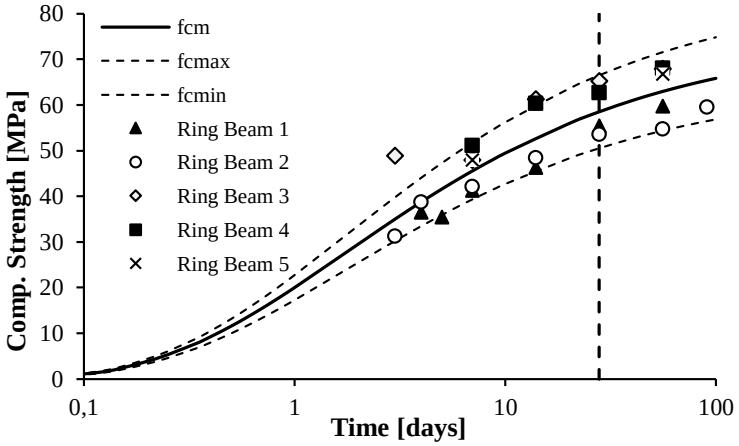

Figure 2-21. laboratory concrete compressive strength test from construction reports.

2.3.2 Development of Elastic Modulus with Time

The evaluation of the elastic modulus was performed through the implementation of the formulation presented by (fib Model Code, 2010), wherein the modulus of elasticity at age of 28 days is calculated by equation (3) and at an age t ≠ 28 days may be estimated from equation (4) and (5).

$$E_{ci} = 21500MPa\left(\frac{f'_{cm}}{10}\right)^{1/3} \quad (3)$$

$$E_{ci}(t) = \beta_E(t)E_{ci} \quad (4)$$

$$\beta_E(t) = [\beta cc(t)]^{0.5} \quad (5)$$

Where:

- $E_{ci}(t)$ is the modulus of elasticity in MPa at an age t in days;
- E_{ci} is the modulus of elasticity in MPa at an age of 28 days;
- $\beta_E(t)$ is a coefficient which depends on the age of concrete, t in days.

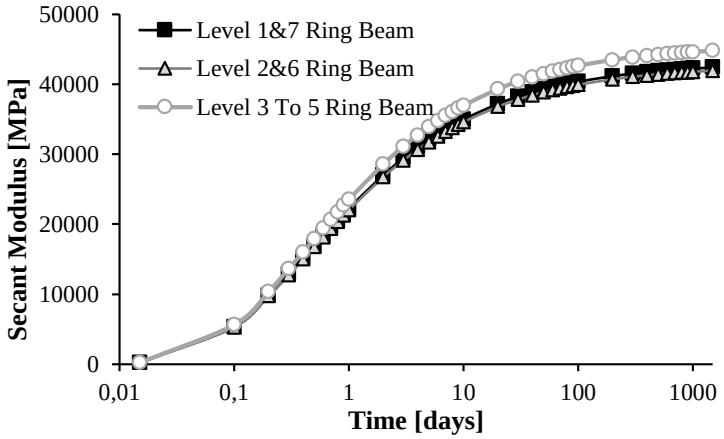

Figure 2-22. Modulus of elasticity with time

2.3.3 Creep

Within the range of service stresses $\sigma_C \leq 0.4f_{cm}(t_0)$ creep is assumed to be linearly related to stress. For a constant stress $\sigma_C(t_0)$ in MPa applied at time (t_0) this leads to the subsequent creep strain $\varepsilon_{cc}(t, t_0)$.

$$\varepsilon_{cc}(t,t_0) = \frac{\sigma_C(t_0)}{E_{ci}}\varphi(t,t_0) \quad (6)$$

Where:

- $\varphi(t,t_0)$ is the creep coefficient;
- E_{ci} is the modulus of elasticity at age of 28 days.

The stress dependent strain is given by:

$$\varepsilon_{c\sigma}(t,t_0) = \sigma_C(t_0)\left[\frac{1}{E_{ci}(t_0)} + \frac{\varphi(t,t_0)}{E_{ci}}\right] = \sigma_C(t_0)\,J(t,t_0) \quad (7)$$

Where:

- $J(t,t_0)$ is the creep function or creep compliance, representing the total stress-dependent strain per unit stress;
- $E_{ci}(t_0)$ is the modulus of elasticity at the time of loading t_0.

For practical applications concrete may be considered as an ageing linear viscoelastic material, and for variable stresses and strains, the principle of superposition is assumed to be valid. On the basis of these assumptions and definitions given above, the constitutive equation for concrete may be written as:

$$\varepsilon_c(t) = \sigma_C(t_0)\,J(t,t_0) + \int_{t_0}^{t} J(t,\tau)\frac{\partial\sigma_C(\tau)}{\partial\tau}d\tau + \varepsilon_{cn}(t) \quad (8)$$

The creep coefficient $\varphi(t,t_0)$ may be calculated from:

$$\varphi(t,t_0) = \varphi_{bc}(t,t_0) + \varphi_{dc}(t,t_0) \quad (9)$$

Where:

- $\varphi_{bc}(t,t_0)$ is the basic creep coefficient;
- $\varphi_{dc}(t,t_0)$ is the drying creep coefficient.(t is the age of concrete in days at the moment considered; t_0 is the age of concrete at loading in days).

The basic creep coefficient may be estimated from:

$$\varphi_{bc}(t,t_0) = \beta_{bc}(f_{cm}) * \beta_{bc}(t,t_0) \quad (10)$$

$$\beta_{bc}(f_{cm}) = \frac{1.8}{(f_{cm})^{0.7}} \quad (11)$$

$$\beta_{bc}(t, t_0) = \ln(\left(\frac{30}{t_{0,adj}} + 0.035\right)^2 (t - t_0) + 1) \quad (12)$$

Where:

- $t_{0,adj}$ is the adjusted age at loading days;
- f_{cm} is the mean compressive strength at 28 days in MPa.

The drying creep coefficient $\varphi_{dc}(t, t_0)$ may be estimated from:

$$\varphi_{dc}(t, t_0) = \beta_{dc}(f_{cm}) * \beta_{dc}(t, t_0) * \beta(RH) * \beta_{dC}(t_0) \quad (13)$$

$$\beta_{dc}(f_{cm}) = \frac{412}{(f_{cm})^{1.4}} \quad (14)$$

$$\beta(RH) = \frac{1-\frac{RH}{100}}{\sqrt[3]{0.1\frac{h}{100}}} \quad (15)$$

$$\beta_{dc}(t_0) = \frac{1}{0.1+t_{0,adj}{}^{0.2}} \quad (16)$$

The development of drying creep with time is described by:

$$\beta_{dc}(t, t_0) = \left[\frac{(t-t_0)}{\beta_h+(t-t_0)}\right]^{\gamma(t_0)} \quad (17)$$

$$\gamma(t_0) = \frac{1}{2.3+\frac{3.5}{\sqrt{t_{0,adj}}}} \quad (18)$$

$$\beta_h = 1.5h + 250 \propto_{fcm} \leq 1500 \propto_{fcm} \quad (19)$$

$$\propto_{fcm} = (\frac{35}{fcm})^{0.5} \quad (20)$$

Where:

- RH is the relative humidity of the ambient environment in %;
- $h = 2Ac/u$, is the notional size of the member in mm, where Ac is the cross-section in mm^2 and u is the perimeter of the member in contact with the atmosphere in mm.

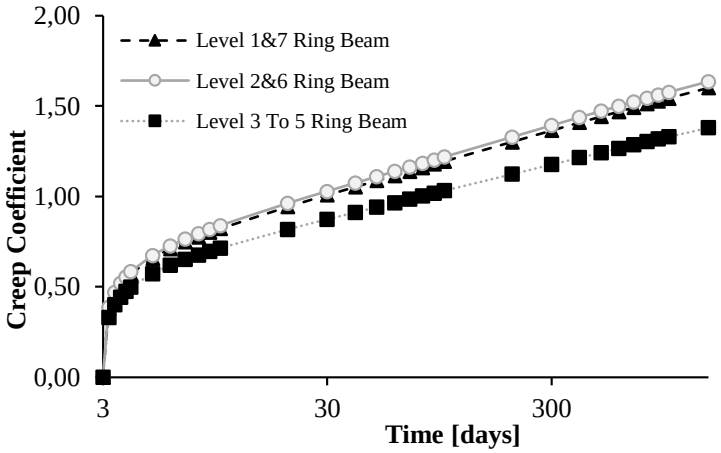

Figure 2-23. Creep Coefficient Vs time

2.3.4 Shrinkage

The total shrinkage or swelling strains $\varepsilon_{cs}(t, t_s)$ may be calculated as:

$$\varepsilon_{cs}(t, t_s) = \varepsilon_{cbs}(t) + \varepsilon_{cds}(t, t_s) \quad (21)$$

where shrinkage is subdivided into the basic shrinkage $\varepsilon_{cbs}(t)$ which occurs even if no moisture loss is possible:

$$\varepsilon_{cbs}(t) = \varepsilon_{cbs0}(fcm) * \beta_{bs}(t) \quad (22)$$

and the drying shrinkage $\varepsilon_{cds}(t, t_s)$ giving the additional shrinkage if moisture loss occurs:

$$\varepsilon_{cds}(t, t_s) = \varepsilon_{cds0}(fcm) * \beta_{RH}(RH) * \beta_{ds}(t - t_s) \quad (23)$$

Where:

- t is the concrete age in days;
- t_s is the concrete age at the beginning of drying in days;
- $t - t_s$ is the duration of drying in days.

The basic shrinkage component $\varepsilon_{cbs}(t)$ may be estimated by means of the basic notional shrinkage coefficient $\varepsilon_{cbs0}(fcm)$ and the time function $\beta_{ds}(t)$:

$$\varepsilon_{cbs0}(fcm) = -\propto_{bs} \left(\frac{0.1*fcm}{6+0.1*fcm}\right)^{2.5} * 10^{-6} \quad (24)$$

$$\beta_{bs}(t) = 1 - \exp(-0.2\sqrt{t}\,) \quad (25)$$

Where:

- fcm is the mean compressive strength at the age of 28 days in MPa;
- $\propto_{bs}$ is a coefficient, dependent on the type of cement.

Table 2-6. Coefficients α_i (Adapted from table 5.1-9 (fib Model Code, 2010)).

Strength class of cement	α_{bs}	α_{ds1}	α_{ds2}
32.5 N	800	3	0.013
32.5 R, 42.5 N	700	4	0.012
42.5 R, 52.5 N, 52.5 R	600	6	0.012

The drying shrinkage $\varepsilon_{cds}(t, t_s)$ is calculated by means of the notional drying shrinkage coefficient $\varepsilon_{cds0}(fcm)$ the coefficient $\beta_{RH}(RH)$, taking into account the effect of the ambient relative humidity, and the function b ds(t-ts) describing the time-development:

$$\varepsilon_{cds0}(fcm) = [(220 + 110 * \alpha_{ds1}) * \exp(-\alpha_{ds2} * fcm)] * 10^{-6} \quad (26)$$

$$\beta_{RH} = \begin{cases} -1.55 * \left[1 - \left(\frac{RH}{100}\right)^3\right] & for\ 40 \le RH \le 99\% * \beta_{s1} \\ 0.25 & for\ RH \ge 99\% * \beta_{s1} \end{cases} \quad (27)$$

$$\beta_{ds}(t - t_s) = \left(\frac{(t-t_s)}{0.035*h^2+(t-t_s)}\right)^{0.5} \quad (28)$$

$$\beta_{s1} = \left(\frac{35}{fcm}\right)^{0.1} \le 1.0 \quad (29)$$

Where:

- α_{ds2}, α_{ds2} are coefficients, dependent on the type of cement;

- fcm is the mean compressive strength at the age of 28 days in MPa;
- RH is the relative humidity of the ambient atmosphere in %;
- h =$2Ac/u$, is the notional size of the member in mm, where Ac is the cross-section in mm^2 and u is the perimeter of the member in contact with the atmosphere in mm;
- t is the concrete age in days;
- t_s is the concrete age at the beginning of drying in days;
- $(t - t_s)$ is the duration of drying in days.

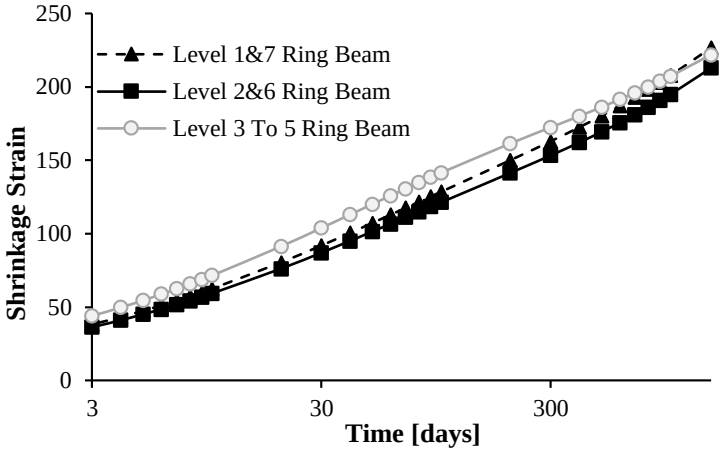

Figure 2-24. Shrinkage strain Vs time

2.3.5 Temperature Effects

During the construction of the ring beams of the cofferdam the local temperature was recorded daily, **Figure 2-25** presents the variation that exhibits values that normally were below 20 °C. It is important to mention that the lowest temperatures were recorded during the casting of the concrete that forms the beams, making slower the curing process and affecting the activation energy of the concrete hydration between cement and aggregates (fib Model Code, 2010). **Figure 2-26** shows effects of temperature on concrete age, indicating a delay in the development of compressive strength as a function of normal conditions of cure at 28 days and in typical environments of laboratories where the Temperature is regulated is presented.

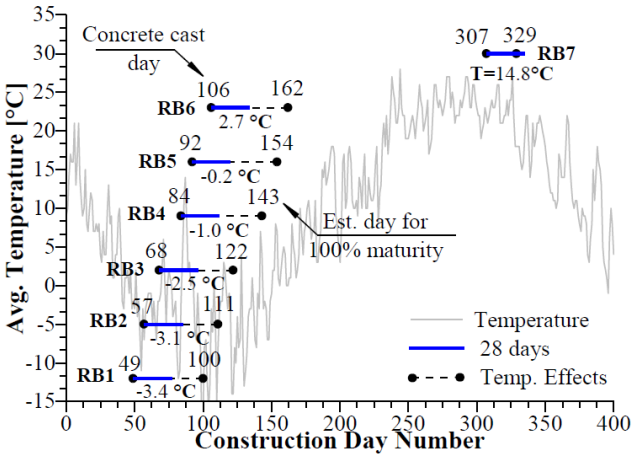

Figure 2-25. Daily average local temperature for cofferdam at site

The (fib Model Code, 2010) specifies that the effect of elevated or reduced temperatures on the maturity of concrete may be taken into account by adjusting the concrete age, through the replacement of equation (30) in equation (2).

$$t_T = \sum_{i=!}^{n} \Delta t_i exp\left[13.65 - \frac{4000}{273+T(\Delta t_i)}\right] \quad (30)$$

Where:

- t_T is the temperature-adjusted concrete age which replaces t in the corresponding equations in days;
- Δt_i is the number of days where a temperature T prevails;
- $T(\Delta t_i)$ is the mean temperature in °C during the time period Δt_i.

The concrete maturity, which indicates how the compressive strength of the concrete has increased with time as affected by temperature effects, was estimated replacing the concrete age of the equation (30). Additionally, the effect of temperature on the compressive strength of normal strength and high strength normal weight and lightweight aggregate concrete, $f_{cm}(T)$ and $fl_{cm}(T)$, respectively, may be calculated as:

$$f_{cm}(T) = f_{cm}(1.06 - 0.003T) \quad (31)$$

Where:

- $f_{cm}(T)$ is the compressive strength in MPa at the temperature T in °C.
- f_{cm} is the compressive strength in MPa at T = 20 °C.
- T is the temperature in ºC.

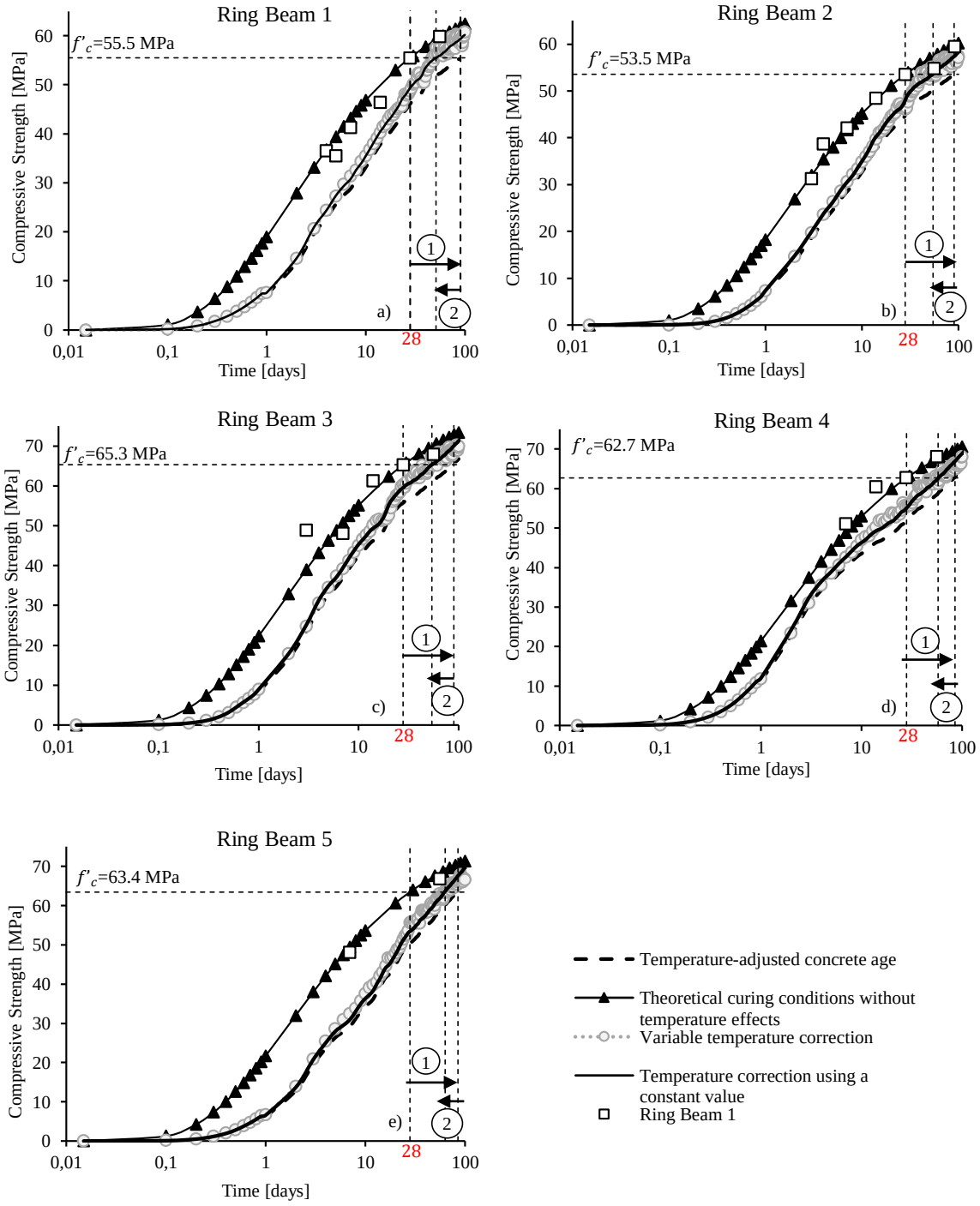

1. Delay in f'_c due to temperature effect in concrete age.
2. Delay in f'_c due to temperature effect directly in compressive strength. For obtain more information about this result, see (Arboleda-Monsalve et al. 2017).

Figure 2-26. Temperature effect on concrete compressive strength, a) ring beam 1, b) ring beam 2, c) ring beam 3, d) ring beam 4, e) ring beam 5.

Following equations presented by (fib Model Code, 2010) describe effect of a constant temperature differing from 20°C while a normal weight concrete is under load. The effect of temperature on the time-development of creep is taken into account using $\beta_{h,T}$:

$$\beta_{h,T} = \beta_h * \beta_T \quad (32)$$

$$\beta_T = exp\left[\frac{1500}{273+T} - 5.12\right] \quad (33)$$

Where:

- $\beta_{h,T}$ is a temperature dependent coefficient;
- T is the temperature in °C.

The effect of temperature on the creep coefficient is taken into account using:

$$\varphi_{bc,T} = \varphi_{bc} * \varphi_T \quad (34)$$

$$\varphi_{dc,T} = \varphi_{dc} * {\varphi_T}^{1.2} \quad (35)$$

$$\varphi_T = exp[0.015(T - 5.12)] \quad (36)$$

Where:

- $\varphi_{bc,T}$ is a temperature dependent coefficient;
- $\varphi_{dc,T}$ is a temperature dependent coefficient;
- φ_{bc} is the basic creep coefficient;
- φ_{dc} is the drying creep coefficient.

If temperature increases while the structural member is under load, creep may be estimated from:

$$\varphi(t, t_0, T) = \varphi(t, t_0) + \Delta\varphi_{T,trans} \quad (37)$$

$$\Delta\varphi_{T,trans} = 0.0004(T - 20)^2 \quad (38)$$

Where:

- $\varphi(t, t_0)$ is the creep coefficient temperature-adjusted;
- $\Delta\varphi_{T,trans}$ is the transient thermal creep coefficient which occurs at the time of the temperature increase.

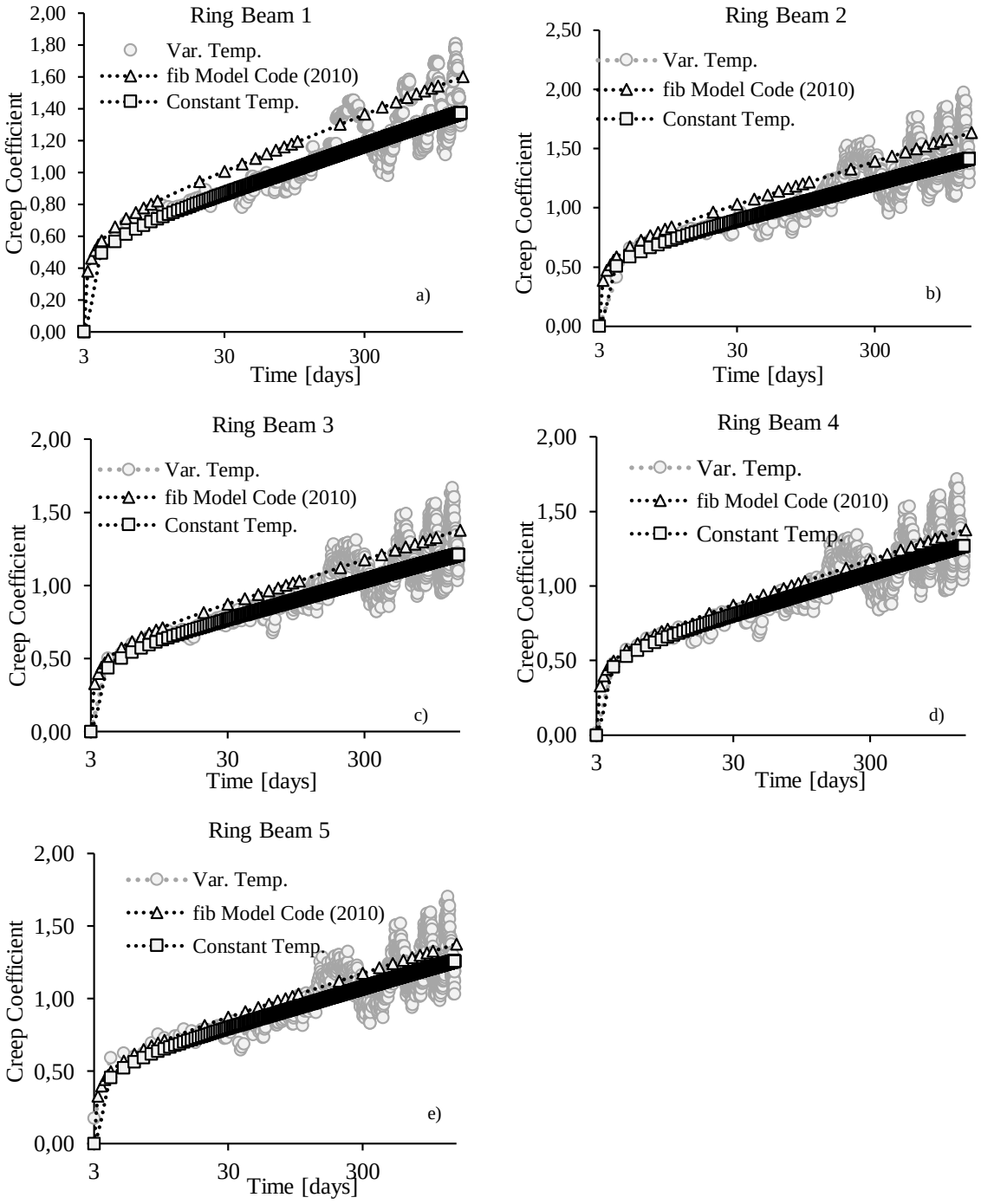

Figure 2-27. temperature effect in creep vs time a) ring beam 1, b) ring beam 2, c) ring beam 3, d) ring beam 4, e) ring beam 5.

According to (fib Model Code, 2010) For basic shrinkage mainly the time-development is influenced. To take this effect into consideration, the concrete age t has to be replaced by the effective concrete age t_T. The effect of a constant temperature differing from 20 °C while the concrete is drying is described by the following equations. The effect of temperature on the time-development of drying shrinkage is taken into account using α_{sT}:

$$\alpha_{sT}(T) = 0.035 * h^2 exp[-0.06(T-20)] \quad (39)$$

Where:

$\alpha_{sT}(T)$ is a temperature-dependent coefficient replacing the product 0.035 h^2.

The effect of temperature on the magnitude of drying shrinkage is taken into account by using:

$$\beta_{RH,T} = \beta_{RH} * \beta_{sT} \quad (40)$$

$$\beta_{sT} = 1 + (\frac{4}{103-RH}) * (\frac{T-20}{40}) \quad (41)$$

$$\beta_{RH} = \begin{cases} -1.55 * \left[1 - (\frac{RH}{100})^3\right] for\ 40 \leq RH < RH_T \\ 0.25\ for\ RH \geq RH_T \end{cases} \quad (42)$$

$$RH_T = 99\beta_{s1} + \beta_{s1,T} \leq 100\% \quad (43)$$

$$\beta_{s1} = (\frac{35}{f_{cm}})^{0.1} \leq 1.0 \quad (44)$$

$$\beta_{s1,T} = (\frac{T-20}{25})^3 \quad (45)$$

Where:

- $\beta_{RH,T}$ is a temperature-dependent coefficient.
- RH is the relative humidity of the ambient environment in %;
- f_{cm} is the mean compressive strength at the age of 28 days.
- T is the temperature in ºC.

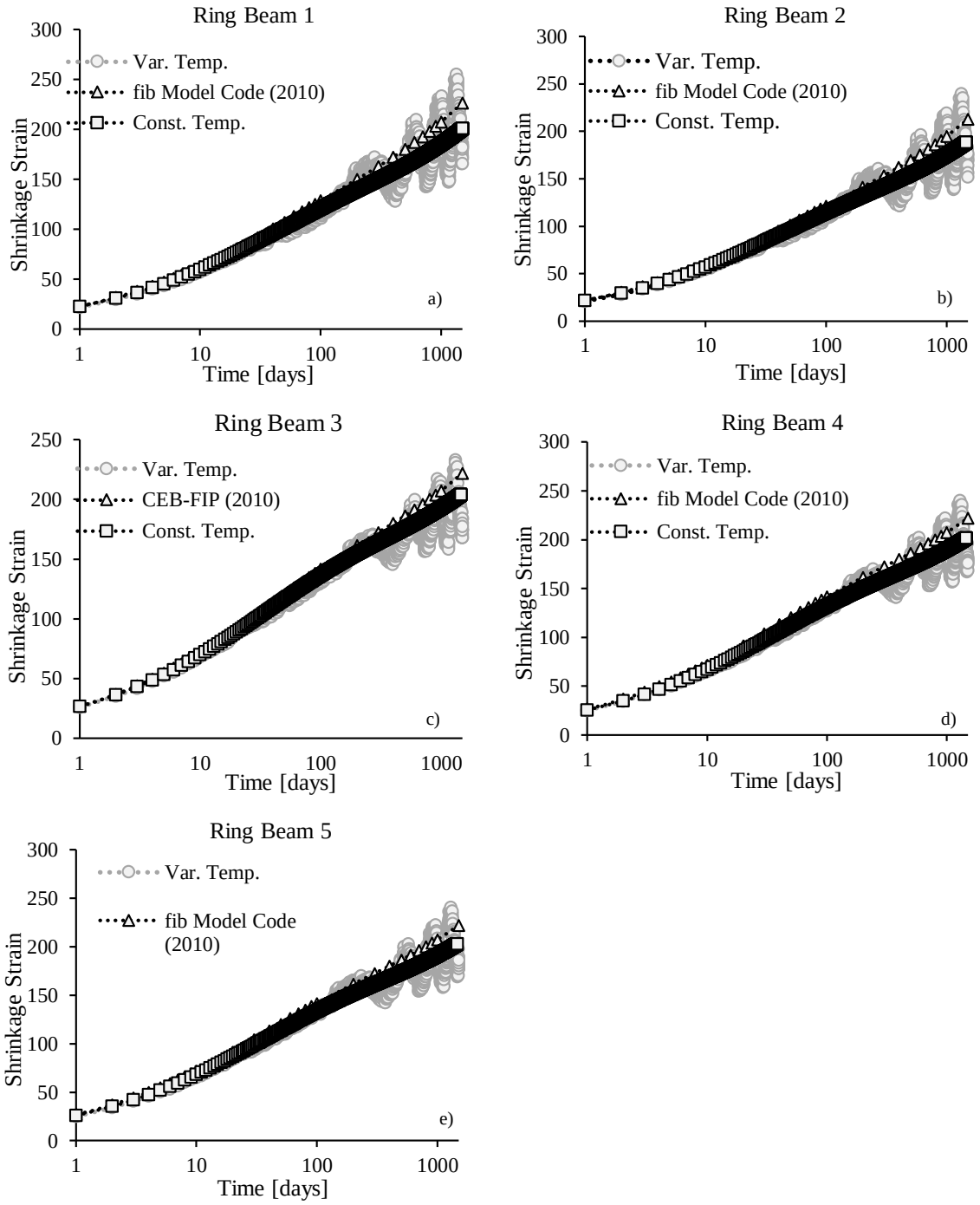

Figure 2-28. Shrinkage with effect of temperature Vs time a) ring beam 1, b) ring beam 2, c) ring beam 3, d) ring beam 4, e) ring beam 5.

2.4 Constitutive Models and Material Behavior

2.4.1 Shotcrete Model

Different Shotcrete Models are analyzed to better understand the behavior of this material. A Short description of several models is presented below. The shotcrete constitutive model proposed by (Shädlich & Schweiger, 2014) is a simple formulation that uses the conventional elastoplastic framework to decompose the total strains into four basic components, elastic ε^e, plastic ε^p, creep ε^{cr}, and shrinkage strains ε^{sh}. The model adopts a plastic strain-hardening/softening approach proposed by (Shütz, Potts, & Zdravkovic, 2011) to include the time dependency nature of cement-base materials. This approach consideres time-dependent compressive and tensile plastic peak strains to recreate the increase of stiffness and strength observed in uniaxial stress-strain curves.

A fictitious crack model, defined by (Hillerborg, Modéer, & Petersson, 1976) as an energy balance approach, is also included to account for the quasibrittle behavior during fracturing. This approach eliminates the dependency of very small elements close to the fracture process zone in Finite Element Methods (FEM) accounting for crack formation and propagation. In addition, the Mohr-coulomb and Rankine yield surface are adopted to vary with time in function of compressive and tensile yield strengths. The model is capable of predicting time-dependent behavior including the plastic deformability at early ages, failure, and fracture process zone during strain-softening in compression and tension.

Constitutive models for cement-base materials haves been object of study for the last decades. Early formulations based on continuum mechanics were developed using elasticity and plasticity theories for strain-hardening/softening rules but excluding time dependency effects and cracking (Chen & Chen, 1975); (Han & Chen, 1985); (Lade & Kim, 1995); (William, 1975). (Chen & Suzuki, 1980) and (Frantziskonis & Desai, 1987) improved those formulations using fracture energy methods to include the cracking development of concrete.

Later, (Pietruszczak, Jiang, & Mirza, 1988) in an elastoplastic framework introduced a simple methodology to capture the progressive transition from ductile to brittle behavior of concrete (i.e., quasibrittle material). The author applied a non-associative flow rule to describe the deformation process under compressive and tensile load during hardening and softening of concrete.

Other authors in recent studies (Meschke 1996) (Meschke et al. 1996) formulated a more sophisticated constitutive model to include the increase of strength with time, considering creep and shrinkage as two basic components of the total strains under a viscoplastic formulation.

The model referred in this research is based on an elastoplastic framework similar to those developed in 1970s including strain-hardening/softening and time-dependent effects based on those proposed by (Shütz, Potts, & Zdravkovic, 2011). The shotcrete model has served as solution for modeling of tunneling lining, capturing the plastic behavior of shotcrete at early hours and the quasibrittle behavior after curing. This model developed by (Shädlich & Schweiger, 2014) has been implemented in the numerical software Plaxis and is used in this paper to simulate the concrete time dependent and stress-strain-strength behavior.

Table 2-7 lists the parameters of the Shotcrete model for concrete (Schädlich and Schweiger 2014b; a) with a short description and summary of how each parameter was obtained. Those parameters stand for the stress-strain-strength behavior, fracture energy and the time-dependent nature of concrete, including the effects of low temperatures during casting and curing. Further details can be found in(Uribe-Henao 2017).

Table 2-7. Shotcrete Model Parameters for Concrete.

#	Symbol	Parameter name	Unit	Source
1	t_{hydr}	Time for 100% of maturity	Days	Development of concrete compressive strength.
2	E_{28}	Young's Modulus at an age of t_{hydr}	kN/m²	(Fédération Internationale du Béton 2010)
3	E_1/E_{28}	Stiffness ratio at 1 day and t_{hydr}	-	Development of concrete stiffness,(Arboleda-Monsalve et al. 2017)
4	$f_{c,28}$	Compressive strength at an age of t_{hydr}	kN/m²	Cylinder test from concrete reports, (Arboleda-Monsalve et al. 2017)
5	$f_{c,1}/f_{c,28}$	Strength ratio at 1 day and t_{hydr}	-	Development of concrete compressive strength, Arboleda-Monsalve et al. (2017)
6	$f_{t,28}$	Tensile strength at an age of t_{hydr}	-	Values reported by (Collins and Mitchel 1991)
7	f_{c0n}	Initial ratio $f_{cy}/f_{cp}(t)$	-	Values reported by (Collins and Mitchel 1991)
8	f_{cfn}	Failure strength ratio $f_{cf}/f_{cp}(t)$	-	Values reported by (Collins and Mitchel 1991)
9	f_{cun}	Residual strength level $f_{cu}/f_{cp}(t)$	-	Values reported by (Collins and Mitchel 1991)
10	f_{tun}	Residual strength level $f_{tu}/f_{tp}(t)$	-	Values reported by (Collins and Mitchel 1991)
11	ϕ_{max}	Maximum friction angle	degress	Measured by (Schädlich and Schweiger 2014b)
12	ε^{p}_{1h}	Uniaxial plastic failure strain at 1 hour	-	Peak plastic strain (Schütz et al. 2011)
13	ε^{p}_{8h}	Uniaxial plastic failure strain at 8 hour	-	Peak plastic strain (Schütz et al. 2011)
14	ε^{p}_{24h}	Uniaxial plastic failure strain at 24 hour	-	Peak plastic strain (Schütz et al. 2011)
15	$G_{c,28}$	Compressive fracture energy at t_{hydr}	kN/m	Classic equation for concrete in compression (Collins and Mitchel 1991)
17	ϕ^{cr}	Ratio between creep and elastic strains	-	Presented by (Arboleda-Monsalve et al. 2017)
18	t^{cr}_{50}	Time for 50% of creep strains	days	Presented by (Arboleda-Monsalve et al. 2017)
19	$\varepsilon^{sh}_{\infty}$	Final shrinkage strain	-	Presented by (Arboleda-Monsalve et al. 2017)
20	t^{sh}_{50}	Time for 50% of shrinkage strains	days	Presented by (Arboleda-Monsalve et al. 2017)

The normalized uniaxial stress-strain curve implemented in the Shotcrete model conforms the basis of the nonlinear evolution of the yield surface and natural increase of stiffness and strength with time. This curve was introduced by (Shütz, Potts, & Zdravkovic, 2011) in function of the hardening/softening parameter H_c and the normalized equivalent uniaxial compressive strength $f_{c,n}$. Both dimensionless and expressed in terms of the peak plastic strain $\varepsilon^{p}_{cp}(t)$ and time-dependent compressive peak stress $f_{cp}(t)$, respectively, as presented in equation (46) and equation (47).

$$H_c = \frac{\varepsilon_3^p}{\varepsilon_{cp}^p(t)} \quad (46)$$

$$f_{c,n} = \frac{\sigma_3}{f_{cp}(t)} = \frac{f_{cy}}{f_{cp}(t)} \quad (47)$$

Where ε_3^p is the minor principal plastic strain and σ_3 is the minor principal stress, equivalent to the compressive yield strength f_{cy}. The model uses a tension-positive-convention where the minor principal direction is taken as compression. **Figure 2-29** shows Shotcrete normalized stress-strain curve (Schütz et al. 2011), this curve concrete compressive strength, which is conformed by four parts: Part I: quadratic strain Hardening (Full mobilization of f_c), Part II: linear strain softening (until the failure strength), Part III: linear strain softening (Strength reduction, destruction of inter-particle bonds), Part IV: constant residual strength.

In addition, **Figure 2-30** shows the normalized stress-strain curve at an age of t_{hydr} obtained using the classic equation for concrete in uniaxial compression presented by (Collins and Mitchel 1991) and the one computed with the Shotcrete model for the ring beams 1 thru 5. It is seen that the zones of hardening and softening coincide with the stress-strain curve described by (Collins and Mitchel 1991). The resistance of concrete due to tension is ignored in this research. The confining loading and the circular geometry of the cofferdam induces to the lateral bracing system compressive stresses. However, neglectable tensile strength parameters are chosen to avoid divergence during the simulations.

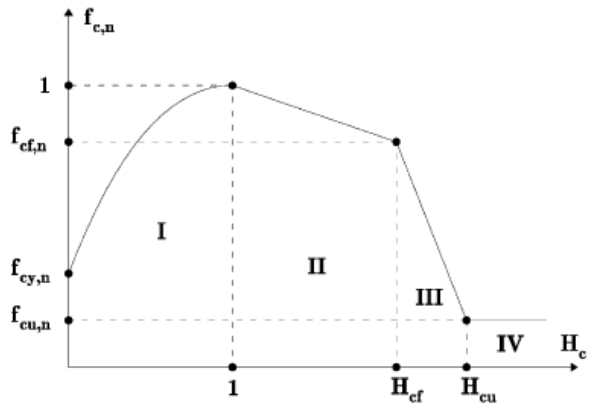

Figure 2-29. Shotcrete normalized stress-strain curve (Schütz et al. 2011)

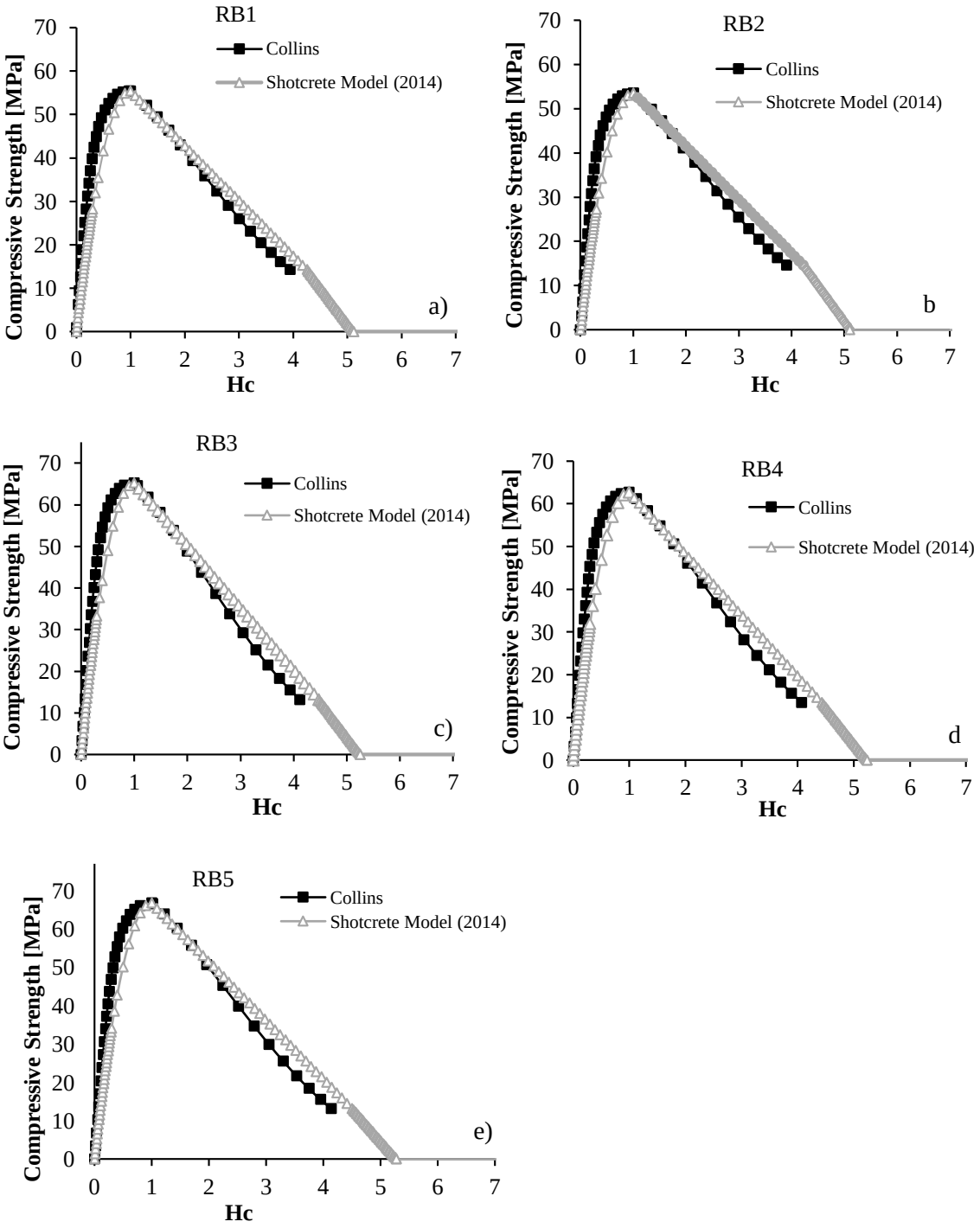

Figure 2-30. Normalized stress-strain curve for concrete. a) Ring beam 1, b) ring beam 2, c) ring beam 3, d) ring beam 4, e) ring beam 5.

("Ceb-Fip Model Code" 1990) was adopted in shotcrete model to calculate concrete strength and the stiffness variation with respect to time; equations (48) and (49) are used for this objective:

$$\frac{f_{cp}(t)}{f_{c,28}} = \exp\left[-\frac{\ln\left(f_{c,1}/f_{c,28}\right)}{\sqrt{t_{hydr}}-1}\left(1-\sqrt{\frac{t_{hydr}}{t}}\right)\right] \tag{48}$$

$$\frac{E(t)}{E_{28}} = \exp\left[-\frac{\ln\left(E_{c,1}/E_{c,28}\right)}{\sqrt{t_{hydr}}-1}\left(1-\sqrt{\frac{t_{hydr}}{t}}\right)\right] \tag{49}$$

Complementarily, the time-dependent compressive peak plastic strain was assumed to vary according to the equation (50) (Schütz et al. 2011), where the parameters ε_{1h}^{p}, ε_{8h}^{p} and ε_{24h}^{p} were determined in order to match the plastic strain at an age of t_{hydr} reported by (Collins and Mitchel 1991).

$$\varepsilon_{cp}^{p}(t) = A\cdot\left[\ln\left(\frac{t}{0.416}\right)\right]^{B} + C \tag{50}$$

$$A = \frac{\varepsilon_{24h}^{P} - \varepsilon_{1h}^{p}}{3.178^{B}} \tag{51}$$

$$B = -\frac{\ln\left(\dfrac{\varepsilon_{8h}^{p} - \varepsilon_{1h}^{p}}{\varepsilon_{24h}^{p} - \varepsilon_{1h}^{p}}\right)}{0.424} \tag{52}$$

$$C = \varepsilon_{1h}^{p} \tag{53}$$

(Schädlich and Schweiger 2014b) expressed the creep strain in an incremental form as it is presented in equation (54). This equation is given in function of the creep coefficient ϕ^{cr} and the time required to reach a 50% of creep strain t_{50}^{cr} as follows:

$$\varepsilon_{n+1}^{cr} = \varepsilon_{n}^{cr} + \frac{\varepsilon_{\infty}^{cr} - \varepsilon_{n}^{cr}}{t_n + t_{50}^{cr}}\cdot\Delta t \text{ and } \varepsilon_{\infty}^{cr} = \phi^{cr}\,\frac{\sigma}{E(t)} \tag{54}$$

Where, $\varepsilon_{\infty}^{cr}$ defined in terms of concrete stiffness and creep coefficient is the final creep strain for a given compressive stress, ε_{n+1}^{cr} and ε_{n}^{cr} are the creep strain at the end and beginning of step *n*; respectively. The (Eurocode 1992) is employed by the Shotcrete model to evaluate creep effect.

Shrinkage strains defined as a decrease in volume of concrete due to moisture loss caused by the exposure to the environment were obtained using the (ACI commite 209R-92 1992). (Schädlich and Schweiger 2014b) reported those strains including the time when the 50% of shrinkage t_{50}^{shr} occurred as presented in equation (55). This equation is given in terms of the final shrinkage $\varepsilon_{\infty}^{Shr}$ as follows:

$$\varepsilon^{Shr}(t) = \varepsilon_{\infty}^{shr} \cdot \frac{t}{t + t_{50}^{shr}} \tag{55}$$

2.4.2 Hardening Soil Model

Employing complex stress-strain models for geotechnical problems is not an accurate process when one does not have enough stiffness parameters, even if there is an acceptable amount of strength parameters data. In this section a constitutive model that uses a double-stiffness framework for elasticity combined with isotropic strain hardening is presented. This model defers with the ones which work with Hooke's single-stiffness with linear elasticity. (Schanz et al. 1999) developed The Hardening-Soil Model to simulate stiff and soft soils elasto-plastic response. This model is based on a multi-yield surface model considering the classical theory of plasticity. The hyperbolic model is surpassed by Hardening-Soil model considering 3 main aspects: Including soil dilatancy; introducing a yield cap; and using the theory of plasticity rather than the theory of elasticity.

Yield surface of Hardening Soil Model does not work with a principal stress space, but can consider plastic straining, in contrast with models working in the field of elasticity and perfect plasticity. Shear hardening, and compression hardening are the two main types of behaviors considered in this model. The first one is representative for deviatoric loads that induce irreversible strains, and the second one is a kind of hardening produced when primary compression in oedometer loading and isotropic loading induces irreversible plastic strains. The develop of Hardening-Soil model requires the input of 13 parameters, including classical Mohr- Coulomb ones, see **Table 2-8**.

Table 2-8. Hardening Soil Model Parameters.

#	Symbol	Parameter name	Unit
1	c'	Cohesion intercept	kN/m²
2	φ'	Angle of internal friction	Degrees
3	ψ	Angle of dilatancy	Degrees
4	${E_{50}}^{ref}$	Secant stiffness at 50% stress level in standard drained triaxial test	kN/m²
5	${E_{oed}}^{ref}$	Tangent stiffness for primary oedometer loading	kN/m²
6	m	Power for stress-level dependency of stiffness	-
7	${E_{ur}}^{ref}$	Unloading/ reloading stiffness (default $E_{ur}^{ref}=3E_{50}^{ref}$),	kN/m²
8	v_{ur}	Poisson's ratio for unloading-reloading (default $v_{ur}=0.2$)	-
9	p^{ref}	Reference stress for stiffness's (default $p^{ref}=100$ stress units)	mm
10	${K_0}^{NC}$	K_0 -value for normal consolidation (default $K_0^{NC}=1-\sin(\varphi)$)	-
11	R_f	Failure ratio q_f/q_a (default $R_f=0.9$),	-
12	$\sigma_{tension}$	Tensile strength (default $\sigma_{tension}=0$ stress units)	mm
13	$c_{increment}$	Increase of cohesion per unit of depth (default $c_{increment}=0$)	mm

There are some main parameters needed for the definition of the primary deviatoric loading behavior, and others needed for determining the behavior of stiffness when soil is subjected to a one-dimensional compression, so, soil stiffness parameters can be separated on this two groups.

Figure 2-31 shows a hyperbolic stress-strain curve that represent soil response when is subjected to a primary load. This curve represents the base of the Hardening Soil Model. For monotonic loading, this model considers the secant modulus (E_{50} determined from a triaxial stress-strain curve at 50% of the ultimate shear strength) as the reference parameter. Effective confining stress ($-{\sigma'}_3$) is directly related to the secant modulus, considering isotropical consolidated conditions. It can be said that E_{50} is dependent on -σ_3. Secant modulus can be defined considering a reference principal stress ($-\sigma_3 = p^{ref}$), as:

$$E_{50} = {E_{50}}^{ref} - \left(\frac{c\ cot\varphi - {\sigma'}_3\ sin\varphi}{c\ cos\varphi + p^{ref}\ sin\theta}\right)^m \quad (56)$$

Where ${E_{50}}^{ref}$ is the secant modulus at the reference stress, c and φ are the Mohr-Coulomb strength parameters (cohesion intercept and friction angle), and m refers to the amount of stress dependency. In a logarithmic stress dependency (commonly observed in soft clays), m is taken as 1.0. For other soils, m can take values between 0.5 to 1.0.

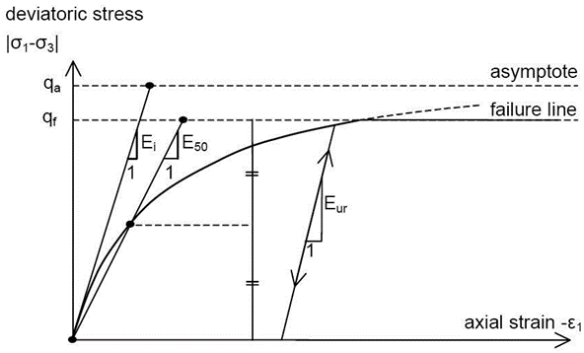

Figure 2-31. Hyperbolic Stress-Strain Relation in Primary Loading for a Standard Drained Triaxial Test (Schanz et al. 1999).

For primary compression, Hardening Soil Model takes an oedometer modulus as the reference for defining the soil stiffness. At a reference stress value (p^{ref}) oedometer stiffness modulus can be defined as:

$$E_{oed} = {E_{oed}}^{ref} - (\frac{c\,cot\varphi - {\sigma'}_1\,sin\varphi}{c\,cos\varphi + p^{ref}\,sin\theta})^m \quad (57)$$

Where E_{oed} is the tangent stiffness modulus for primary loading in constrained compression (zero lateral strain) and ${E_{oed}}^{ref}$ is a tangent stiffness at a reference vertical stress ($-\sigma_3 = p^{ref}$), as indicated in **Figure 2-32**.

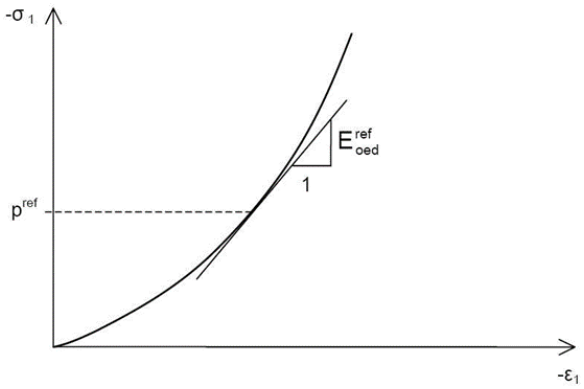

Figure 2-32. Definition of ${E_{oed}}^{ref}$ in Oedometer Test Results (Brinkgreve et al. 2011).

It is important to clarify that when primary loading is considered, ${\sigma'}_1$ is used rather than ${\sigma'}_3$. Hardening Soil Model does not present any relationship between oedometer and drained triaxial

stiffness (E_{oed} and E_{50} respectively), in contrast to elasticity models, which involve a fixed relationship between these two stifnesses.

Elastic Young's modulus E_{ur} depends on the effective confining stress (reference modulus ${E_{ur}}^{ref}$), that obeys to a reference pressure p^{ref}. Young's modulus is used to define and analyze stiffness subjected to unloading and reloading process, see **Figure 2-31**, and is defined as:

$$E_{ur} = {E_{ur}}^{ref} - \left(\frac{c\ cot\varphi - {\sigma'}_3\ sin\varphi}{c\ cos\varphi + p^{ref}\ sin\theta}\right)^m \quad (58)$$

Plaxis takes a default value for ${E_{ur}}^{ref}$ equal to $3{E_{50}}^{ref}$, but it can be set as other value in the formulation. Poisson's ratio (v_{ur}), depends on the strain level, but commonly, it varies between 0.1 and 0.2, but for Hardening Soil Model it is taken as 0.2 as default. Elastic theory indicates that for normally consolidated soils, Lateral earth pressure coefficient (${K_0}^{NC}$) is not dependent of v_{ur}, instead, this coefficient is related to the internal frictional angle (φ):

$${K_0}^{NC} = 1 - \sin(\varphi) \quad (59)$$

This is the most used correlation, that is why it is suggested to maintain this value. ${K_0}^{NC}$ values can be in a range related to some other parameters (v_{ur}, ${E_{50}}^{ref}$, ${E_{oed}}^{ref}$, ${E_{ur}}^{ref}$), but the input values outside this range will be rejected by Plaxis. Under primary triaxial loading, the basis of the Hardening Soil Model is shown by the relationship between vertical strain and deviatoric stress (ε_1 and $q = \sigma_1 - \sigma_3$, respectively). As it has been demonstrated in standard drained triaxial test yield curves, see **Figure 2-31**, soil shows a stiffness reduction with axial strain, when it is subjected to primary deviatoric loads, developing irreversible plastic strains. These yield curves can be described as:

For $q < q_f$:

$$-\varepsilon_1 = \frac{q}{E_i\left(1 - \frac{q}{q_a}\right)} \quad (60)$$

Where E_i is the initial stiffness, q_a is the asymptotic value of shear strength, and q_f is the ultimate deviatoric stress.

$$E_i = \frac{2E_{50}}{2-q_f} \quad (61)$$

$$q_a = \frac{q_f}{R_f} \quad (62)$$

$$q_f = (c\ cot\varphi - \sigma'_3\ sin\varphi)\frac{2sin\varphi}{1-sin\varphi} \quad (63)$$

q_a is found as the inverse of the slope of a plot of $\varepsilon_1/(\sigma_1 - \sigma_3)$ versus ε_1, and should be smaller than 1.0. Plaxis takes $q_a = 0.9$ as a default value. R_f is the failure ratio, given by the ratio between q_f and q_a. In Mohr-Coulomb model, the failure criterion is satisfied when $q = q_f$, and it traduces into a perfectly plastic yielding. Mohr-Coulomb failure criterion is the basis of the q_f relationship.

When considering stress paths of standard drained triaxial tests, hyperbolic stress-strain curve of Equation (60) is defined by Hardening Soil Model. Shear hardening yield function is defined as:

$$f = \bar{f} - \gamma^p \quad (64)$$

Where $\bar{f}$ is a stress function and γ^p is function of plastic shear strains.

$$\bar{f} = \frac{2q}{E_i(1-\frac{q}{q_a})} - \frac{2q}{E_{ur}} \quad (65)$$

$$\gamma^p = -(2{\varepsilon_1}^p - {\varepsilon_v}^p) \approx -2{\varepsilon_1}^p \quad (66)$$

Plastic volume change is very small compared to the axial strains, for hard soils, this is why this approximation is made and accepted. For a given value of plastic shear strain (parameter used for frictional hardening), yield condition $f = 0$ can be visualized in the $p' - q$ plane by using yield loci. Equations (64, 65 and 66) must be used to plot yield loci, that depends on exponent m to describe its shape. Slightly curved lines are obtained when m values are less than 1.0, but when it is equal to 1.0, curves form straight lines. The shape of yield loci for $m = 0.5$ (typical for hard soils) is shown in **Figure 2-33**.

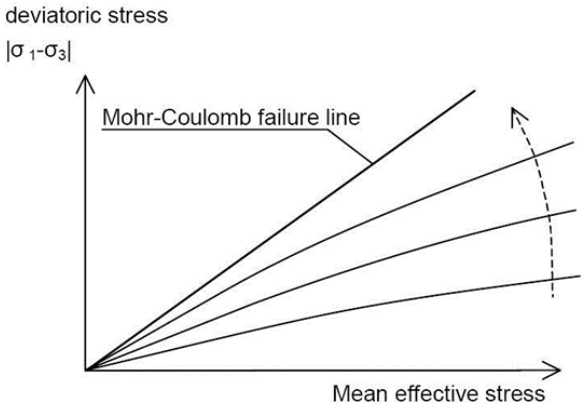

Figure 2-33. Yield Loci for Various Constant Values of Plastic Shear Strain (Schanz et al. 1999).

Plastic volume strain observed in isotropic compression is not explained by Shear yield surfaces, so another yield surface must be defined to analyze the elastic region. Independent input of ${E_{oed}}^{ref}$ and ${E_{50}}^{ref}$ must be allowed in that kind of yield surface. Magnitude of plastic strains associated with the shear yield surface, are controlled by ${E_{50}}^{ref}$, and plastic strains from yield cap are controlled by ${E_{oed}}^{ref}$. Hardening Soil Model describes an elliptical cap yield surface as:

$$f^c = \frac{\tilde{q}^w}{\propto^2} + p^2 - {p_p}^2 \tag{67}$$

Where f^c is the cap yield surface and $\propto$ is a parameter related to ${K_0}^{NC}$.

$$p = (\sigma_1 + \sigma_2 + \sigma_3)/3 \tag{68}$$

$$\tilde{q} = \sigma_1 + (\delta - 1)\sigma_2 - \delta\sigma_3 \tag{69}$$

$$\delta = \frac{3+sin\varphi}{3-sin\varphi} \tag{70}$$

In triaxial compression, where $-\sigma_1 > -\sigma_2$, $\tilde{q}$ becomes $-\sigma_1 - \sigma_3$. In triaxial extension, where $-\sigma_1 = -\sigma_2 > -\sigma_3$, $\tilde{q}$ reduces to $-\delta(\sigma_1 - \sigma_3)$.

The magnitude of the yield cap is determined by the isotropic preconsolidation stress (p_p), which can be derived from relations with plastic volumetric strain, under isotropic compression conditions, as follows:

$$\varepsilon_v{}^{pc} = \frac{\beta}{1-m}\left(\frac{p_p}{p^{ref}}\right)^{1-m} \quad (71)$$

Where $\varepsilon_v{}^{pc}$ is the volumetric cap strain, m refers to stress-level dependency, and β is a hardening modulus related to $E_{oed}{}^{ref}$. β and m are cap parameters derived from $K_0{}^{NC}$ and $E_{oed}{}^{ref}$.

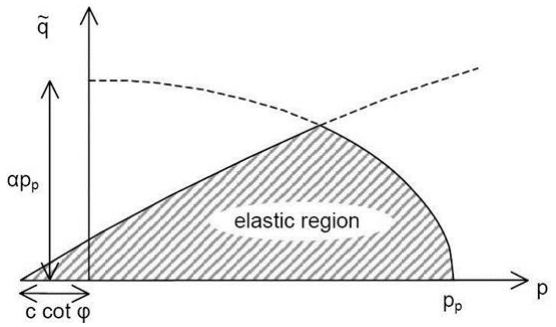

Figure 2-34. Yield Cap Surface of HSM $p - \tilde{q}$ -Plane (Brinkgreve et al. 2011)

As shown in **Figure 2-34**, yield cap shape has an ellipse shape in $p - \tilde{q}$ space. Aspect ratio is determined by α, and ellipse's magnitude is defined by preconsolidation stress p_p.

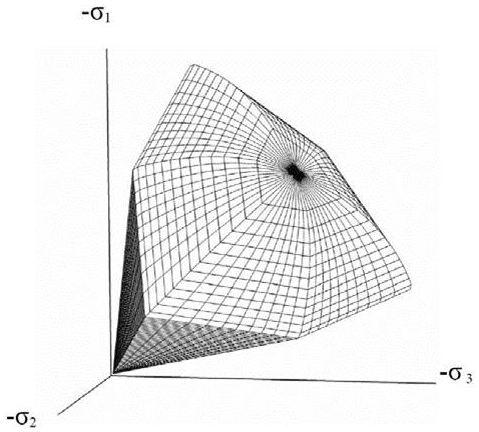

Figure 2-35. Representation of Total Yield Contour of the HSM in Principal Stress Space for Cohesionless Soil (Schanz et al. 1999).

Figure 2-35 shows yield surface in principal stress space, and **Figure 2-34** only shows simple yield lines. Mohr-Coulomb failure criterion has a hexagonal shape, and it can be seen in both figures, but the main difference is yield cap expansion depends on preconsolidation stress, while shear yield loci expansion can be taken up to ultimate Mohr-Coulomb failure surface. Hardening Soil Model works under two important parameters described in this chapter, such as plastic shear strain and plastic

volumetric strain (γ^p , ${\varepsilon_v}^{pc}$respectively). This model takes a flow rule which is a linear relationship of both parameters:

$$\varepsilon_v{}^p = sin\psi_m \gamma^p \tag{72}$$

Where ψ_m is the mobilized dilatancy angle, defined for this constitutive model as:

For $sin\varphi_m < 3/4 sin\varphi$ $\psi_m = 0$ (73)

For $sin\varphi_m \geq 3/4 sin\varphi \; and \; \psi > 0$ $sin\psi_m = \max(\frac{sin\varphi_m - sin\varphi_{cv}}{1 - sin\varphi_m sin\varphi_{cv}}, 0)$ (74)

For $sin\varphi_m \geq 3/4 sin\varphi \; and \; \psi \leq 0$ $\psi_m = \psi$ (75)

If $\varphi = 0$ $\psi_m = 0$ (76)

Where φ_{cv} is the critical state friction angle and φ_m is them mobilized friction angle, defined as:

$$sin\varphi_m = \frac{{\sigma'}_1 - {\sigma'}_3}{{\sigma'}_1 + {\sigma'}_3 - 2c \; cot\theta} \tag{77}$$

Above equations corresponds to the stress-dilatancy theory (Rowe 1962), which exposes that soil tends to dilatate for high stress ratios ($\varphi_m > \varphi_{cv}$), and with small stress ratios ($\varphi_m < \varphi_{cv}$) soil tends to contract. This can be understood as dense soils will expand under low consolidation stresses and loose soil will contract under high consolidation stresses. φ_m will be equal than failure angle φ when failure occurs, shown by the next relationship:

$$sin\varphi_{cv} = \frac{sin\varphi - sin\psi}{1 - sin\varphi sin\psi} \tag{78}$$

The relationship between these angles (frictional and dilatancy) shows the equivalency to plastic potential functions. Soil reaches a state of critical density after an extensive shearing process, that is when dilatancy tends to stop, and this behavior is defined by Hardening Soil Model as Dilatancy Cut-Off, and is controlled by initial and maximum void ratio (e_{min} and e_{max}) related to the dilatancy angle as well.

For $e < e_{max}$ $sin\psi_m = \frac{sin\varphi_m - sin\varphi_{cv}}{1 - sin\varphi_m sin\varphi_{cv}}$

For $e > e_{max}$ $\psi_{mob} = 0$

There is also a relationship between void ratio and volumetric strain, where an increment of ε_v is negative for dilatancy:

$$-\left(\varepsilon_v - \varepsilon_v{}^{init}\right) = \ln\left(\frac{1+e}{1+e_{init}}\right)$$

Maximum void ratio corresponds to a material in a critical state, and the initial void ratio correspond to the in-situ one. Dilatancy angle tend to be zero when maximum void ratio is reached. When modeling soil behavior, maximum void ratio can be an input parameter, but generally it is not used out of the context of Hardening Soil Model.

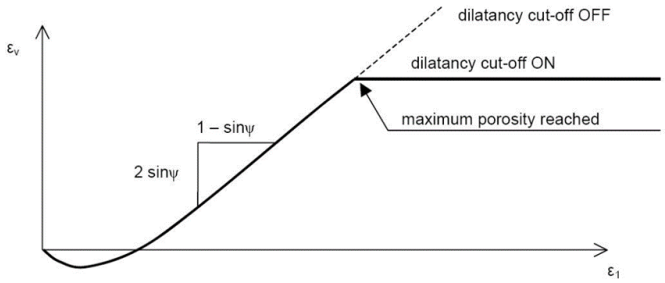

Figure 2-36. Resulting Strain Curve for a Standard Drained Triaxial Test When Including Dilatancy Cut-Off (Schanz et al. 1999).

Hardening Soil Model is an advanced constitutive soil model, but it has its own limitations, as any other of them. There will always be several features and parameters of real soil behavior that one single model can not take into account. This model does not consider the softening produced by soil dilatancy and its effects.

This is a model which works into the isotropic framework, that is why does not considers hysteric or cyclic loading, it also has a lack of accuracy when differencing large stiffness at small strains and reduced stiffness at normal engineering strain levels. Because of this, user must have a complete knowledge of the project and strain levels will be produced, since that level will be the resource to define (select) stiffness parameters to proceed with the model. Hardening Soil Model works with a stiffness matrix, which is decomposed in each parameter and calculation step, that is why generally calculation times with this model become longer.

2.4.3 Hypoplastic Model

Hypoplasticity is an advanced constitutive model captures the nonlinear behavior of fine grained soils at large strains under different stress paths, within the field of critical state soil mechanics. This model does not consider conventional process of decomposing strains in elastic and plastic groups, so does not work with yield surface and plastic potential definitions.

This model is focused for clays, and was proposed by (Mašín 2005)(Mašín 2012)(Mašín 2014)(Mašín 2015) but in its first versions proposed, it was focused on granular materials (Kolymbas et al. 1996) and (von Wolffersdorff 1996), later extended to fine grained soils also (Niemunis and Krieg 1996)(Niemunis and Herle 1997)(Niemunis 2002)(Niemunis 2003), but there was a lack of accuracy at predicting behavior under anisotropic stress states, and defining shear stiffness at small strains.

A new constitutive parameter that controls the ratio between initial bulk and shear modulus was included by (Herle and Kolymbas 2004) looking for improve last deficiency mentioned. When intergranular strain concept was included, soil behavior subjected to cyclic loads and small strains was better represented. This model was improved by (Mašín 2014) by considering small strain stiffness anisotropy by working with stiffness tensor. Isotropic loading/unloading tests (beyond the preconsolidation pressure) were used for the calibration of the main basic model parameters.

Five main soil parameters are the basis of the basic Hypoplasticity constitutive model: $N, \lambda^*, k^*, v_{pp}$ and φ'. These parameters are all determined from standard laboratory tests, which represents a great advantage. k^* parameter represents the slope of isotropic unloading line, while slope and position of the isotropic normal compression line are represented by N and λ^*parameters, typically obtained from isotropic compression tests, or even one-dimensional constraint compression test such as oedometer test, could be useful to obtain them.

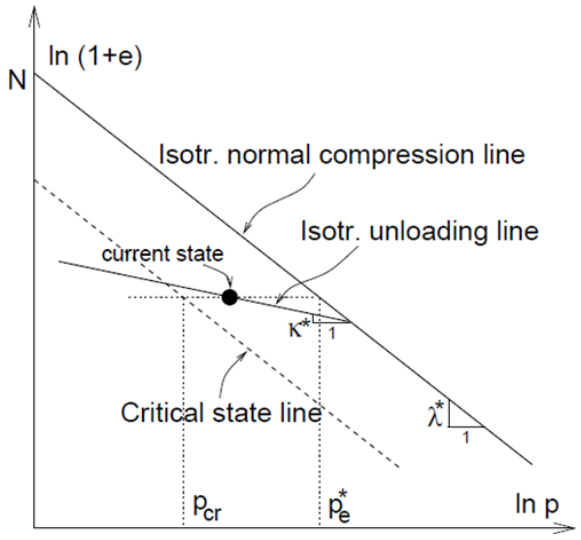

Figure 2-37. Definition of parameters: N, λ*, κ*, taken from (Mašín 2005)

Table 2-9. Basic and advanced Hypoplastic parameters.

#	Symbol	Parameter name	unit
1	φc	Critical state friction angle	kN/m²
2	Pt	Shift of the mean stress due to cohesion	kN/m²
3	λ	Slope of the isotropic normal compression line	-
4	κ	Slope of isotropic unloading line	-
5	N	Position of the isotropic normal compression line	-
6	νpp	Control of the shear stiffness	-
7	αG	Ratio of horizontal and vertical shear modulus	-
8	Ag	Very small strain shear stiffness parameter	-
9	ηg		-
10	mrat	Intergranular strain concept parameter	-
11	R	Intergranular strain concept parameters	-
12	βr		-
13	χ		-

Relationships for the soft to medium stiff clays is marked for an almost constant variation with water content. For the stiff clays, the variation is almost linear with equations presented in **Figure 2-38**, in which is shown also a summary of N, λ^*, and / $\lambda^* / k^*$for stiff clays layers, obtained from One Museum Park West project (Arboleda-Monsalve 2014). Shear stiffness is related to the bulk-to-shear stiffness ratio r (Sarabia 2012) and it is controlled by parameter ν_{pp}, obtained from parametric

analysis. This parameter can be evaluated in terms of other basic model parameters calibrated from laboratory tests, as follows:

$$v_{pp} = \frac{3r(\lambda^* + k^*) - 4k^*}{6r(\lambda^* + k^*) + 4k^*} \quad (79)$$

Parametric analysis allowed this expression are based on stress-strain curves of undrained triaxial extension and compression tests. Considering a constant volume, friction angle φ' become a natural water content (w_n) and overconsolidation ratio (OCR) function, and for Blodgett and Deerfield layers, the K_0- consolidated triaxial compression tests become the basis for obtaining the normalized undrained shear strength ($S_{uTXC}/\sigma_{v0}{}'$), which can be expressed as (Finno and Chung 1993).

$$\frac{S_{uc}}{\sigma_{v0}{}'} = 0.46(0.9 - w_n)OCR^{0.9} \quad (80)$$

The ratio $S_{uTXC}/\sigma_{v0}{}'$ proposed by (Wroth 1984)for isotropic compression triaxial tests was later modified by (Wroth 1984) and was given in terms of OCR and φ', as follows:

$$\frac{S_{uc}}{\sigma_{v0}{}'} = \frac{1}{6}M(1 + 2K_0)\left(\frac{\alpha_R OCR}{2}\right)^{\Lambda} \quad (81)$$

$$M = \frac{6\sin\varphi'}{3 - sin\varphi'} \quad (82)$$

$$\alpha_R = \frac{9(1 - K_{0nc})^2 + M^2(1 + 2K_{0nc})^2}{M^2(1 + 2K_0)(1 + 2K_{0nc})} \quad (83)$$

$$K_0 = (1 - sin\varphi')OCR^{sin\varphi'} \quad (84)$$

Where M is the critical state parameter M and Λ is the plastic volumetric ratio taken as 0.75 for most clays. **Figure 2-38** shows φ' input values for triaxial stress paths, and the relation for the OCR values from 1 to 2, which result in a difference of 2 degrees in φ' for these two states. Above equations are the ones allow to obtain the relationship between critical state frictional angle, natural water content, and OCR.

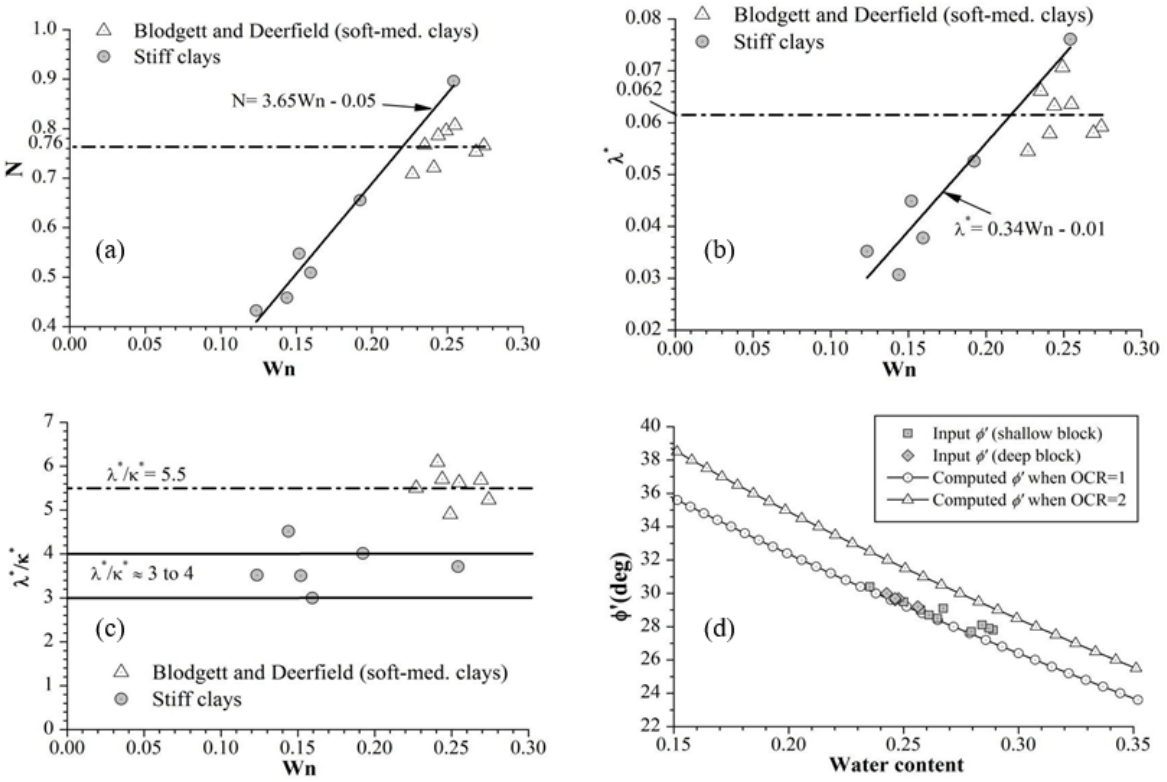

Figure 2-38. Parameters for basic model: (a) position of isotropic normal compression line (N); (b) slope of isotropic normal compression line (λ*); (c) ratio isotropic loading and unloading line (λ*/κ*); (d) friction angle at constant volume (φ').

Before Hypoplasticity constitutive model were enhanced to estimate soil behavior for strain levels lower than 0.1% with including intergranular strain concept, it was only useful for strains levels greater than that magnitude. With the new concept, a new variable which represents the deformation of the interface layers between soil particles was added, this parameter represents intergranular strain and is denoted as δ, which allowed to model stress history of the soil. Overall response comprises both particle rearrangement of soil skeleton and deformation of the intergranular interface layer between grains, when soil is subjected to continuous loads. Seven additional parameters are introduced in the constitutive model, as the intergranular strain concept considers small strain behavior of soil: $\alpha_G, A_G, n_g, m_{rat}, R, \beta_r$ and χ. The ratio of horizontal and vertical shear modulus under cross-anisotropic nature is represented by α_G. For Chicago clays, this parameter varies between 1.1 and 1.2 according to (Kim and Finno 2012). Very small strain shear stiffness (calibrated with bender elements in triaxial tests) are defined by A_G and n_g. Initial shear stiffness and effective mean normal stress are related between them, and that dependency can be expressed as:

$$G_{vh} = p_r A_g \left(\frac{p'}{p_r}\right)^{n_g} \quad (85)$$

G_{vh} is the shear stiffness and p_r is a reference pressure defined as 1 kPa.

Normal effective stress p' and deviatoric stress q are the stress invariants reported. Volumetric strain ε_{vol} and shear strain ε_{sh} represent the strain invariants. For axisymmetric conditions, these parameters can be defined as:

$$p' = (\sigma'_a + 2\sigma'_r)/3 \quad (86)$$

$$q = \sigma'_a - \sigma'_r \quad (87)$$

$$\varepsilon_{vol} = \varepsilon_a + 2\varepsilon_r \quad (88)$$

$$\varepsilon_{sh} = (2/3)\,(\varepsilon_a - \varepsilon_r) \quad (89)$$

Where σ'_a and σ'_r correspond to the axial and radial effective stresses, ε_{vol} and ε_{sh} correspond to the axial and radial strains, respectively. **Figure 2-39** shows enhanced model parameters, considering the addition of intergranular strain tensor. These parameters influence the stiffness degradation of soils, and this influence was analyzed under parametric studies by (Mašín 2015) who defined variation ranges for typical soils.

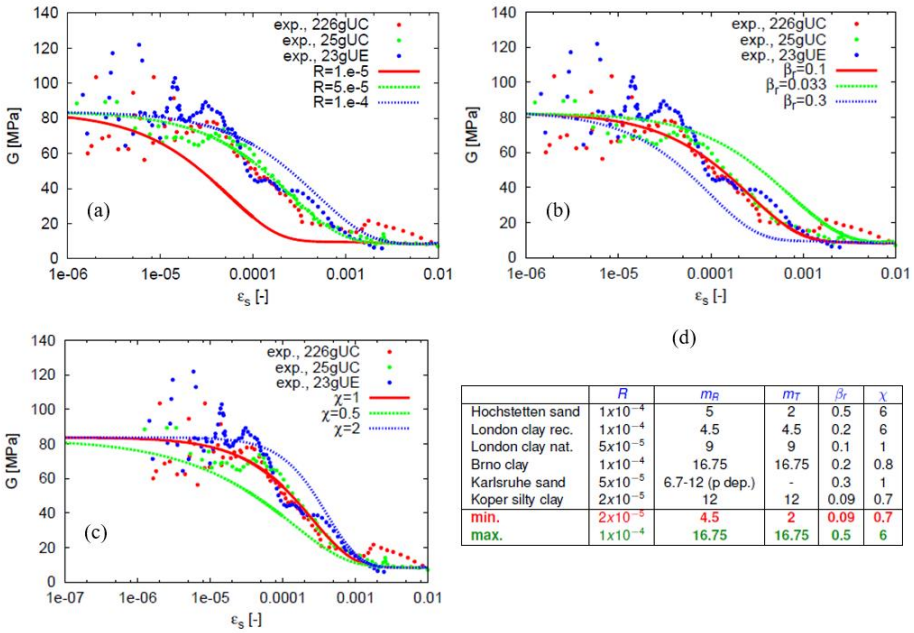

	R	m_R	m_T	β_r	χ
Hochstetten sand	$1x10^{-4}$	5	2	0.5	6
London clay rec.	$1x10^{-4}$	4.5	4.5	0.2	6
London clay nat.	$5x10^{-5}$	9	9	0.1	1
Brno clay	$1x10^{-4}$	16.75	16.75	0.2	0.8
Karlsruhe sand	$5x10^{-5}$	6.7-12 (p dep.)	-	0.3	1
Koper silty clay	$2x10^{-5}$	12	12	0.09	0.7
min.	$2x10^{-5}$	4.5	2	0.09	0.7
max.	$1x10^{-4}$	16.75	16.75	0.5	6

Figure 2-39. Calibration of constitutive parameters for HC model with intergranular strains: (a) size of the elastic range, R, (b) degradation rate parameter, β, (c) degradation rate parameter, χ, (d) parameters for different soils (Mašín 2015).

3. NUMERICAL ANALYSIS OF URBAN COFFERDAM AT ANONYMOUS SITE

In this research, a two-dimensional (2D) finite element model of the cofferdam was constructed under axisymmetric conditions using the software Plaxis 2D 2016.1. It was used to simulate the stages of excavation, and the construction of the reinforced concrete ring beams that support the cofferdam. The model wished the sheet pile wall in place, it means that the alteration of pore pressures and state of tensions in the soil due to pile driving was not included in the numerical analysis. The cofferdam works as a temporary support system to allow the construction of the foundation caissons and rigid concrete core that would support the superstructure. This model is called Base Model throughout this work.

The numerical model takes into account the time-dependent effects of the concrete material that forms the ring beams of the cofferdam. Specifically, aging (with time dependency of elastic stiffness E_1/E_{28} and time dependency of strength f_{c1}/f_{c28}), creep (with creep coefficient φ^{cr}) and shrinkage (with shrinkage coefficient $\varepsilon_{\infty}^{shr}$), as well as their variations with temperature, are considered.

The Shotcrete constitutive model was employed to captures the nonlinear behavior of the concrete elements. The Shotcrete model formulation and theoretical basis are discussed in section 2.4.1. The advanced constitutive soil models Clay hypoplasticity and Hardening Soil Model were used to simulated the small stress-strain response of the soils that make up the local stratigraphic profile, which consists mainly of loose to dense sands at the surface and soft to very stiff clays in depth.

In this thesis, the horizontal displacements were taken as the comparing parameter to fit the numerical response to the observed performance during construction (see section 2.2.6).

3.1 Base Model Including all Time-Dependent Effects

3.1.1 Type of Analysis in the Model

Due to the circular geometry of the cofferdam and the assumed location of the loads acting on it, see **Figure 3-1**, an analysis under axisymmetric conditions is implemented in the software Plaxis 2D 2016.1. The use of an axisymmetric model reduces considerably the computational times compared to an equivalent three-dimensional (3D) model.

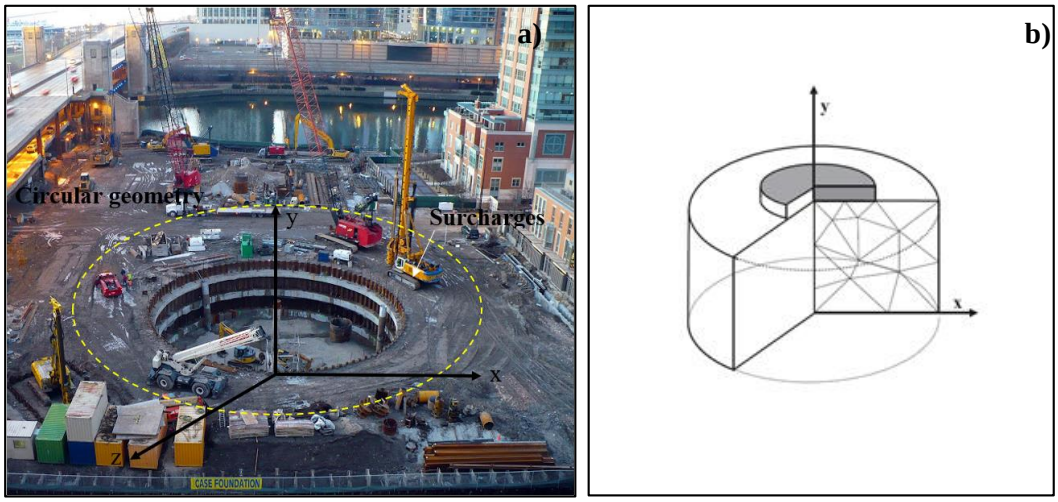

Figure 3-1. a) Field conditions and b) Axisymmetric conditions scheme (Brinkgreve et al. 2011).

Under this analysis condition the shear stresses on a circumferential plane (z) are zero and the stress state on any diametral plane is the same. Additionally, the radial deformation induces a circumferential deformation. In Plaxis, it is denoted by equation (90). Equation (91) shows as an example of an elastic linear material the stiffness matrix in conditions of axisymmetric analysis, which is modified in each constitutive model, maintaining the coordinate system.

$$\varepsilon_{zz} = \frac{1}{r} U_x \tag{90}$$

$$\begin{bmatrix} \sigma'_{XX} \\ \sigma'_{YY} \\ \sigma'_{ZZ} \\ \sigma'_{XY} \end{bmatrix} = \frac{E}{(1-2\nu')(1+\nu')} \begin{bmatrix} 1-\nu' & \nu' & \nu & 0 \\ \nu & 1-\nu' & \nu & 0 \\ \nu & \nu & 1-\nu' & 0 \\ 0 & 0 & 0 & 1/2-\nu' \end{bmatrix} \begin{bmatrix} \varepsilon_{XX} \\ \varepsilon_{YY} \\ \varepsilon_{ZZ} \\ \gamma_{XY} \end{bmatrix} \tag{91}$$

Where:

- E is the elastic modulus
- ν is the Poisson coefficient
- σ' are stresses under axisymmetric conditions
- ε and γ are strains under axisymmetric conditions

Figure 3-2 shows a scheme of the radial section of the axisymmetric model. This presents the soil stratification of the study site associated with the Chicago City Datum (CCD), cofferdam structural elements (reinforced concrete ring beams and sheet piles), also the surface surcharge, water table position, and finally model limits and axis of axial symmetry.

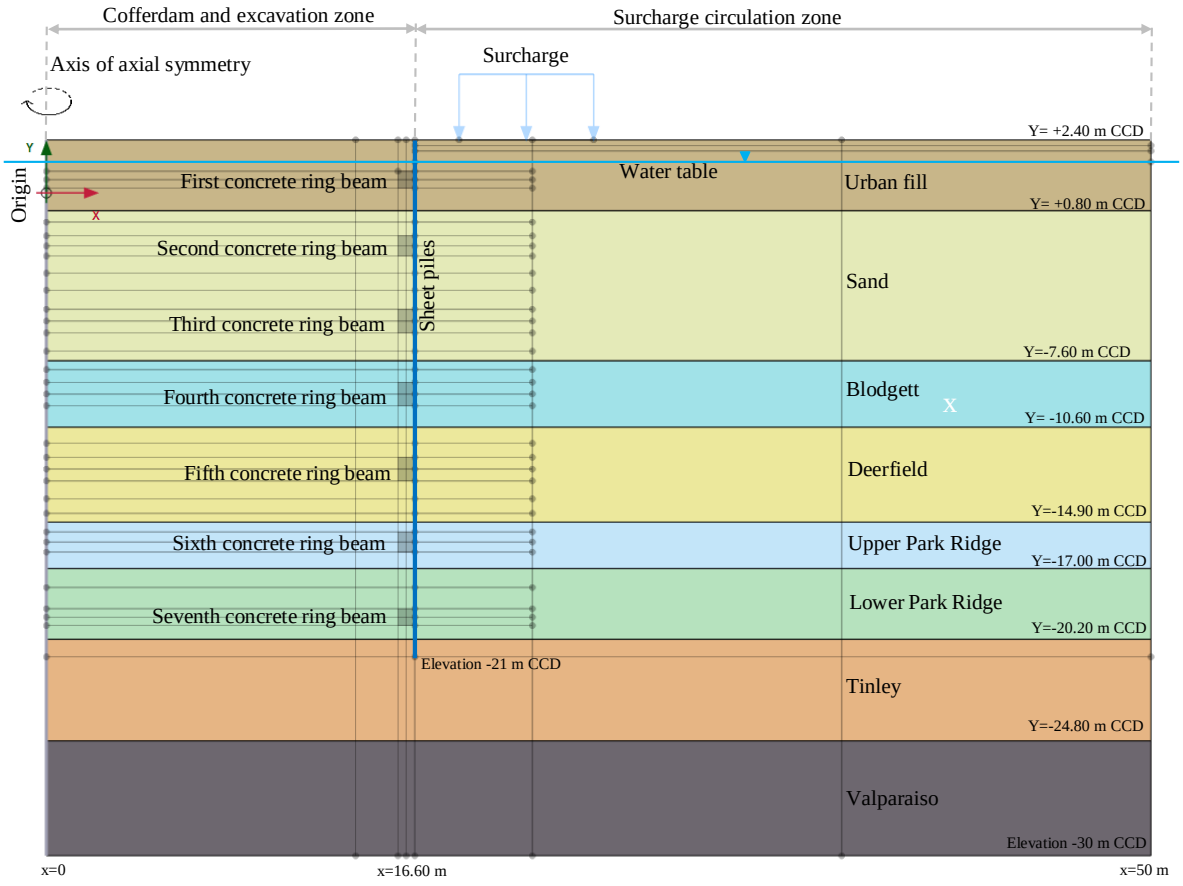

Figure 3-2. Axisymmetric model illustrating soil stratigraphy, concrete ring beams, and sheet piles.

3.1.2 Mesh and Boundary Conditions

The finite element model and mesh used to model the cofferdam excavation is shown in **Figure 3-3**This figure shows the concrete ring beam cross sections, sheet pile wall location, the different soil layers, and the water table. The mesh was designed with a higher degree of refining around the sheet piles, concrete ring beams and excavation zones. **Figure 3-4** shows the refinement of the mesh around the concrete ring beams.

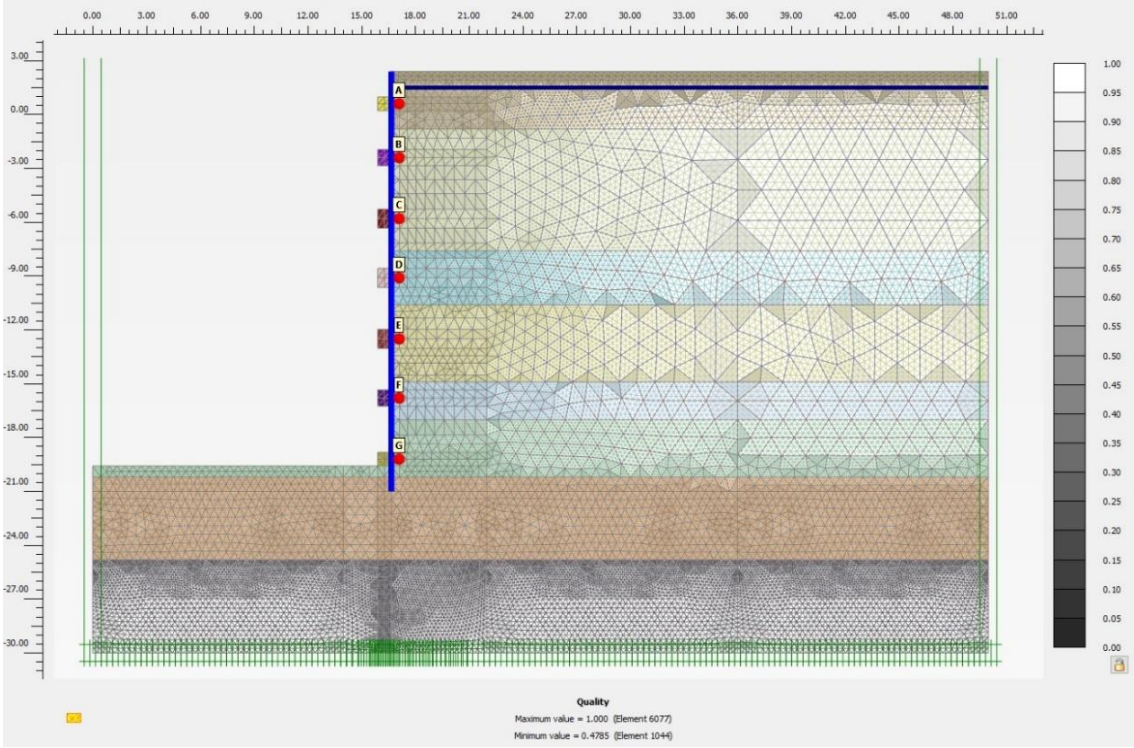

Figure 3-3. Finite element mesh used in the model.

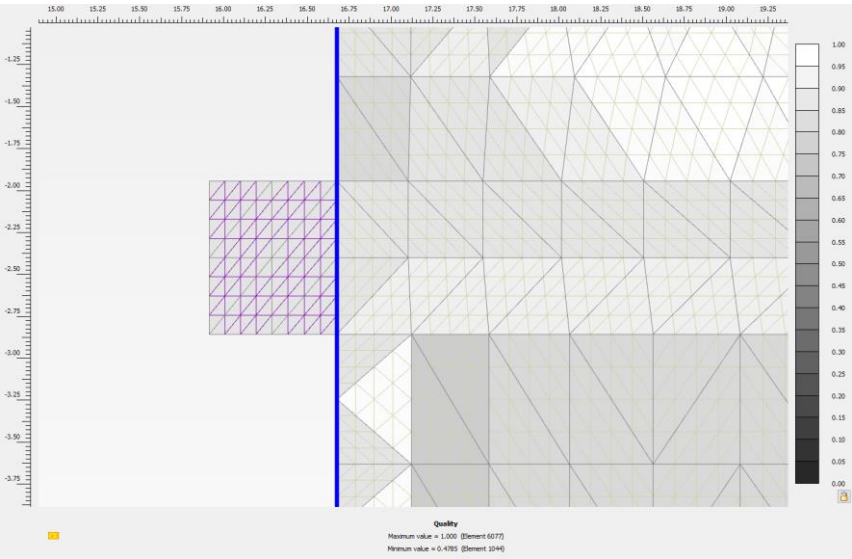

Figure 3-4. Finite element mesh detail in the concrete ring beam.

Seven (7) points of interest are presented for the calculation of tensions and displacements behind the sheet piles denominated A, B, C, D, E, F and G in Figure 3-3**.** The location of these points corresponds to the elevation of each ring beam. The data obtained in these calculation points will be compared with the observed field performance in order to validate the base model.

15-node elements are used to form the model mesh. In the Plaxis software, this element contains 15 nodes and 12 internal stress points. This type of element uses a fourth order interpolation for displacement calculations, a characteristic that gives better precision and yields results of high quality stress in difficult geotechnical problems. For axisymmetric model conditions, it is recommended to use a 15-node finite element mesh (Brinkgreve et al. 2011). Figure 3-5 shows the detail of the element type and mesh used in the model. The opacity scale in the finite element mesh shown in Figure 3-3 indicates the quality of the mesh. It increases as the sides of the triangles of 15 nodes become equal. In the numerical model 68681 nodes and 102228 stress points were implemented.

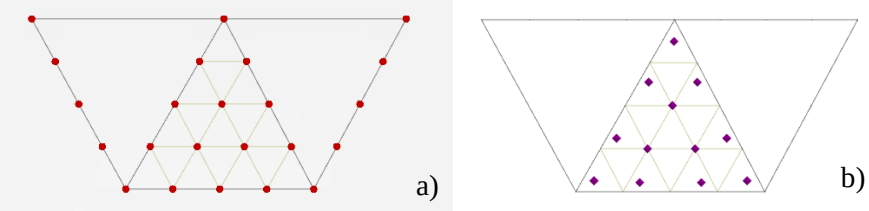

Figure 3-5. 15-Node element in Plaxis 2D, a) Nodes and b) Stress points

The boundary conditions employed in the models define a rigid base at an elevation of -30 m, and movement restriction in the Y direction in the axis of axial symmetry, and external limit of the model. More specifically, the model boundary conditions were set as follows:

- Boundary X Minimum: Normally fixed
- Boundary X Maximum: Normally fixed
- Boundary Y Minimum: Fully fixed
- Boundary Y Maximum: Free

3.1.3 Surcharge

In the base model a 55-kPa-surcharge was incorporated to represent the induced load of stock-pile material around the cofferdam and the operating weight of drilling rig equipment during cofferdam construction. An approximately 3-m-high stock-pile of excavated material as well as heavy-load cranes were identified in the project photographic records. **Figure 3-6** shows the distribution of drilling rig equipment over the track area, in this way the surcharge was considered perpendicular to the cofferdam perimeter wall. The surcharge was applied in the base model at phase 19 (RB3 Installation), see **Table 3-6**. Analysis model under axisymmetric (2D) conditions has a restriction for capturing the surcharges tridimensional effect, therefore the surcharges application in the numerical model in this research are taken as a technical simplification, which showed results consistent with field performance.

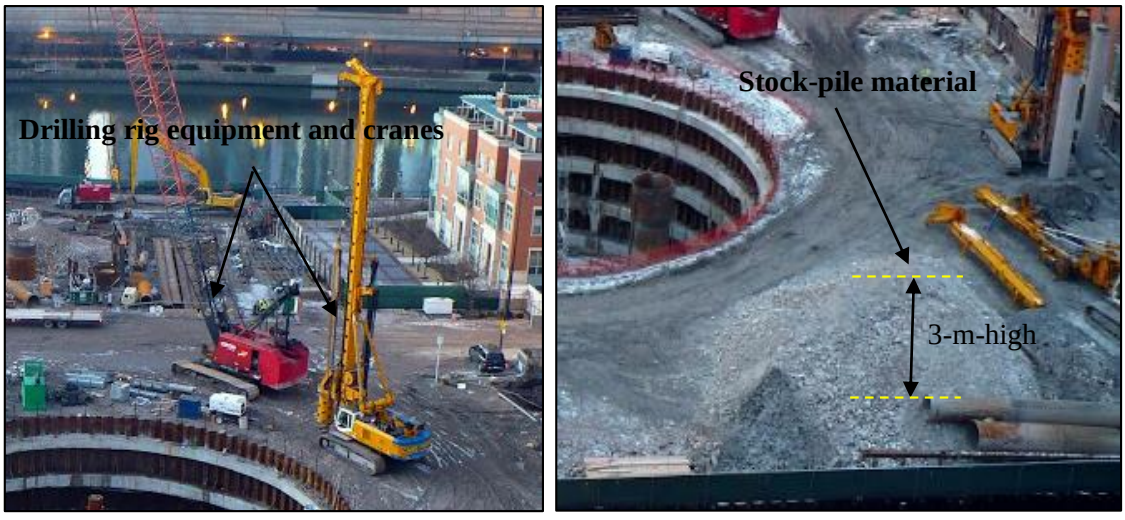

Figure 3-6. Equivalent Krane Bauer BS 100 Surcharge and stock-pile material.

3.1.4 Soil and Structural Properties

Table 3-1 presents the model parameters of the strata that make up the stratigraphy of the cofferdam site. The Hardening Soil Model is used to represent the nonlinear behavior of sand layers, called urban fill and sand in the base model. The hardening soil parameters for the sands were initially proposed by (Blackburn 2005) based on inverse optimization of the Ford Engineering Design Center excavation.

According to (Finno and Calvello 2005) these inverse analyzes, combined with field observations of the excavation performance, are effective to predict horizontal ground movements in the Chicago area. Specifically, the authors developed an inverse analysis algorithm, which compares the deformations around the excavation calculated in the software Plaxis with those registered in field monitoring. The inverse analysis process consists on executing the modeling calculations several times, where the reference secant stiffness parameter E_{50}^{ref} is optimized. The process is finalized when the difference between the soil deformations calculated and field observations is minimized.

Table 3-1. Hardening soil parameters for Urban Fill and Loose to Dense sands.

Name	**Urban Fill**	**Sand**	**unit**
Model	Hardening Soil	Hardening Soil	
Type	Drained	Drained	
γ unsat	18.90	18.90	kN/m³
γ sat	18.90	18.90	kN/m³
e init	0.50	0.50	-
E_{50}^{ref}	7185	7185	kN/m²
E_{oed}^{ref}	7185	7185	kN/m²
E_{ur}^{ref}	21560	21560	kN/m²
power (m)	0.50	0.50	-
C'_{ref}	1.00	1.00	kN/m²
φ' (phi)	32.00	37.00	°
ψ	0	5	°
ν'_{ur}	0.20	0.20	-
P_{ref}	5.00	5.00	kN/m²
K_0^{nc}	0.47	0.40	-
Rf	0.90	0.90	-

To capture the nonlinear behavior of the clays the hypoplasticity clay model, including the concept of intergranular deformation (Mašín 2005), was used in the numerical analysis. **Table 3-2** summarizes the parameters employed for the behavior simulation of the clay layers that make up the stratigraphic profile. These parameter are taken from (Arboleda-Monsalve 2014) and were calibrated based on index properties and results of triaxial stress probes and oedometers, completed as part of the laboratory testing program of the One Museum Park West Excavation project located in the Chicago area.

Table 3-2. Hypoplasticity parameters for Chicago clays.

Name	**Blodgett**	**Deerfield**	**UpPRidge**	**LowPRidge**	**Tinley**	**Valparaiso**	**unit**
Model Type	Hypoplastic Undrained	Hypoplastic Undrained	Hypoplastic Undrained	Hypoplastic Undrained	Hypoplastic Undrained	Hypoplastic Undrained	
γ_{unsat}	18.90	18.90	18.90	18.90	19.60	19.60	kN/m³
γ sat	18.90	18.90	18.90	18.90	19.60	19.60	kN/m³
e init	0.86	0.63	0.50	0.45	0.60	0.60	-
φc	25	31.70	36.00	37.80	35.80	40.00	kN/m²
Pt	25	25	25	25	25	25	kN/m²
λ	0.06200	0.06200	0.05500	0.05000	0.06500	0.06800	-
κ	0.01130	0.01130	0.01000	0.00500	0.00500	0.01200	-
N	0.76000	0.76000	0.62000	0.55000	0.75000	0.75000	-
νpp	0.1500	0.1500	0.1500	0.1500	0.1500	0.1500	-
αG	1.10	1.10	1.10	1.10	1.10	1.10	-
Ag	4100	4100	4100	4100	4100	4100	-
ηg	0.60	0.60	0.60	0.60	0.60	0.60	-
mrat	1.000	1.000	1.000	1.000	1.000	1.000	-
R	0.00005	0.00005	0.000024	0.000024	0.000024	0.000024	-
βr	0.18	0.18	0.18	0.18	0.18	0.18	-
χ	1.30	1.30	1.30	1.30	1.30	1.30	-

The non-linear behavior of the concrete and its time-dependent effects was modeled with the Shotcrete model (Schädlich and Schweiger 2014b). The Shotcrete model takes into account time dependency for strength and stiffness. It also includes the effects of shrinkage and creep, and considers strain hardening/softening for compression. The main concrete parameters (f'_c) of the ring beams were obtained from compressive strength laboratory tests completed during construction. **Table 3-3** summarizes the average results of compressive strength.

The summary of all the parameters required as input in the Shotcrete model is presented in **Table 3-4**. The creep and shrinkage coefficients used to model the concrete ring beams were determined

as a function of the compressive strength and environmental conditions at each construction period, where the volume-to-exposed surface ratio is taken into account as well as relative humidity and temperature. The formulation to obtain each coefficient is explained in Sections 2.3.3 and 2.3.4. Time dependency of elastic stiffness E_1/E_{28} and time dependency of strength f_{c1}/f_{c28} coefficients were determined from the maturity curves of each concrete beam, which were presented in Sections 2.3.1 and 2.3.2. In order to build the complete excavation model and verify stability conditions, the parameters of rings 6 and 7 were assumed, assigning them the parameters of rings 2 and 1, respectively.

Table 3-3. Results of concrete compressive strength tests.

Ring Beam #	Compressive strength f_{ci} [MPa]	Area A_c[mm²]	Exposed perimeter u[in]
1	55.49	580644	2286.00
2	53.53	696772.8	2438.40
3	65.28	812901.6	2590.80
4	62.71	812901.6	2590.80
5	63.44	812901.6	2590.80
6		no data available	
7		no data available	

Table 3-4. Shotcrete parameters of concrete ring beams.

Name	**RB1**	**RB2**	**RB3**	**RB4**	**RB5**	**RB6**	**RB7**	**unit**
Model	Shotcrete	Shotcrete	Shotcrete	Shotcrete	Shotcrete	Shotcrete	Shotcrete	
Type	Non-porous	Non-porous	Non-porous	Non-porous	Non-porous	Non-porous	Non-porous	
γ unsat	24	24	24	24	24	24	24	kN/m³
E_{28}	38060000	37610000	40180000	39647	39800	37610000	38060000	kN/m²
ν	0.200	0.200	0.200	0.200	0.200	0.200		-
$f_{c,28}$	55490	53530	65280	62708	63437	53530	55490	kN/m²
$f_{t,28} = 0.10*f_{c,28}$	2520	2470	2730	2680	2760	2470	2520	kN/m²
ψ	0	0	0	0	0	0	0	°
E_1/E_{28}	0.3831	0.3828	0.3821	0.4512	0.3319	0.4001	0.6205	-
$f_{c,1}/f_{c,28}$	0.1371	0.1370	0.1368	0.1915	0.1038	0.1522	0.3791	-
$f_{c0n} = f_{c0}/f_{c,28}$	0.00	0.00	0.00	0.00	0.00	0.00	0.00	-
$f_{cfn} = f_{cf}/f_{c,28}$	0.26	0.27	0.20	0.22	0.20	0.27	0.26	-
$f_{cun} = f_{cu}/f_{c,28}$	0.00	0.00	0.00	0.00	0.00	0.00	0.00	-
	-0.010	-0.010	-0.012	-0.012	-0.010	-0.010	-0.012	-
ε_{cp}^{p}	-0.0010	-0.0010	-0.0011	-0.0011	-0.0011	-0.00100	-0.0010	-
	-0.00095	-0.00096	-0.00100	-0.00098	-0.00097	-9.50E-04	-0.00095	-
$G_{c,28}$	70.00	70.00	70.00	70.00	70.00	70.00	70.00	kN/m
f_{tun}	0	0	0	0	0	0	0	-
$G_{t,28}$	0	0	0	0	0	0	0	kN/m
L_{eq}	0.00	0.00	0.00	0.00	0.00	0.00	0.00	m
α	0	0	0	0	0	0	0	-
φ_{max}	37	37	37	37	37	37	37	°
φ^{cr}	1.380	1.420	1.220	1.390	1.320	1.460	1.490	-
t_{50}^{cr}	9.00	9.00	9.00	9.00	9.00	9.00	9.00	day
$\varepsilon_{\infty}^{shr}$	-0.000203	-0.000192	-0.000205	-0.000193	-0.000198	-0.000195	-0.000210	-
t_{50}^{shr}	50	50	50	50	50	50	50	day
γ_{fc}	1.0	1.0	1.0	1.0	1.0	1.0	1.0	-
γ_{ft}	1.0	1.0	1.0	1.0	1.0	1.0	1.0	-
t_{hydr}	51	54	54	59	62	56	22	day
E_{oed}^{ref}	15000	15000	15000	15000	15000	15000	15000	kN/m²
C_{ref}	8721	8721	8721	8721	8721	8721	8721	kN/m²
φ' (phi)	54.9	54.9	54.9	54.9	54.9	54.9	54.9	°

In order to validate the Shotcrete model response and its predictions in terms of the Normalized Hardening Parameter, H_c, elastic strains, ε_c, compressive strength, f'_c and elastic modulus, E, a Plaxis 2D finite element model of each type of ring beam cross section was created. Time stages were included without load allowing to evidence the aging of the concrete. **Figure 3-7** shows the concrete ring beam numerical model used for the validation analyses. Due to the same geometry and small difference that exists between compressive strength of ring beams 3, 4 and 5, these were standardized in a single validation model.

c)

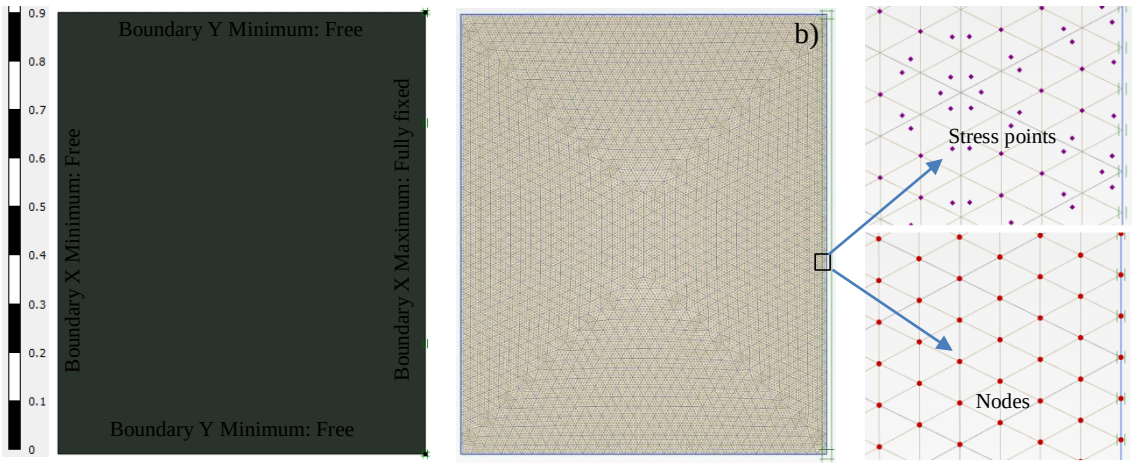

Figure 3-7. Concrete ring beam numerical model, a) Geometry and boundary conditions, b) finite element mesh and c) Increased view of the mesh.

The validation results are shown in **Figure 3-8**, **Figure 3-9** and **Figure 3-10** for ring beams 1, 2 and 3 to 5, respectively. The figures present the variation of the compressive strength, f'_c, with H_c, strain and time. Also include in the figures is the evolution in time for the elasticity modulus of the concrete. It can be seen that the Shotcrete model allows to capture load history of the concrete in a more realistic way for loading and reloading during the aging of the concrete.

The predictions of compressive strength and modulus of elasticity are validated with the formulations proposed by (Collins and Mitchel 1991) and (fib – fédération internationale du béton 2013). Note also that two different curves for the Shotcrete model are included in the figures. One represents the obtained values from the Plaxis validation ring beam model, and the other is calculated by coding the Shotcrete model formulation in a simple Excel spreadsheet (See Appendix A). It allows for a simpler and faster calibration of the model parameters.

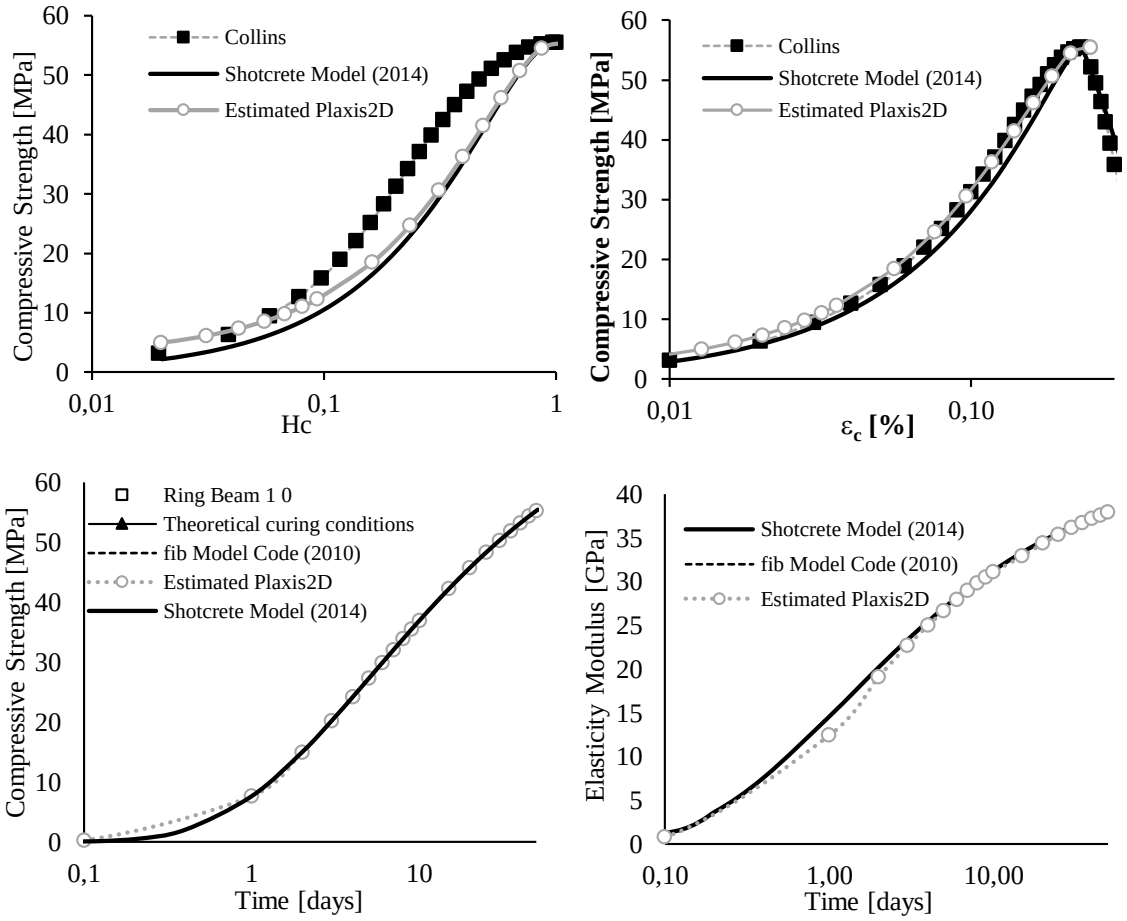

Figure 3-8. Compressive Strength versus Hc; Compressive Strength versus ε_c; Compressive Strength versus Time and Elasticity Modulus versus Time, Ring Beam 1.

The validation curves indicate an adequate adjustment for each analyzed parameter, especially for compressive strength and elastic modulus, where the three implemented methodologies present basically the same trend. Similar behavior is observed for the compressive resistance versus elastic deformation curve. The numerical compressive strength versus hardening parameter responses present slightly larger discrepancies with respect to the methodology proposed by (Collins and Mitchel 1991). However, the numerical results are acceptable.

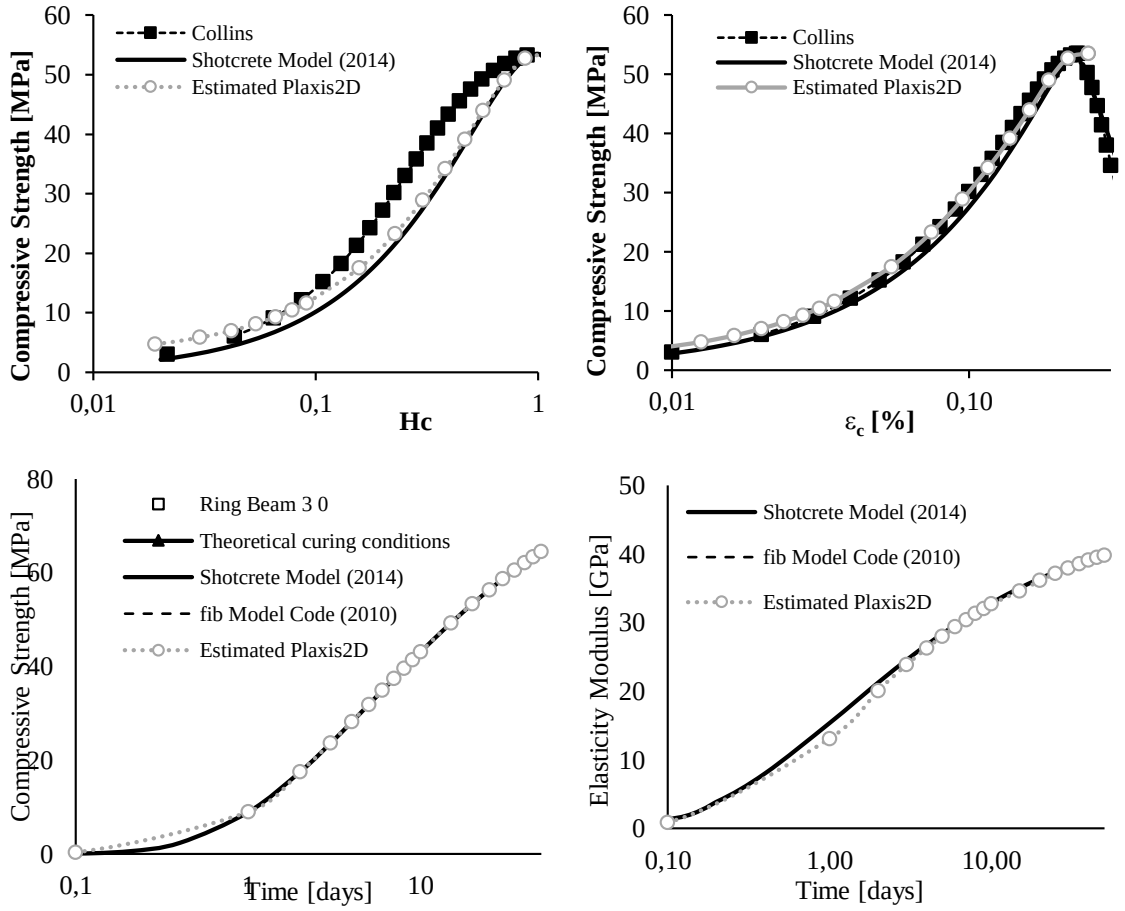

Figure 3-9. Compressive Strength versus Hc; Compressive Strength versus ε_c; Compressive Strength versus Time and Elasticity Modulus versus Time, Ring Beam 2.

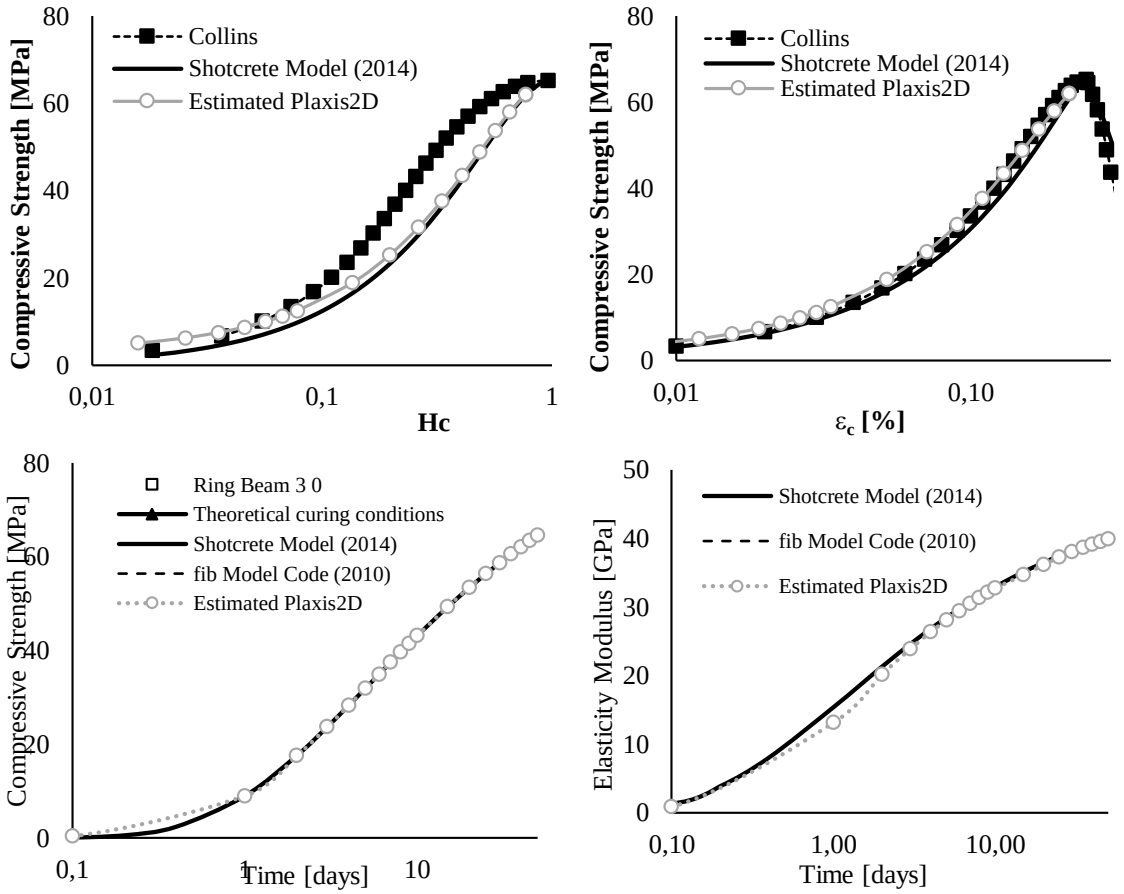

Figure 3-10. Compressive Strength versus Hc; Compressive Strength versus ε_c; Compressive Strength versus Time and Elasticity Modulus versus Time, Ring Beam 3 to 5.

The final coefficients of creep and shrinkage obtained from the Shotcrete model implemented in Plaxis 2D were also validated with the (Fédération Internationale du Béton 2010) and (American Concrete Institute 2008) . The validation results are presented in **Figure 3-11**, **Figure 3-12** and **Figure 3-13** for ring beams 1 and 7, 2 and 6, and 3 to 5, respectively. Note in the figures that considerable differences during the creep and shrinkage coefficient evolution in time are obtained. However, a good agreement is obtained for the final creep and shrinkage coefficients employed to calculate time-dependent strains.

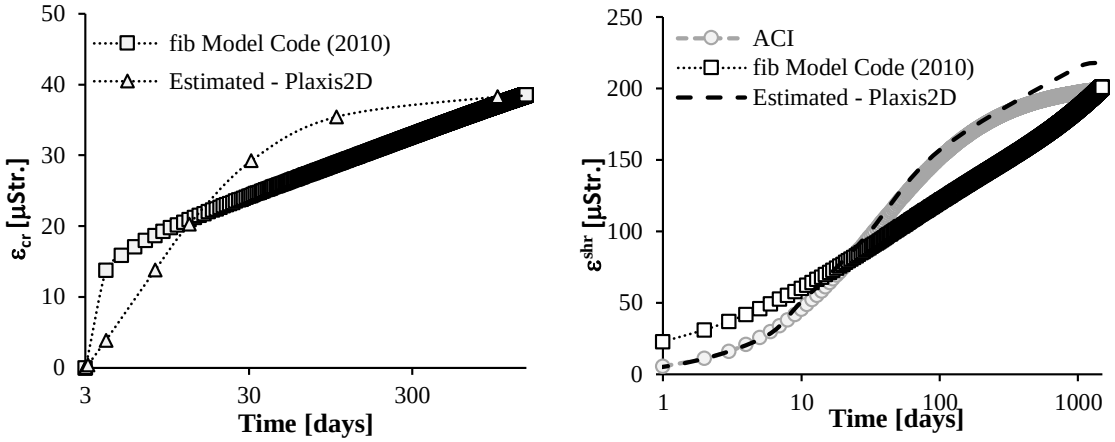

Figure 3-11. Creep and Shrinkage micro strains versus time for ring beams 1 and 7.

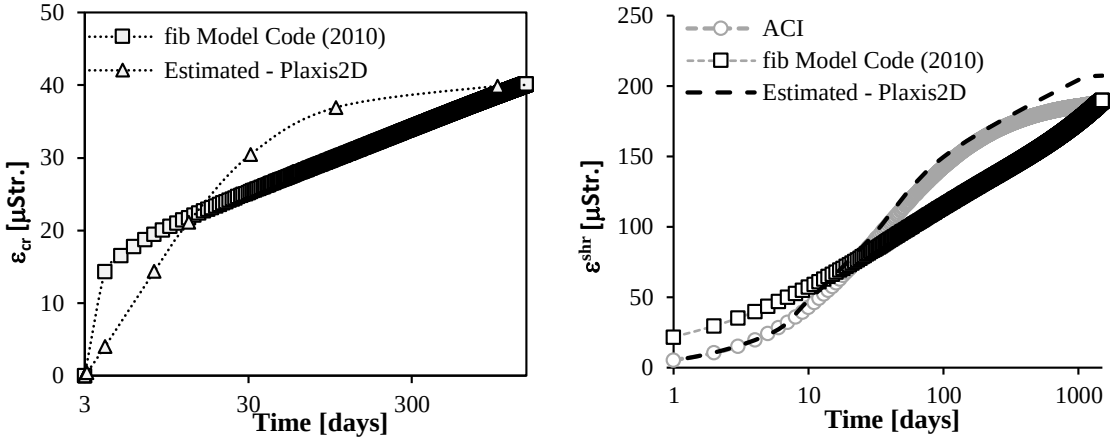

Figure 3-12. Creep and Shrinkage micro strains versus time for ring beams 2 and 6.

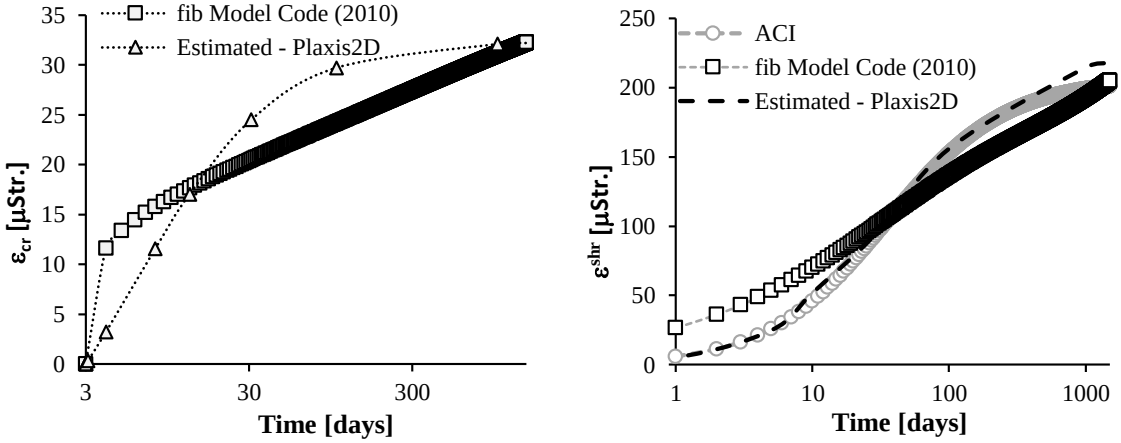

Figure 3-13. Creep and Shrinkage micro strains versus time for ring beams 3 to 5.

Table 3-5 shows steel sheet piles properties implemented in the numerical analysis, in which a linear elastic behavior is assumed. A plate element is used in software Plaxis for modeling the sheet piles. According to the geometric characteristics of the section PZ-27, area and first moment of inertia, the axial and flexural stiffness were calculated.

Table 3-5. Sheet pile properties.

Name	Sheet piles [Plate]	unit
EA1	28900000	kN/m
EA2	336000porous	kN/m
EI	50400	kN.m/m²
deq	0.1447	m

3.1.5 Construction Sequence

The sequence followed in the numerical analysis to simulate the cofferdam construction is summarized in **Table 3-6**. The table lists phase number, type of analysis, construction time intervals, and excavation elevations. The main construction activities were simulated by plastic calculations followed by consolidation phases to simulate construction times and allow the dissipation of excess porewater pressures. The cofferdam construction was simulated using 17 main calculations phases, which were divided into several sub-phases to closely followed field construction records, presented in Section 2.2.5. In summary, the simulation included the generation of the initial state of stresses followed by sheeting installation. The excavation process started at the +2.4 CCD elevation and was alternated with concrete ring beam installation stages. Excavation was suspended at -16.26 CCD elevation where the caisson foundations to support the rigid concrete core of the skyscraper were constructed. Although the construction of the 20 caissons was not explicitly included in the numerical analysis, their construction time was taken into account by a consolidation stage of about 190 days. **Figure 3-14** and **Figure 3-15** illustrate the construction sequence followed in the numerical analysis.

The surface surcharge, representing the load of construction equipment and the weight of the stock-pile material, was activated in phase 18, just before the construction of the third concrete ring beam.

Table 3-6. Construction sequence followed in the numerical simulation

ID			Phase	Initial Elevation [CCD]	Final Elevation [CCD]	ΔH [m]	Calculation type	Time interval [days]	Accumulated time [days]
1	Initial phase		0				K0 procedure	0	
2	Installation of sheeting		1				Plastic	0	0
3	L1 Excavation								
	3.1	Excavation from	2	2.4	0.219	2.181	Plastic	0	0
	3.2	Consolidation	3				Consolidation	7	7
4	RB1 Installation		4	0.219			Plastic	2.00	9
5	L2 Excavation								
	5.1	Excavation-2	5	0.219	-1.321	1.54	Plastic	0	9
	5.2	Consolidation	6				Consolidation	4	13
	5.3	Excavation-3	7	-1.321	-1.943	0.622	Plastic	0	13
	5.4	Consolidation	8				Consolidation	1	14
	5.5	Excavation-4	9	-1.943	-2.857	0.914	Plastic	0	14
	5.6	Consolidation	10				Consolidation	4	18
6	RB2 Installation		11	-2.857			Plastic	2	20
7	L3 Excavation								
	7.1	Excavation-2	12	-2.857	-4.401	1.544	Plastic	0	20
	7.2	Consolidation	13				Consolidation	4	24
	7.3	Excavation-3	14	-4.401	-5.267	0.866	Plastic	0	24
	7.4	Consolidation	15				Consolidation	2	26
	7.5	Excavation-4	16	-5.267	-6.333	1.066	Plastic	0	26
	7.6	Consolidation	17				Consolidation	5	31
	7.7	Unbraced	18				Consolidation	4	35
8	RB3 Installation		19	-6.333			Plastic	2	37
9	L4 Excavation								
	9.1	Excavation-2	20	-6.333	-7.993	1.66	Plastic	0	37
	9.2	Consolidation	21				Consolidation	4	41
	9.3	Excavation-3	22	-7.993	-8.567	0.574	Plastic	0	41
	9.4	Consolidation	23				Consolidation	2	43
	9.5	Excavation-4	24	-8.567	-9.633	1.066	Plastic	0	43
	9.6	Consolidation	25				Consolidation	6	49
10	RB4 Installation		26	-9.633			Plastic	0.1	49.1
11	L5 Excavation								
	11.1	Excavation-2	27	-9.633	-11.33	1.697	Plastic	0	49.1
	11.2	Consolidation	28				Consolidation	3	52.1
	11.3	Excavation-3	29	-11.33	-11.97	0.64	Plastic	0	52.1
	11.4	Consolidation	30				Consolidation	1	53.1
	11.5	Excavation-4	31	-11.97	-13.03	1.06	Plastic	0	53.1
	11.6	Consolidation	32				Consolidation	5	58.1
12	RB5 Installation		33	-13.03			Plastic	0.1	58.2
13	L6 Excavation								
	13.1	Excavation-2	34	-13.03	-14.5	1.47	Plastic	0	58.2
	13.2	Consolidation	35				Consolidation	7.9	66.1
	13.3	Excavation-3	36	-14.5	-15.34	0.84	Plastic	0	66.1
	13.4	Consolidation	37				Consolidation	3	69.1
	13.5	Excavation-4	38	-15.34	-16.26	0.92	Plastic	0	69.1
	13.6	Consolidation	39				Consolidation	7	76.1
14	RB6 Installation		40	-16.26			Plastic	0	76.1
15	Caissons Installation		41				Consolidation	190.9	267
16	L7 Excavation								
	16.1	Excavation-1	42	-16.26	-17.86	1.6	Plastic	0	267
	16.2	Consolidation	43				Consolidation	1	268
	16.3	Excavation-2	44	-17.86	-19.58	1.72	Plastic	0	268
	16.4	Consolidation	45				Consolidation	1.75	269.75
17	RB7 Installation		46	-19.58			Plastic	0.25	270

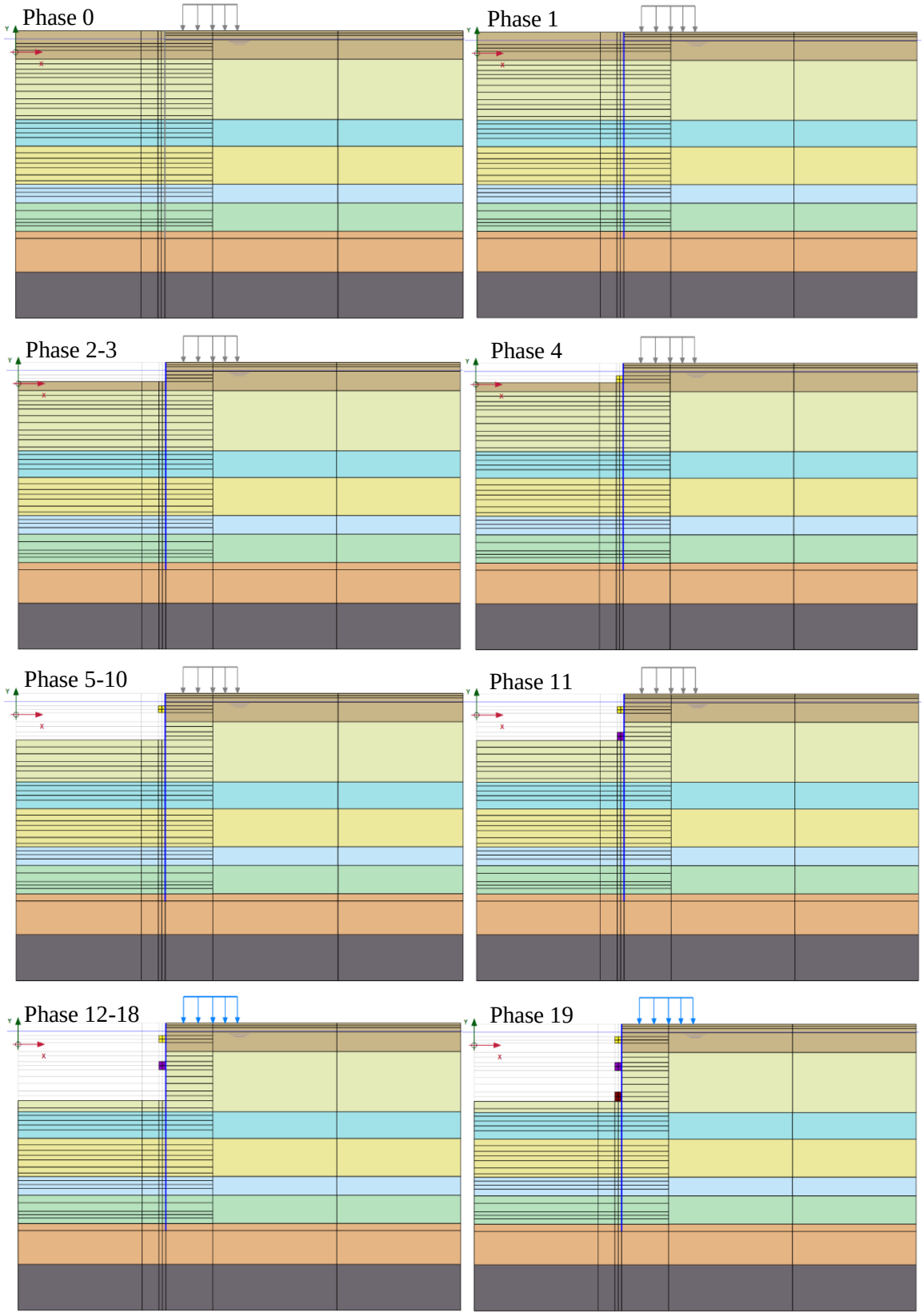

Figure 3-14. Construction sequence considered in numerical analysis, phases 0 to 19.

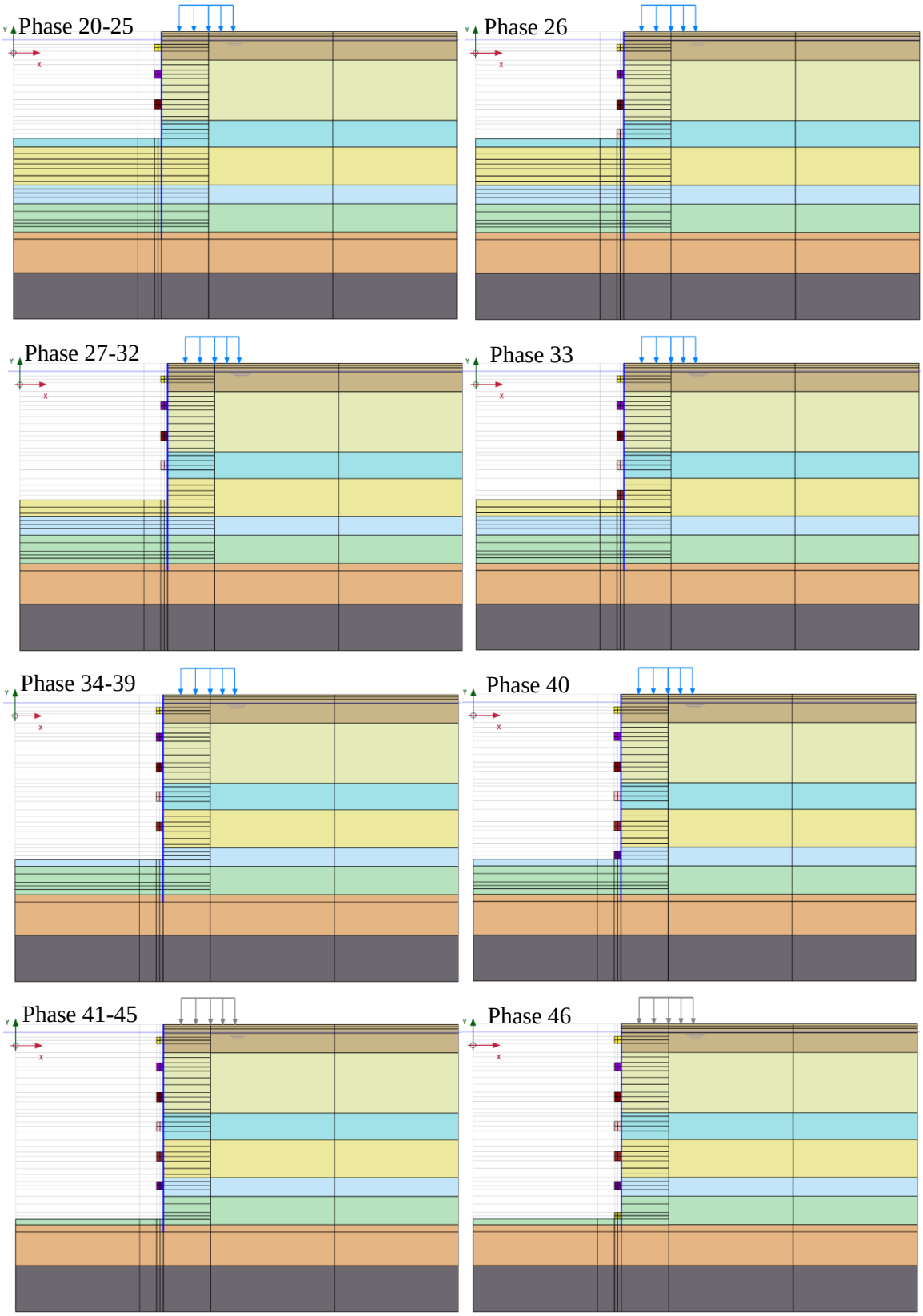

Figure 3-15. Construction sequence considered in numerical analysis, phases 20 to 46.

3.1.6 Modeling Groundwater Conditions

Steady-state pore pressures were calculated using the groundwater flow calculation in Plaxis. It is based on the definition of boundary hydraulics conditions and the coefficients of permeability assigned to the different soil layers. The software interpolates pore pressures between soil clusters of larger hydraulic heads and those where a smaller hydraulic head was defined. Additional information about groundwater flow model that describes hydraulic behavior of materials is presented by (Galavi 2010) and (Brinkgreve et al. 2011).

Based on the construction and photographic records, pumping wells were used during the cofferdam construction keeping the excavation bottom free of water (See **Figure 3-16**). Typical measurements of the ground water table level taken within the superficial urban fill material roughly coincide with the river or lake water levels (i.e., about 0 to 1.5m CCD). Therefore, the groundwater conditions in the Plaxis simulations considered a global water table level at +1.50 CCD as shown in Figure 3-18(a). At each plastic excavation phase, the hydraulic head at the bottom of the excavation was modified to the corresponding magnitude according to its elevation, (see **Figure 3-17** (b) for the particular case of excavation advanced to Elevation -9.633 CCD). Even on the plastic phase, the interpolation process is executed to determine the new steady-state condition and the excess pore water pressure. Finally, a consolidation phase is used to estimate the development and dissipation of excess porewater pressures.

Figure 3-16. Pumping wells in the excavation during cofferdam construction.

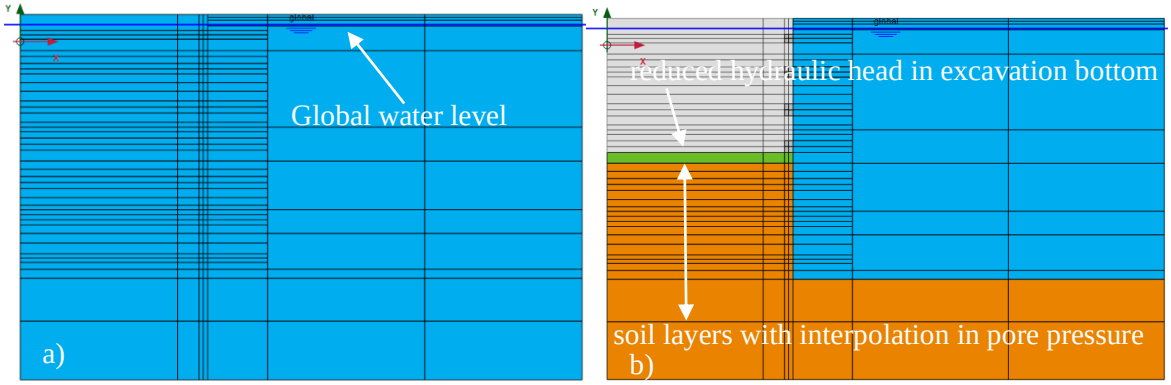

Figure 3-17. Groundwater Conditions a) Steady-state initial condition and b) interpolation in groundwater flow at calculation phase 24.

Figure 1 shows the active pore pressure after the interpolation and consolidation phases

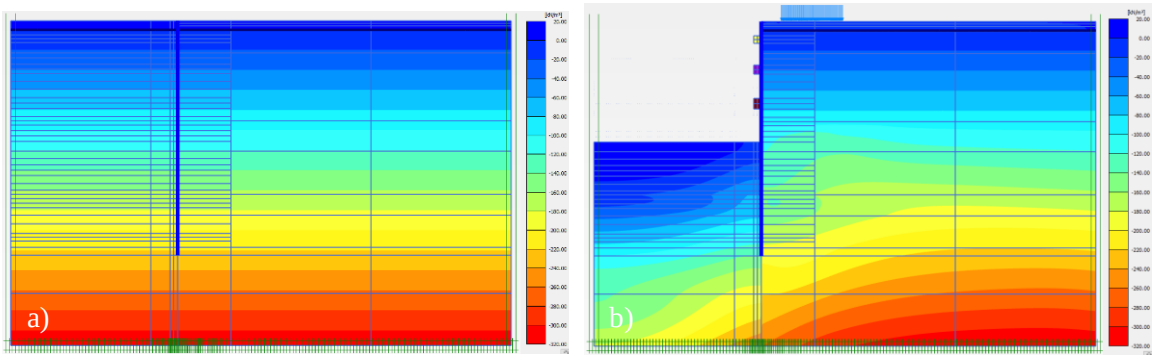

Figure 3-18. Groundwater Conditions a) Active pore pressure initial condition and b) Active pore pressure after the interpolation and consolidation phases at calculation phase 24.

As mentioned in Section 2.2.3 due to the construction of the tunnel and the pumping system, a decrease in the total hydraulic head (to -14.5 m CCD) at the top of the rock formation has been generated. The effect of reduction in porewater pressure is not considered in the base model as neither are fully coupled flow-deformation analyses. The analysis of these effects is out of the scope of this research. It is important to mention that the main goal in this work is to study the time dependent effects of the concrete ring beams bracing an urban cofferdam. The inclusion of the effects related to time dependence in hydraulic conditions, as well as concrete time-dependency and the hypoplasticity model for clays would have considerably increased the computational cost of the Plaxis simulations. However, the impact on the obtained results of neglecting these effects is discussed in Section 3.2.

3.2 Results of the Base Model

Figure 3-19 compares the computed horizontal displacements with field measurements of inclinometer I-1 at various stages of the cofferdam construction. The figure shows elevations in terms of the Chicago City Datum (CCD) and presents the stratigraphic profile, concrete ring beam positions and excavation sequence. According to field records, the inclinometer I-1 was installed on 29/12/2007, 59 days after the cofferdam construction began. Therefore, the computed horizontal displacements included in the figure are incremental movements corrected based on the construction stages no capture by the inclinometer.

It is important to clarify that **Figure 3-19** shows the inclinometer readings from +0.571 to -23.813 CCD elevations, for a total length of 24.813 m indicating that the inclinometer was embedded in the limestone bedrock. The computed results from the base model are presented from the ground surface (+2.4 CCD elevation) to the bottom of the sheeting (-21 CCD elevation).

Although the observed field performance has records until cofferdam construction end, information about concrete compressive strength tests of ring beams 6 and 7 is not available in this investigation. Therefore, the comparative analysis is limited to excavation dates before placing concrete of the sixth ring beam. In effect, field measurements are available from the dates corresponding to the construction of the second ring beam, placed at -2.857 CCD elevation, to the end of excavation 6 at -16.26 CCD elevation. Due to this, **Figure 3-19** shows incremental lateral movements for excavation stages termed herein Ex-3, -4, -5, and -6 which correspond to -6.666, -9.633, -13.03, and -16.26 CCD elevations, respectively.

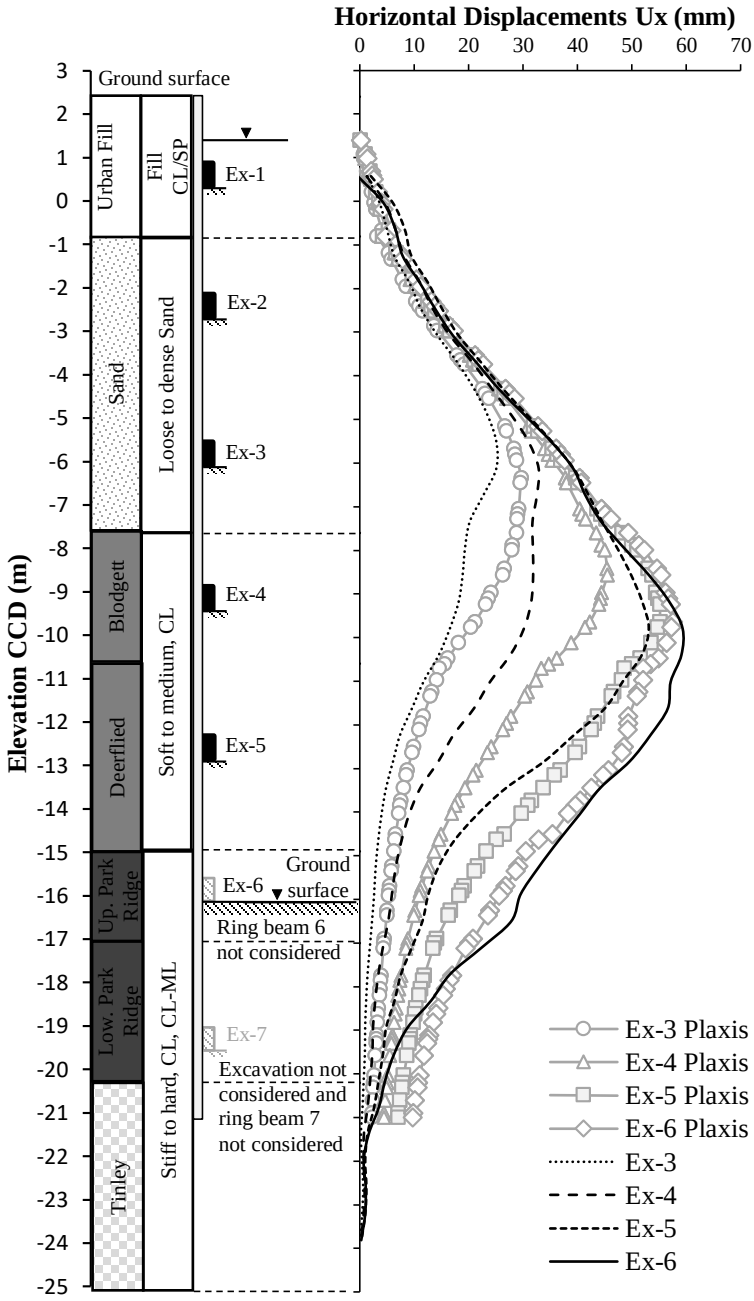

Figure 3-19. Computed versus measured horizontal displacements at excavation elevation of -6.666, -9.633, -13.03 and -16.26 CCD.

Note on **Figure 3-19** that the computed and measured horizontal displacements present a reasonably match for the different construction stages considered herein. The numerical model is capable of predicting the shape of the lateral deformations within the different soil layers and the location of the maximum deformation.

Figure 3-20 shows the horizontal displacements versus construction time extracted from the I-1 inclinometer readings at the elevations of the concrete ring beams. Also included in the figures are the Plaxis computed responses. In general, a good agreement between the calculated and measured responses are observed. Note also that for ring beam elevations 3, 4 and 5 around construction days 69-70 a significant increase in the displacement rate, evidenced by the steep slope of the curve, takes place. This sudden deformation increment is associated with the surface surcharge that represents the weight of an excavated material stock-pile and construction equipment. As presented in Section 3.1.3 these surcharge elements were evidenced in the photographic record of the project around days 69 corresponding to the construction of the third concrete ring beam.

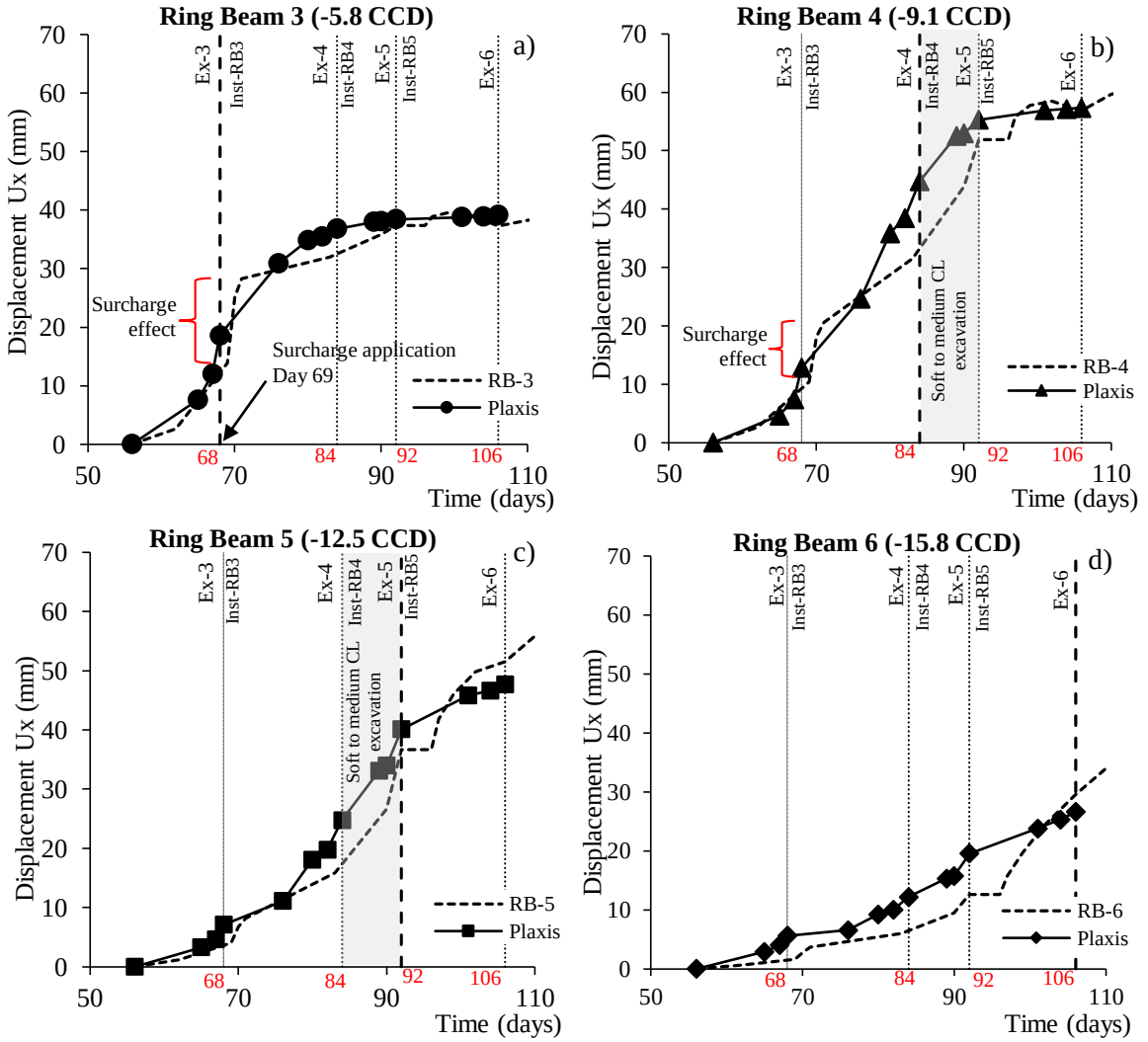

Figure 3-20. Computed and observed horizontal displacements during construction at the concrete ring beam elevations: a) Ring beam 3; b) Ring beam 4; c) Ring beam 5; and d) Ring Beam 6.

Note also on **Figure 3-20** (b) and (c) that another rapid increment in the displacement rate takes place between construction days 84 and 92. This time interval corresponds to the excavation through soft clays found between -7.60 and -15 CCD elevations.

Figure 3-21 shows horizontal displacement contours generated in Plaxis 2D for excavation stages corresponding to the elevations of concrete ring beams 1 to 7. This figure, along with the pore water pressure response computed near the sheeting at the ring beam elevations (see Figure 3-22), the hardening soil model plastic points (see Figure 3-23), the mobilized relative shear strength (see Figure 3-24), the normalized length of the intergranular strain tensor in the hypoplasticity clay model (see Figure 3-25) and the mobilized friction angle (see Figure 3-26), allow to identify the main failure and strain concentration zones and the deformation mechanisms generated during the cofferdam construction.

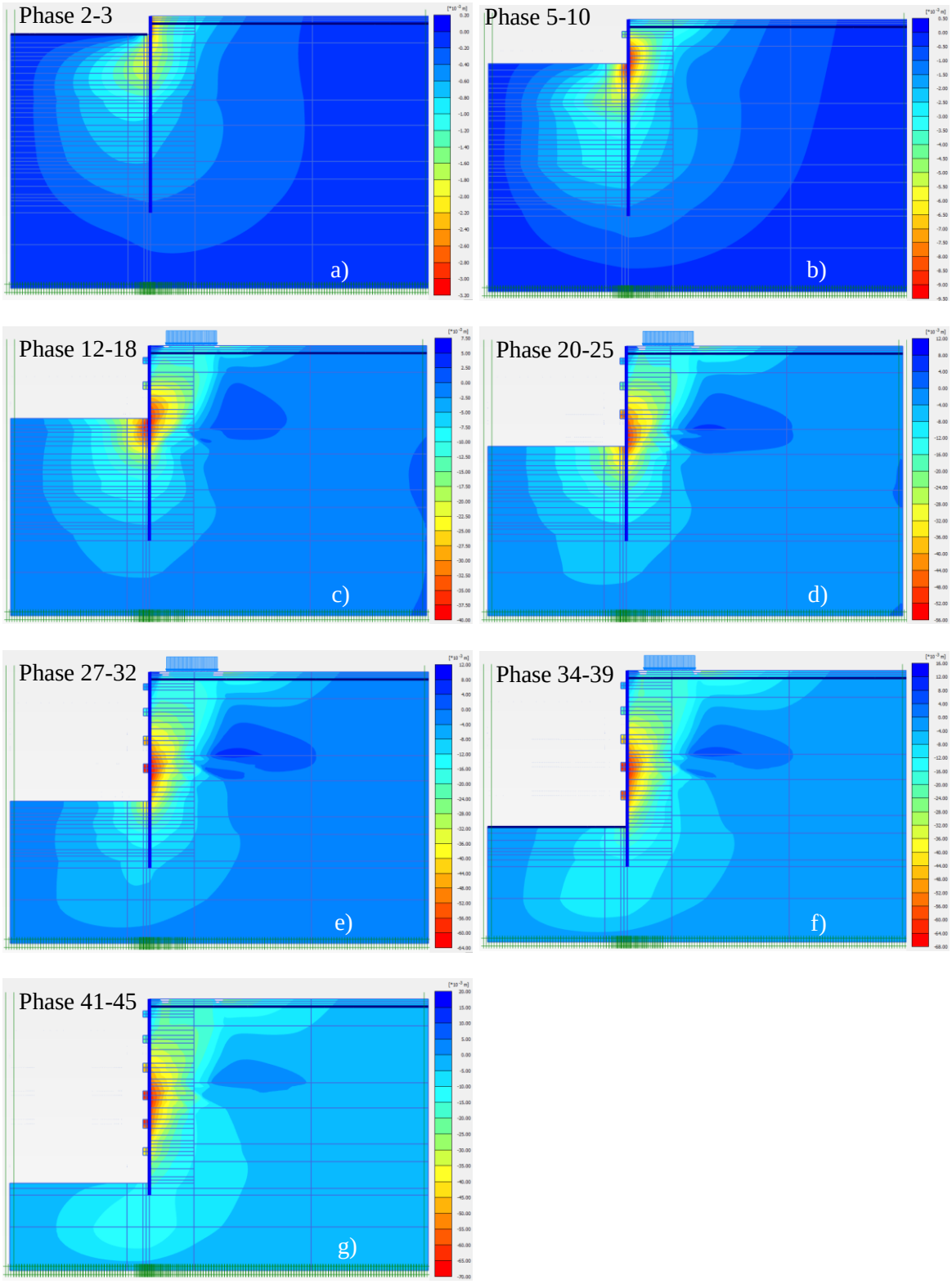

Figure 3-21. Computed horizontal displacement contours Ux: a) excavation 1 b) excavation 2 c) excavation 3 d) excavation 4 e) excavation 5 f) excavation 6 g) excavation 7.

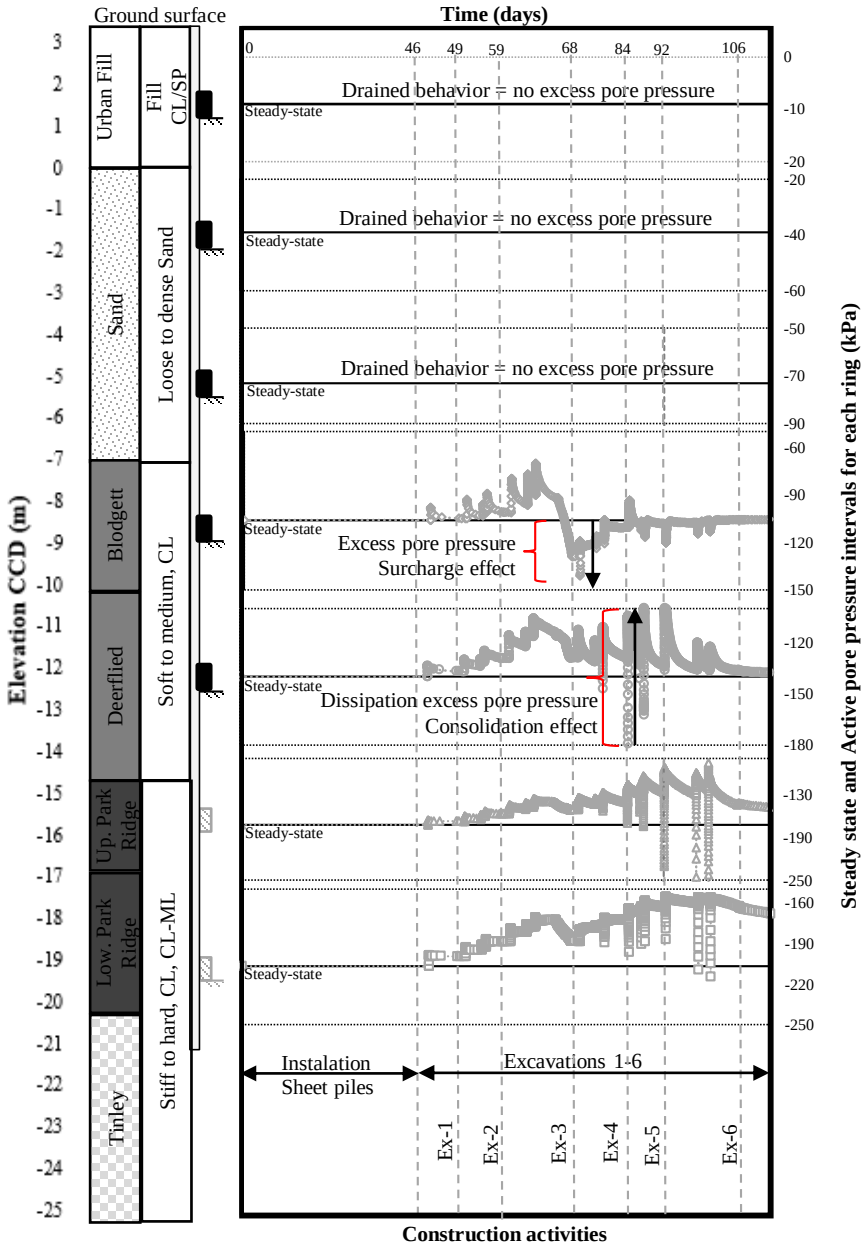

Figure 3-22. Variation with time of computed steady-state and active pore pressures.

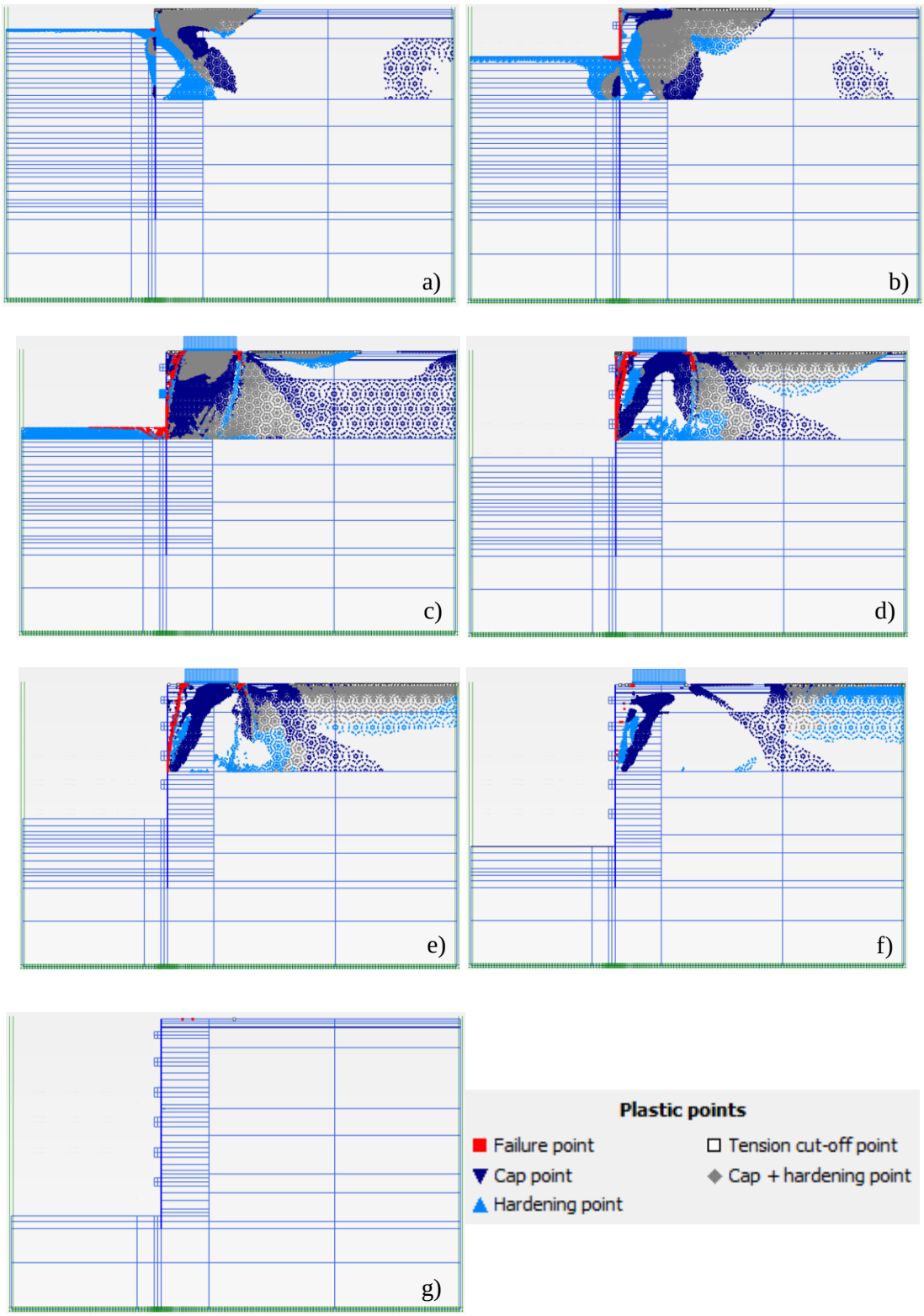

Figure 3-23. Hardening soil model plastic points: a) excavation 1 b) excavation 2 c) excavation 3 d) excavation 4 e) excavation 5 f) excavation 6 g) excavation 7.

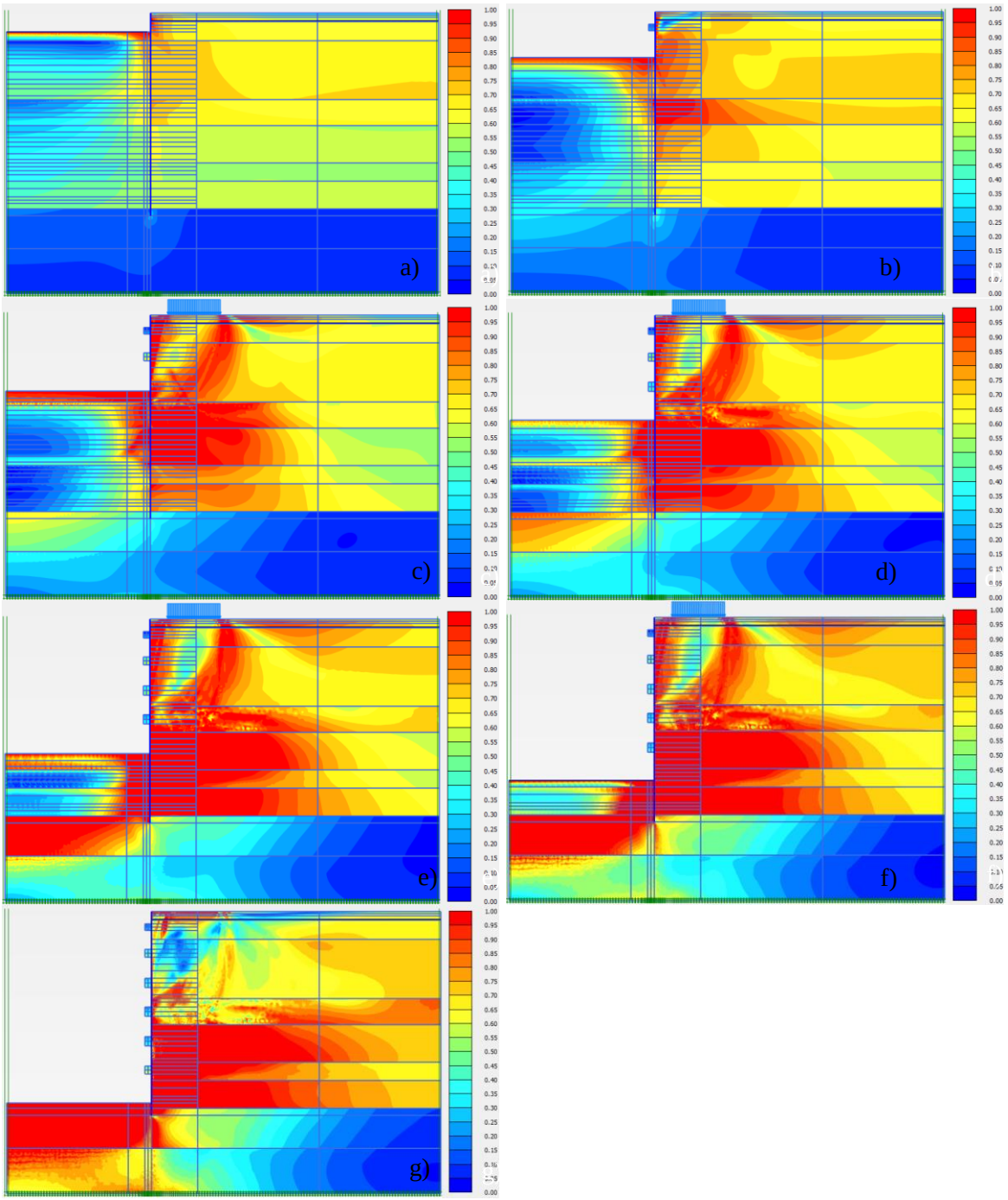

Figure 3-24. Mobilized relative shear strength contours: a) excavation 1 b) excavation 2 c) excavation 3 d) excavation 4 e) excavation 5 f) excavation 6 g) excavation 7.

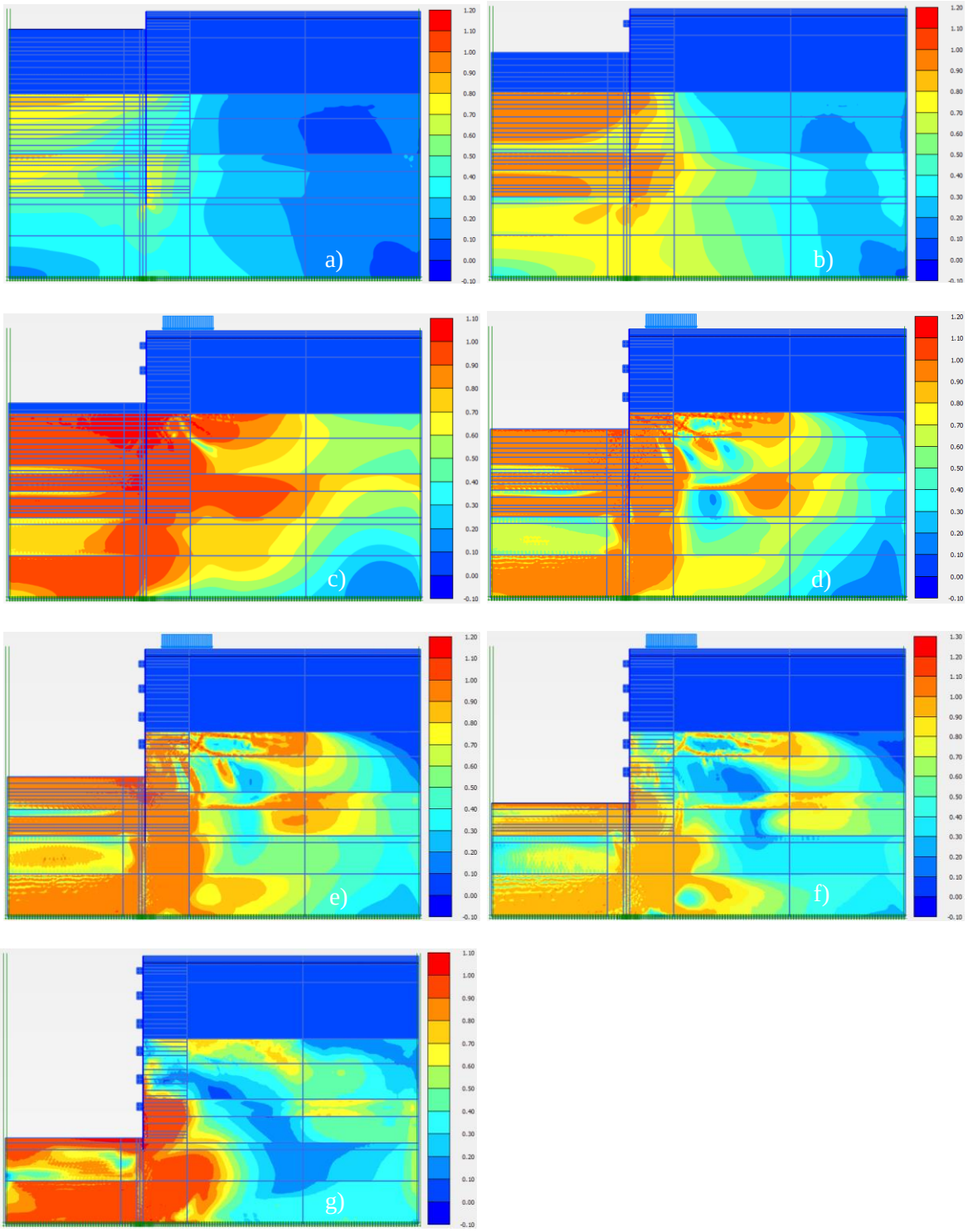

Figure 3-25. Contours of the normalized length of the intergranular strain tensor of the hypoplasticity clay model: a) excavation 1 b) excavation 2 c) excavation 3 d) excavation 4 e) excavation 5 f) excavation 6 g) excavation 7.

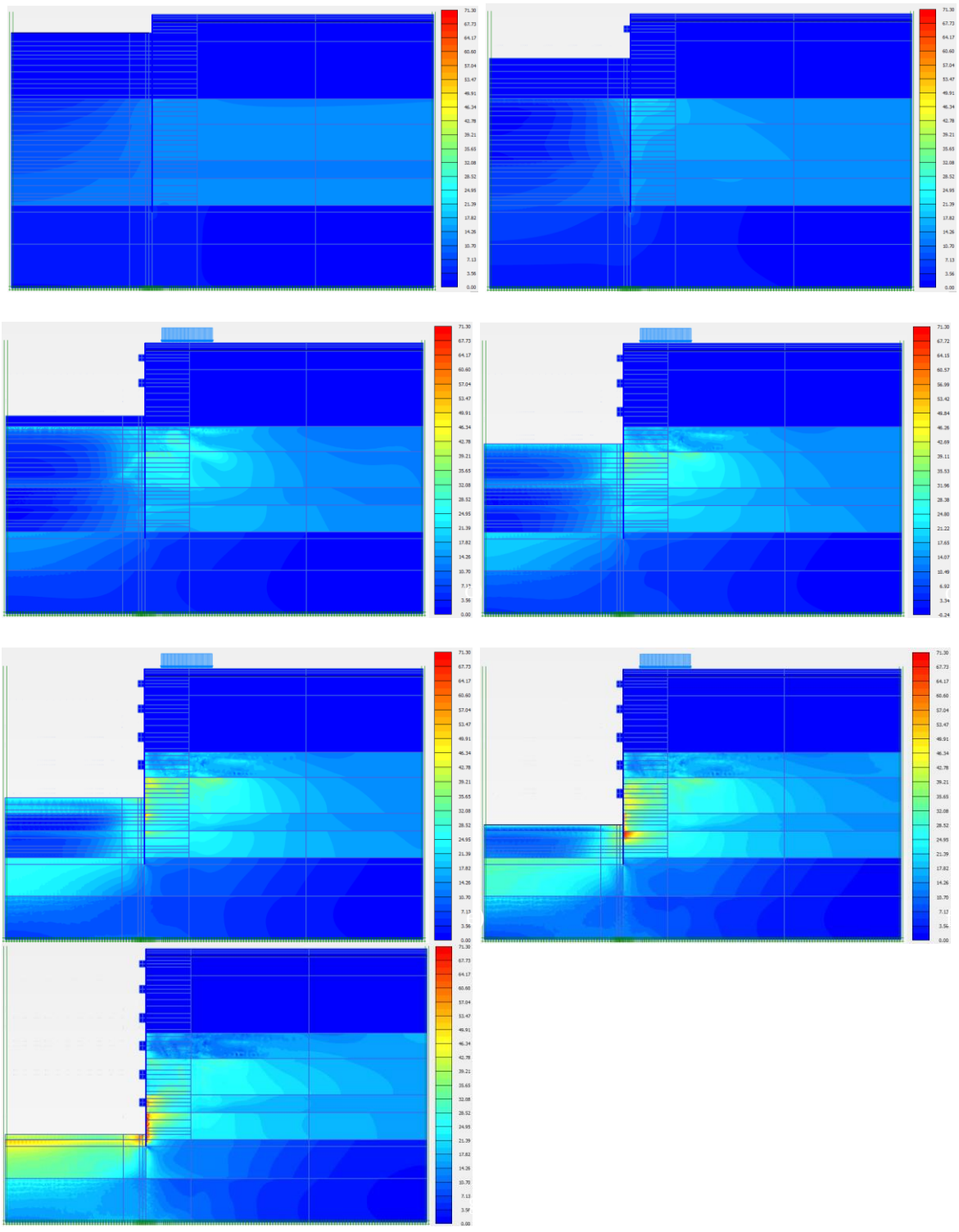

Figure 3-26. Mobilized friction angle contours: a) excavation 1; b) excavation 2; c) excavation 3; d) excavation 4; e) excavation 5; f) excavation 6; and g) excavation 7.

The results presented in the above figures are discussed or grouped based on the main soil layers presented at the site. The upper layers (from +0.571 CCD to -7.6 CCD), consisting of filling material and loose to dense sands show a very good adjustment of the computed lateral displacements with respect to the performance data (**Figure 3-19**). Note on **Figure 3-21**, that the horizontal ground deformations, up to phase 18, were mainly developed on the loose to dense sand layers. As excavation proceeded, ground deformations concentrated on the soft to medium clays presenting a maximum value of about 58 mm at the end of the excavation (i.e., phase 45). The deformations at the bottom of the model, specifically between elevations of -15 m CCD and -25 m CCD, are restrained by the Park Ridge stratum of stiff to hard clays. The main function of these hard soils was to provide embedment and passive resistance to the sheeting. Note on Figure 3-19 that the hypoplastic clay soil model did not capture accurately the response of the embedded portion of the cofferdam. A sheeting toe movement of approximately 7.5 mm was computed at the end of excavation 6. These discrepancies are attributed to the limitation of the hypoplastic clay soil model to represent the response of hard or transition geomaterials (Mašín 2005)(Mašín 2014) as the one found at the bottom of the cofferdam.

Two main soil failure mechanisms during the cofferdam construction are identified. Initially, an approximately planar failure surface in the upper granular layers, with an inclination of 70 degrees with respect to the horizontal line, can be observed from the Hardening Soil model plastic points and relative shear stresses presented in **Figure 3-23**(c and d) and **Figure 3-24** (c and d), respectively. Note in the figures that the lateral deconfinement of the granular layers and the associated excavation-induced deformations, around calculation phase 20, were large enough to generate a failure state in the granular layers similar to the theoretical Rankine Active state, which predicts a failure surface at about 65 degrees. These materials were modeled assuming a drained behavior and consequently no excess pore water pressures are generated. The second failure mechanism is formed as excavation proceeds to the soft to medium clays. This layer has a thickness of about 7.40 m and is found underlying the granular materials. As shown in **Figure 3-22**, this clay layer developed an undrained behavior and was subjected to a downward flow, which imposed a reduction in the hydraulic head. Excess pore water pressures in this layer peak during construction times corresponding to excavation to ring beam 3 elevation and are associated with two events. First is the lateral unloading of the clays behind the sheeting as a result of the cofferdam excavation. Second is the application of the surcharge load in phase 18, just before the construction of the third concrete ring beam, which generated positive excess pore water pressures and in turn considerable reduction

of the undrained shear strength of the clay. This can be observed in **Figure 3-24** where the mobilized relative shear strength is presented incrementally.

The model used to calculate the clays stress-strain response implements two main parameters for a clear interpretation, called Normalized Length of the Intergranular Strain Tensor and Mobilized Friction Angle. The first one varies from 0, indicating that the soil is within the elastic range, up to 1 where soil behavior is governed by the basic model of hypoplasticity (Mašín 2011). The normalized length of the Intergranular Strain Tensor (see **Figure 3-25**) and the mobilized friction angle (see **Figure 3-26**) show similar results to the mobilized relative shear strength. Note that around times corresponding to excavation 3 and ring beam 3 construction, localized shear zones in the soft clays were generated, mainly at the interface between the Blodgett and the Deerfield layers. As excavation advances to the deeper hard material, (i.e., around excavation 5) localized shear zones are identified at the interface of the sheeting and the Park Ridge stratum.

Table 3-7 summarizes the evaluation of concrete strength demand/capacity indices, σ_{zzi}/f'_c, as a function of the total stresses acting on the concrete ring beams and their compressive strength for excavations 2 to 6. The total stresses on each ring beam were estimated from the numerical model as the cartesian total stresses σ_{zz} in the z-direction. The indices presented in **Table 3-7** show that concrete ring beams 2 and 3 were the most demanded in terms of resistance. Ring 2 showed a maximum index of 0.37 at the end of excavation 3. This evaluation allowed validation of the restriction stipulated by (fib Model Code, 2010) which only allows to apply the formulations to study the effects of aging, creep and shrinkage for concrete sections subjected to stresses that do not exceed $0.40f'_c$.

Table 3-8 presents the evolution of stiffness, as represented by the elastic young modulus, in the concrete ring beams for each stage of the excavation. It is assumed that stresses are induced on the ring beams once excavation advances under the ring beam location. Note that at the time of the first induced-load on the ring beams, only 77 to 85% of the design stiffness was developed. Early applied load on the concrete rings, without these having reached the design rigidity, leads to additional lateral displacements. Similar to resistance, the concrete non-linear behavior is also significantly affected by aging and time-dependent effects.

Table 3-7. Concrete ring beams demand/capacity index.

Ring Beam #	Cartesian total stresses σ_{zzi} [MPa] Concrete maturity [%] [a] $I_{d/c}$ [b]	Ex-2 Construction day 59	Ex-3 Construction day 68	Ex-4 Construction day 84	Ex-5 Construction day 92	Ex-6 Construction day 106
1 Construction days 49-53	σ_{zz} [MPa]	3.00	3.09	2.96	3.09	3.11
	Maturity [%]	64	79	94	97	104
	$I_{d/c}$	0.09	0.07	0.06	0.06	0.05
2 Construction days 59-61	σ_{zz} [MPa]		12.35	10.75	10.13	9.88
	Maturity [%]		62	88	93.	101
	$I_{d/c}$		0.37	0.23	0.20	0.18
3 Construction days 68-76	σ_{zz} [MPa]			7.26	8.87	8.21
	Maturity [%]			79	88	94
	$I_{d/c}$			0.14	0.15	0.13
4 Construction days 84-86	σ_{zz} [MPa]				5.29	5.69
	Maturity [%]				70	84
	$I_{d/c}$				0.12	0.11
5 Construction days 92-95	σ_{zz} [MPa]					5.99
	Maturity [%]					66
	$I_{d/c}$					0.14

[a] Concrete maturity in terms of f_{c1}/f_{c28}.

[b] $I_{d/c}$ is the demand/capacity index

Table 3-8. Development of elastic modulus with time.

Ring Beam #	Development of elastic modulus with time	Ex-2 Construction day 59	Ex-3 Construction day 68	Ex-4 Construction day 84	Ex-5 Construction day 92	Ex-6 Construction day 106
1 Construction day 49-53	Maturity [%] [a]	77	86	96	96	97
2 Construction days 59-61	Maturity [%] [a]		77	90	94	96
3 Construction days 68-76	Maturity [%] [a]			85	91	94
4 Construction days 84-86	Maturity [%] [a]				81	89
5 Construction days 92-95	Maturity [%] [a]					78

[a] Concrete maturity in terms of E_1/E_{28}.

4. PARAMETRIC ANALYSIS

The previous chapter described the developed of a numerical model was built employing available advanced concrete and soil constitutive models to reproduce the non-linear soil response and its interaction with the bracing support system of an urban cofferdam. The Hardening Soil (Schanz et al. 1999) and Hypoplasticity clay (Mašín 2005) (Mašín 2012)(Mašín 2014) constitutive soil models were used to simulate the response of sands and clays, respectively. The shotcrete constitutive model (Schädlich and Schweiger 2014b) was implemented to simulate the elasto-plastic response of the concrete ring beams and evaluate time-dependent effects such as shrinkage, creep and aging. Using the numerical model mentioned above, a parametric analysis was conducted to isolate the time-dependent effects of the concrete and evaluate their individual impact on the cofferdam horizontal displacements. For this purpose, four numerical simulations of the cofferdam construction, based on the base model presented in Chapter 3, were conducted. The Shotcrete Model main parameters (E_1/E_{28}, $f_{c,1}/f_{c,28}$, φ^{cr} and ε^{shr}) were selectively deactivated, depending on what effect was going to be studied. As explained in Section 2.4.1, these Shotcrete parameters control additional deformations due to creep, shrinkage and aging. **Table 4-1** summarizes the numerical analysis used in the parametric study.

Table 4-1. Summary of parametric analysis.

Analysis type	Concrete time-dependent effect		
	Aging	**Creep**	**Shrinkage**
Ex-6 without any effects	No	No	No
Ex-6 + shrinkage	No	No	Yes
Ex-6 + creep	No	Yes	No
Ex-6 + aging	Yes	No	No

The curve of horizontal displacements obtained in the base model at the time of excavation 6 was chosen as reference because at this point the maximum deformation was obtained in the cofferdam and can be compared with the performance observed in the field; as explained in section 3.2

information about concrete compressive strength tests of ring beams 6 and 7 is not available in this investigation.

4.1 Input Parameters

Time-dependent effects in the concrete that forms the bracing ring beams were neglected by changing key parameters in the Shotcrete constitutive model used to simulate their behavior during the cofferdam construction. To neglect shrinkage effects and preclude deformations due to volume loss of the concrete cementing paste with time, the final shrinkage strain, ε^{shr}, was assumed equal to zero. Deformations arising from sustained loads over time were avoided by assigning a zero value to the ratio of creep to elastic strains, φ^{cr}. Aging in the Shotcrete model was neglected and its resulting time effects in strength and stiffness eliminated by assigning a unitary value to the relations E_1/E_{28} and $f_{c,1}/f_{c,28}$. The other shotcrete and soil constitutive model parameters were not modified. Table **Table 4-2** lists the parameters used to neglect time-dependent effects in the numerical model while Tables **Table 4-3**, **Table 4-4**, and **Table 4-5** list the input parameters used to isolate the effects of shrinkage, creep and aging, respectively.

Table 4-2. Shotcrete parameters neglecting all concrete time-dependent effects.

Name	RB1	RB2	RB3	RB4	RB5	RB6	RB7	unit
E_{28}	38060000	37610000	40180000	38278941	39089390	37610000	38060000	kN/m²
$f_{c,28}$	55490	53530	65280	56437	60098	53530	55490	kN/m²
E_1/E_{28}	1	1	1	1	1	1	1	-
$f_{c,1}/f_{c,28}$	1	1	1	1	1	1	1	-
φ^{cr}	0	0	0	0	0	0	0	-
$\varepsilon_{\infty}^{shr}$	0	0	0	0	0	0	0	-
t_{hydr}	51	54	54	59	62	56	22	day

Table 4-3. Shotcrete parameters considering shrinkage effects.

Name	RB1	RB2	RB3	RB4	RB5	RB6	RB7	unit
E_{28}	38060000	37610000	40180000	38278941	39089390	37610000	38060000	kN/m²
$f_{c,28}$	55490	53530	65280	56437	60098	53530	55490	kN/m²
E_1/E_{28}	1	1	1	1	1	1	1	-
$f_{c,1}/f_{c,28}$	1	1	1	1	1	1	1	-
φ^{cr}	0	0	0	0	0	0	0	-
$\varepsilon_{\infty}^{shr}$	-0.000203	-0.000192	-0.000205	-0.000193	-0.000198	-0.000195	-0.000210	-
t_{hydr}	51	54	54	59	62	56	22	day

Table 4-4. Shotcrete parameters considering creep effects.

Name	RB1	RB2	RB3	RB4	RB5	RB6	RB7	unit
E_{28}	38060000	37610000	40180000	38278941	39089390	37610000	38060000	kN/m²
$f_{c,28}$	55490	53530	65280	56437	60098	53530	55490	kN/m²
E_1/E_{28}	1	1	1	1	1	1	1	-
$f_{c,1}/f_{c,28}$	1	1	1	1	1	1	1	-
φ^{cr}	1.380	1.420	1.220	1.390	1.320	1.460	1.490	-
$\varepsilon_{\infty}^{shr}$	0	0	0	0	0	0	0	-
t_{hydr}	51	54	54	59	62	56	22	day

Table 4-5. Shotcrete parameters considering aging effects.

Name	RB1	RB2	RB3	RB4	RB5	RB6	RB7	unit
E_{28}	38060000	37610000	40180000	38278941	39089390	37610000	38060000	kN/m²
$f_{c,28}$	55490	53530	65280	56437	60098	53530	55490	kN/m²
E_1/E_{28}	0.3831	0.3828	0.3821	0.4512	0.3319	0.4001	0.6205	-
$f_{c,1}/f_{c,28}$	0.1371	0.1370	0.1368	0.1915	0.1038	0.1522	0.3791	-
φ^{cr}	0	0	0	0	0	0	0	-
$\varepsilon_{\infty}^{shr}$	0	0	0	0	0	0	0	-
t_{hydr}	51	54	54	59	62	56	22	day

4.2 Results of the Parametric Analysis

The results of the parametric analysis are presented in **Figure 4-1** in terms of computed horizontal displacements versus elevation. The figure shows the obtained results for the numerical model neglecting all time-dependent effects and those where the effects of shrinkage, creep and aging, were isolated or uncoupled. Also included in the figure is the horizontal displacement profile obtained from the base model which includes all coupled effects of temperature, soil consolidation, and concrete time-dependency. **Table 4-6Table 4-6.** Results for the coupled parametric analysis. and **Table 4-7** summarize the obtained results in terms of the maximum horizontal displacement and percentage with respect to the base model maximum displacement, for coupled and uncoupled models, respectively.

Based on the parametric study results for this case history, it was found that concrete time-dependent effects represent about 25 % of the maximum horizontal displacements in urban cofferdams braced with reinforced concrete ring beams. Note that aging effects are the most important concrete time-

dependent component. Aging induced-deformations for the considered case represent about 15% of the total horizontal displacements calculated from the base model. Creep and shrinkage effects contribute around 6 and 3 %, respectively.

It is important to mention that the above concrete time-dependent effects occur as a fully coupled phenomenon with soil consolidation and the incrementally non-linear response of the soil. It was found that an isolated or uncoupled analysis would slightly underestimate the deformations. It is evidenced when comparing the results from the numerical model considering all coupled effects with the uncoupled models. The slight difference (i.e., 1.2%) in both approaches is attributed to the non-linear response of the soil.

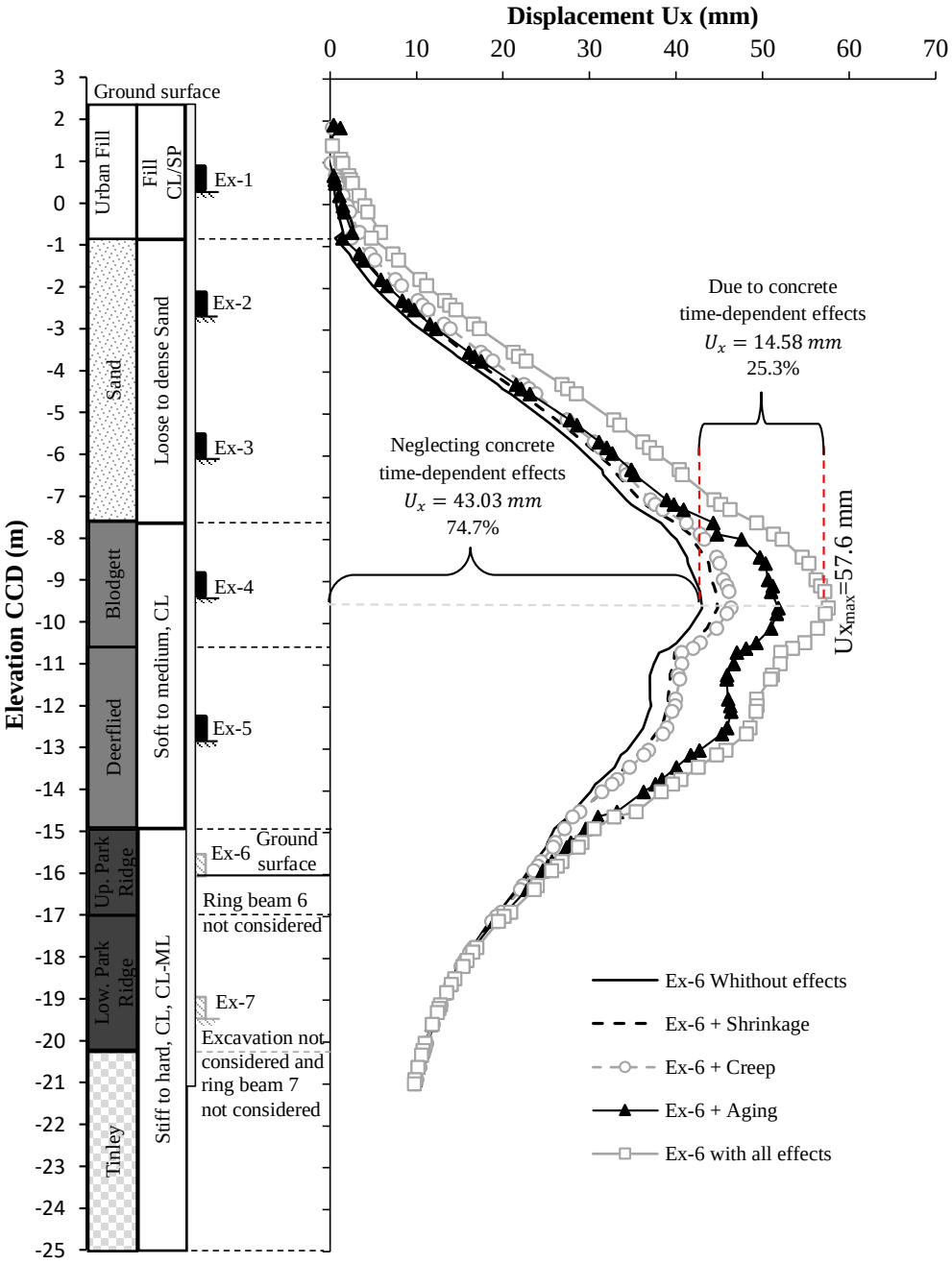

Figure 4-1. Results of the parametric study: horizontal displacement at Ex-6 computed using Plaxis 2D uncoupled and coupled effects.

Table 4-6. Results for the coupled parametric analysis.

Coupled effects Parametric model	Ux **[mm]**	%/Uxmax
Ex-6 with all effects (base model) - Ux max	57.61	
Ex-6 without any effects	43.03	74.7
Uxe due to concrete time dependent effects	14.58	**25.3**
	Σ	100.00

Table 4-7. Results for the uncoupled parametric analysis.

Decoupled effects parametric model	Ux+Uxe max **[mm]**	Uxe **[%]**
Ex-6 + shrinkage	43.03 + 1.77	3.1
Ex-6 + creep	43.03 + 3.35	5.8
Ex-6 + aging	43.03 + 8.76	15.2
	Σ	**24.1**

(Arboleda-monsalve et al. 2015) reported that concrete time-dependent effects represent approximately 30% of the maximum displacements measured in the top-down excavation of the OMPW project, in which the shrinkage effect dominated the response. The OMPW project used a support system braced continuously with concrete floor slabs, which have large surfaces exposed to environmental conditions. Then, it was expected that variations of relative humidity and temperature would affect the concrete material response. Although the top-down system reported by (Arboleda-monsalve et al. 2015) greatly differs from the bottom-up urban cofferdam braced with concrete ring beams studied in the present work, the total contribution of concrete time-dependent effects to the horizontal displacements in percentage is very similar (about 30 and 25 %, respectively). As opposed to top-down excavation systems, shrinkage has no significant impact on the performance of cofferdam braced with reinforced concrete ring beams. It is because the surface exposed during the concrete curing process of a ring beam is much smaller than the exposed surface of a floor slab.

The significance of the time-dependent effects found in this investigation for reinforced concrete ring beams used as bracing support system in urban cofferdams, lead to conclude that these effects should be included, from the beginning, in the designs of the support systems. It allows to foresee additional deformations in the soil and consequently avoid damage to structures or perimeter service lines.

The inclusion of these effects in the designs must be complemented with historical records of temperature and relative humidity of the expected construction seasons so that the most adverse conditions to which the cofferdam will be subjected to, can be evaluated. This is particularly the case of cofferdams located in mid-latitude and polar regions where changes in climatic seasons are so marked, as is the case of Chicago city where the research site presented in this thesis is located.

5. CONCLUSIONS AND RECOMMENDATIONS

5.1 Conclusions

This research work presented a parametric study to evaluate time-dependent effects in an urban cofferdam braced with reinforced concrete ring beams. This is the first time where a fully couple numerical approach, considering aging, creep and shrinkage effects in the concrete along with advanced constitutive soil models to adequately represent consolidation and non-linear soil behavior, is presented. The parametric study is based on a numerical model calibrated and validated against field performance data collected during the construction of an urban cofferdam braced with seven reinforced concrete ring beams.

Based on the evaluation of the cofferdam performance data and the results of the Plaxis 2D base model, the following conclusions can be drawn:

- A sudden increase in the displacement rate for ring beam elevations 3, 4 and 5 around construction days 69-70, associated to surface surcharges arising from a stock-pile of excavated material and the traffic of construction equipment, was identified. Surface surcharges should be considered a primary factor in the design of deep excavations as significant wall and ground movements can be induced. For this particular case, approximately 19 mm of the total cofferdam lateral wall deformation (57.6 mm) are attributed to surcharge loads.

- The stresses calculated in the concrete ring beams were significantly low with respect to the compressive strength of the concrete upon reaching 100% maturity. During the construction of the cofferdam, the stress demand/capacity indexes did not exceed, in any case, 40%. At the end of the excavation 6, the demand/capacity indexes did not exceed 20 % of the final

resistance. Similar to resistance, the concrete non-linear behavior is also significantly affected by aging and time-dependent effects. It was estimated that only 77 to 85% of the design stiffness was developed at the time the concrete ring beams underwent loading, which resulted in additional lateral displacements.

- The deviation between the computed and measured lateral displacements at the base of the cofferdam is attributed to the fact that the numerical analysis did not include the reduction in pore water pressures at the top of the rock formation due to the existing downward flow. As a result, the lateral earth pressures in the numerical cofferdam model are larger and consequently, the computed lateral displacements would increase. A fully coupled flow-deformation analysis is required to account for the above effects. These discrepancies can also be attributed to the limitations of the hypoplastic clay soil model to represent the response of hard or transition materials.

- Even though the Shotcrete constitutive model was developed for tunnel applications including non-reinforced concrete elements, it was found that it can adequately represent the non-linear concrete response and account for time-dependent effects in reinforced concrete structures. The validations made in this study for reinforced concrete ring beams were based on the procedures proposed by (Plaxis b.v 2016), where lightly reinforced concrete beams were used to validate the response predictions with the non-linear Shotcrete model.

Based on the parametric study, conducted to isolate the time-dependent effects of the concrete and evaluate their individual impact on the cofferdam horizontal displacements, the following conclusion can be drawn:

- Concrete time-dependent effects represent about 25% of the maximum horizontal displacements in the urban cofferdam braced with reinforced concrete ring beams analyzed in this study. Similar results were presented by (Arboleda-Monsalve 2014) for top-down excavations where concrete time-dependent effects represent 30% of the total lateral wall deformations.

- Aging effects were the most important concrete time-dependent component in the cofferdam performance. Aging induced-deformations for the considered case represent about 15% of the total horizontal displacements as calculated from the base model. Creep and shrinkage effects contribute around 6 and 3 %, respectively. As opposed to top-down excavation systems, shrinkage has no significant impact on the performance of cofferdams braced with reinforced concrete ring beams. It is because the surface exposed during the concrete curing process of a ring beam is much smaller than the exposed surface of a floor slab.

- The significance of the time-dependent effects found in this investigation for reinforced concrete ring beams used as bracing support system in urban cofferdams leads to conclude that these effects should be included, from the beginning, in the designs of the support systems. It allows to foresee additional deformations in the soil and consequently avoid damage to nearby structures or perimeter service lines.

5.2 Recommendations

Based on the detailed literature review, the careful study of the cofferdam performance, and the comprehensive numerical analyses conducted, the following recommendations are given:

- Surcharge loads due to heavy construction equipment are basically unavoidable for large excavations projects. However, attention must be focused on surcharges generated by excavated or construction material stock-piles around the excavation perimeter as they can significantly impact lateral displacements.

- When cracking sensitive structures are nearby, design criteria based on required stiffness must be used to size bracing concrete ring beam elements and define construction sequence in cofferdam structures. Strength-based design criteria must be avoided as cast-in-place concrete ring beams can be strong enough to resist the induced solicitation under an accelerated cofferdam construction sequence but can be still very flexible and undergo significant deformations.

- The author is aware that numerical modeling in practice is subjected to limited laboratory, field and performance data, so detailed or refined numerical analyses of an excavation project are difficult. This work pretends to raise awareness about concrete time-dependent effects and their impact on the final ground movements around cofferdam structures. Even though these ground movements are difficult to quantify, especially when coupled with advanced constitutive soil models, they are significant sources of movement that must be taken into account to protect adjacent infrastructure.

6. REFERENCES

ACI commite 209R-92. (1992). *Prediction of Creep, Shrinkage, and Temperature Effects in Concrete Structures, American Concrete Institute*. ACI.

Arboleda-Monsalve, L. G. (2014). "Performance, Instrumentation and Numerical Simulation of One Museum Park West Excavation." Northwestern University.

Arboleda-monsalve, L. G. and Finno, R. J. (2015). "Influence of Concrete Time-Dependent Effects on the Performance of Top-Down Construction."

Arboleda-Monsalve, L. G., Uribe-Henao, A. F., Velasquez-Perez, A., Zapata-Medina, D. G., and Sarabia, F. (2017). "Performance of urban cofferdams braced with segmental steel and reinforced concrete ring beams." *Journal of Geotechnical and Geoenvironmental Engineering*, Submmited(562), 1–35.

Blackburn, J. T. (2005). "Automated sensing and three-dimensional analysis of internally braced excavations." *Civil and environmental engineering*.

Brinkgreve, R. B. J., Swolfs, W. M., and Engin, E. (2011). "Reference Manual Plaxis." *Plaxis*.

"Ceb-Fip Model Code.".

Clough, W., and Kuppusamy, T. (1985). "Finite Element Analyses of Lock And Dam 26 Cofferdam." *American Society of Civil Engineers*, I, 521–541.

Collins, M. P., and Mitchel, D. (1991). *Presstressed Concrete in Structures*. Prentice-Hall Inc., Englewood Cliffs, New Jersey.

Duncan, J. M., Peter Byrne, Kai S. Wong, and Phillip Mabry. (1980). *Strength, Stress-Strain and Bulk Modulus Parameters For Finite Element Analyses Of Stresses and Movements in Soil Masses*. University of California.

Eurocode. (1992). "Eurocode 2: Design of concrete structures - Part 1-1 : General rules and rules for buildings." *British Standards Institution*, 1(2004), 230.

Fédération Internationale du Béton. (2010). *fib Model Code for Concrete Structures 2010*. Wilhem Ernst & Sohn, Berlin, Germany.

fib – fédération internationale du béton. (2013). "Materials." *fib Model Code for Concrete Structures 2010*, 74–150.

Finno, B. R. J., and Chung, C. (1993). “Stress-strain-strength responses of compressible chicago glacial clays.” 118(10), 1607–1625.

Finno, R. J., and Calvello, M. (2005). “Supported Excavations: Observational Method and Inverse Modeling.” *Journal of Geotechnical and Geoenvironmental Engineering*, 131(7), 826–836.

Galavi, V. (2010). “Internal Report Plaxis. Groundwater flow, fully coupled flow deformation and undrained analyses in PLAXIS 2D and 3D.” *Plaxis*, (April), 1–290.

Gallant, A. P. (2011). “A Parametric Study of Open Cell Cofferdam Construction at the Port of Anchorage Marine Terminal Redevelopment Project.” Northwestern University.

Herle, I., and Kolymbas, D. (2004). “Hypoplasticity for soils with low friction angles.” *Computers and Geotechnics*, 31(5), 365–373.

Kim, T., and Finno, R. J. (2012). “Anisotropy Evolution and Irrecoverable Deformation in Triaxial Stress Probes.” *Journal of Geotechnical and Geoenvironmental Engineering*, 138(2), 155–165.

Kolymbas, D., Wu, W., and Bauer, E. (1996). “Hypoplastic constitutive model with critical state for granular materials.” *Mechanics of Materials*, 23(1), 45–69.

Manitowoc. (2017). “Remote functions of Potain MCT 88 enable efficient Serbian bridge reconstruction.”

Mašín, D. (2005). “A hypoplastic constitutive model for clays.” *International Journal for Numerical and Analytical Methods in Geomechanics*, 29(4), 311–336.

Mašín, D. (2011). “PLAXIS implementation of hypoplasticity.” 30.

Mašín, D. (2012). “Clay hypoplasticity with explicitly defined asymptotic states.” *Acta Geotechnica*, 8(5), 481–496.

Mašín, D. (2014). “Clay hypoplasticity model including stiffness anisotropy.”

Mašín, D. (2015). “Hypoplasticity for Practical Applications.” (June), 1–26.

Meschke, G. (1996). “Consideration of aging of shotcrete in the context of A 3-D viscoplastic material model.” *International Journal for Numerical Methods in Engineering*, 39(18), 3123–3143.

Meschke, G., Kropik, C., and Mang, H. A. (1996). “Numerical analyses of tunnel linings by means of a viscoplastic material model for shotcrete.” *International Journal for Numerical Methods in Engineering*, 39(18), 3145–3162.

Nemati, K. M. (2005). “Temporary Structures Cofferdams.” *Advanced Topics In Civil Engineering*, TOKYO, 2.

Niemunis, A. (2002). “Extended hypoplastic models.” (January), 191.

Niemunis, A. (2003). “Anisotropic effects in hypoplasticity.” *Deformation Characteristics of*

Geomaterials.

Niemunis, A., and Herle, I. (1997). "Hypoplastic model for cohesionless soils with elastic strain range." *Mechanics of Cohesive-Frictional Materials*, 2(4), 279–299.

Niemunis, A., and Krieg, S. (1996). "Viscous behaviour of soils under oedometric conditions." *Canadian Geotechnical Journal*, 33, 159–168.

Orazalin, Z. Y., and Whittle, A. J. (2014). "3D Finite Element Analysis of a Complex Excavation." *Plaxis Bulletin*, (Spring), 16–21.

Plaxis b.v. (2016). "On the Use of the ShotCrete UDSM for Modelling Concrete."

Rowe, P. W. (1962). "The Stress-Dilatancy Relation for Static Equilibrium of an Assembly of Particles in Contact." *Proceedings of the Royal Society A: Mathematical, Physical and Engineering Sciences*, 269(1339), 500–527.

Sarabia, F. (2012). "Hypoplastic constitutive law adapted to simulate excavations in Chicago glacial clays." Northwestern University.

Schädlich, B., and Schweiger, H. F. (2014a). "Application of a novel constitutive shotcrete model to tunnelling." *Rock Engineering and Rock Mechanics: Structures in and on Rock Masses - Proceedings of EUROCK 2014, ISRM European Regional Symposium*, (May 2014), 799–804.

Schädlich, B., and Schweiger, H. F. (2014b). "A new constitutive model for shotcrete." *Numerical Methods in Geotechnical Engineering*, (2), 103–108.

Schanz, T., Vermeer, a, and Bonnier, P. (1999). "The hardening soil model: formulation and verification." *Beyond 2000 Comput. Geotech. 10 years PLAXIS Int. Proc. Int. Symp. beyond 2000 Comput. Geotech. Amsterdam Netherlands 1820 March 1999*, 281.

Schmieg, H., and Vielsack, P. (2002). "Transmission of Shear Forces in Sheet Pile Interlocks." (April), 292–297.

Schütz, R., Potts, D. M., and Zdravkovic, L. (2011). "Advanced constitutive modelling of shotcrete: Model formulation and calibration." *Computers and Geotechnics*, 38(6), 834–845.

United Nations. (2007). "World Urbanization Prospects The 2007 Revision Highlights." *Desa*, ESA/P/WP/2(4), 883.

Uribe-Henao, A. F., and Arboleda-Monsalve, L. G. (2016). "Sheet Pile Interlocks and Ring Beam Installation Effects on the Performance of Urban Cofferdams." 170–180.

Uribe-Henao, F. (2017). "Effects of Pre-Excavation Activities on the Performance of Urban Cofferdams." California State University, Long Beach.

Uribe-Henao, F., Arboleda-Monsalve, L. G., Velasquez-perez, A., Zapata-medina, D. G., and Sarabia, F. (2017). "Temperature and Concrete Time-Dependent Effects on Urban Cofferdams." 1–10.

Wissmann, K. J., Asce, M., Filz, G. M., Asce, M., Mosher, R. L., Asce, M., Ii, J. R. M., and Asce, M. (2003). “Sheet Pile Tensions in Cellular Structures.” (March), 224–233.

von Wolffersdorff, P. A. (1996). “Hypoplastic relation for granular materials with a predefined limit state surface.” *Mechanics of Cohesive-Frictional Materials*, 1(3), 251–271.

Wroth, C. P. (1984). “The interpretation of in situ soil tests.” *Géotechnique*, 34(4), 449–489.

Zapata-medina, D. G. (2012). “Evaluation of Dynamic Soil Parameter Changes Due to Construction–Induced Stresses.” Northwestern University.

7. APPENDIX A

Shotcrete model excel spreadsheet

Ring beam 1

Stress-strain curve (Collins and Mitchel 1991)

Parameters			$f_{c,n}$	f'_c	H_c	ε^e_c	ε^p_c	ε_c
				MPa				days
n	4.06			-2.52	-1			-0.00007
k	1.56		0.00	0.00	0.00	0.0000	0.0000	0
ε_c	0.0023		0.02	1.01	0.01	0.0000	0.0000	0.000032
ε_{cu}	0.0027		0.11	6.33	0.04	0.0002	0.0000	0.0002
			0.17	9.49	0.06	0.0002	0.0001	0.0003
f_{cm28}	55.49	**MPa**	0.23	12.65	0.08	0.0003	0.0001	0.0004
w	2400	**kg**	0.28	15.81	0.10	0.0004	0.0001	0.0005
Ec	31630.23	**MPa**	0.34	18.95	0.12	0.0005	0.0001	0.0006
E_{cm28}	38062.60	**MPa**	0.40	22.09	0.14	0.0006	0.0001	0.0007
	35233.13	**MPa**	0.45	25.20	0.16	0.0007	0.0001	0.0008
f_{tm28}	2.52	**MPa**	0.51	28.27	0.18	0.0007	0.0002	0.0009
ε_t	0.00007		0.56	31.30	0.20	0.0008	0.0002	0.001
			0.62	34.26	0.23	0.0009	0.0002	0.0011
g_r	0.013		0.67	37.13	0.26	0.0010	0.0002	0.0012
g_t	0.0069		0.72	39.90	0.29	0.0010	0.0003	0.0013
g_{ct}	0.043		0.77	42.52	0.33	0.0011	0.0003	0.0014
			0.81	44.98	0.37	0.0012	0.0003	0.0015
fcr	4.69	**MPa**	0.85	47.24	0.41	0.0012	0.0004	0.0016
G_c	51.43	**kPa**	0.89	49.28	0.47	0.0013	0.0004	0.0017
G^p_c	99.52	**kPa**	0.92	51.06	0.53	0.0013	0.0005	0.0018
Gt	0.083	**kPa**	0.95	52.57	0.60	0.0014	0.0005	0.0019
G^e_c	7.71	**kN/m**	0.97	53.77	0.68	0.0014	0.0006	0.002
G^e_c	14.928	**kN/m**	0.99	54.66	0.76	0.0014	0.0007	0.0021
Gt	0.01249	**kN/m**	1.00	55.23	0.86	0.0015	0.0007	0.0022
Leq	0.15	**m**	1.00	55.47	0.97	0.0015	0.0008	0.0023
			1.00	55.49	1.00	0.0015	0.0009	0.0023
			0.94	52.18	1.30	0.0014	0.0011	0.0025
			0.89	49.50	1.50	0.0013	0.0013	0.0026
			0.84	46.40	1.70	0.0012	0.0015	0.0027
			0.78	43.00	1.92	0.0011	0.0017	0.0028
			0.71	39.46	2.14	0.0010	0.0019	0.0029
			0.65	35.90	2.37	0.0009	0.0021	0.003
			0.58	32.42	2.59	0.0009	0.0022	0.0031
			0.52	29.11	2.80	0.0008	0.0024	0.0032
			0.47	26.01	3.01	0.0007	0.0026	0.0033
			0.42	23.17	3.21	0.0006	0.0028	0.0034
			0.37	20.58	3.41	0.0005	0.0030	0.0035
			0.33	18.25	3.59	0.0005	0.0031	0.0036
			0.29	16.17	3.77	0.0004	0.0033	0.0037
			0.26	14.33	3.94	0.0004	0.0034	0.0038
				55.49	0.66	0.0018	0.0006	0.0023

Stress-strain curve (Schütz et al. 2011)

Parameters			$f'_{cy,I}$	$H_{c,I}$	ε^p_c	$f'_{cy,II}$	$H_{c,II}$	ε^p_c	$f'_{cy,III}$	$H_{c,III}$	ε^p_c	$f'_{cy,IV}$	$H_{c,III}$	ε^p_c
			MPa			MPa			MPa			MPa		
f_{c0n}	0.00	0.00	0.00	0.00	0.00000	54.43	1.08	0.00095	13.96	4.28	0.00375	0.00	5.1	0.00448
f_{cfn}	0.26	14.33	1.10	0.01	0.00001	53.37	1.17	0.00102	13.59	4.3	0.00377	0.00	100.0	0.08757
f_{cun}	0.00	0.00	2.20	0.02	0.00002	52.32	1.25	0.00110	13.23	4.3	0.00378			
f_{tun}	1		3.28	0.03	0.00003	51.26	1.33	0.00117	12.86	4.3	0.00380	f_{yt}	H_t	
H_{cf}	4.26		4.35	0.04	0.00004	50.21	1.42	0.00124	12.49	4.4	0.00382	MPa		
H_{cu}	5.12		5.41	0.05	0.00004	49.15	1.50	0.00131	12.12	4.4	0.00384	-2.52	0	
			6.46	0.06	0.00005	48.10	1.58	0.00139	11.76	4.4	0.00386	-2.52	-1	
ε_{cp}	-0.0023		7.50	0.07	0.00006	47.04	1.67	0.00146	11.39	4.4	0.00388			
ε^e_{cp}	-0.0015	**Collins**	8.52	0.08	0.00007	45.99	1.75	0.00153	11.02	4.5	0.00390	$\varepsilon(t)_{cp}$	**t**	
ε^p_{cp}	-0.00088	-0.00087	9.54	0.09	0.00008	44.93	1.83	0.00161	10.65	4.5	0.00392	MPa	Hrs	
ε^p_{cf}	-0.0037	-0.0034	10.54	0.10	0.00009	43.88	1.92	0.00168	10.29	4.5	0.00394	-0.0100	1	
ε^p_{cu}	-0.0045		11.54	0.11	0.00010	42.82	2.00	0.00175	9.92	4.5	0.00396	-0.0013	1.1	
ε^p_{tu}	0.000033	0.000066	12.52	0.12	0.00011	41.77	2.09	0.00183	9.55	4.5	0.00398	-0.0013	1	
	1.0077126		13.49	0.13	0.00011	40.71	2.17	0.00190	9.18	4.6	0.00400	-0.0012	1.3	
A	0.009		14.45	0.14	0.00012	39.66	2.25	0.00197	8.82	4.6	0.00402	-0.0012	1	
B	0.012		15.40	0.15	0.00013	38.60	2.34	0.00205	8.45	4.6	0.00404	-0.0012	1.5	
C	-0.01000		16.33	0.16	0.00014	37.55	2.42	0.00212	8.08	4.6	0.00405	-0.0012	2	
D	0.0120	**t [hrs]**	17.26	0.17	0.00015	36.49	2.50	0.00219	7.72	4.7	0.00407	-0.0010	4	
ε_{1h}	-0.01000	**1**	18.18	0.18	0.00016	35.43	2.59	0.00226	7.35	4.7	0.00409	-0.0010	8	
ε_{8h}	-0.0010	**8**	19.08	0.19	0.00017	34.38	2.67	0.00234	6.98	4.7	0.00411	-0.0010	10	
ε_{24h}	-0.00095	**24**	19.97	0.20	0.00018	33.32	2.75	0.00241	6.61	4.7	0.00413	-0.0010	12	
			20.86	0.21	0.00018	32.27	2.84	0.00248	6.25	4.7	0.00415	-0.0010	24	
G^p_c	14.93	**kN/m**	21.73	0.22	0.00019	31.21	2.92	0.00256	5.88	4.8	0.00417	-0.0009	28	
G^p_t	0.0125	**kN/m**	22.59	0.23	0.00020	30.16	3.00	0.00263	5.51	4.8	0.00419	-0.0009	48	
L_{eq}	0.15	**m**	23.44	0.24	0.00021	29.10	3.09	0.00270	5.14	4.8	0.00421	-0.0009	72	
			24.27	0.25	0.00022	28.05	3.17	0.00278	4.78	4.8	0.00423	-0.0009	96	
f_{cm28}	55.49	**MPa**	25.10	0.26	0.00023	26.99	3.25	0.00285	4.41	4.9	0.00425	-0.0009	120	
E_c	38062.60	**MPa**	25.92	0.27	0.00024	25.94	3.34	0.00292	4.04	4.9	0.00427	-0.0009	144	
f_{tm28}	2.52	**MPa**	26.72	0.28	0.00025	24.88	3.42	0.00300	3.67	4.9	0.00429	-0.0009	168	
ε_t	0.00007		27.52	0.29	0.00025	23.83	3.50	0.00307	3.31	4.9	0.00431	-0.0009	192	
	0.00008		28.30	0.30	0.00026	22.77	3.59	0.00314	2.94	4.9	0.00433	-0.0009	216	
			32.04	0.35	0.00031	21.72	3.67	0.00321	2.57	5.0	0.00434	-0.0009	240	
E_1	14582.281	**MPa**	35.51	0.40	0.00035	20.66	3.75	0.00329	2.20	5.0	0.00436	-0.0009	264	
$f_{c,1}$	7.61	**MPa**	41.61	0.50	0.00044	19.60	3.84	0.00336	1.84	5.0	0.00438	-0.0009	288	
ϕ^{cr}_{∞}	1.38		46.61	0.60	0.00053	18.55	3.92	0.00343	1.47	5.0	0.00440	-0.0009	312	
t^{cr}_{50}	9.00	**days**	50.49	0.70	0.00061	17.49	4.01	0.00351	1.10	5.0	0.00442	-0.0009	336	
t^{shr}_{50}	50.00	**days**	53.27	0.80	0.00070	16.44	4.09	0.00358	0.73	5.1	0.00444	-0.0009	360	
$\varepsilon^{shr}_{\infty}$	-0.0002033		54.93	0.90	0.00079	15.38	4.17	0.00365	0.37	5.1	0.00446	-0.0009	672	28
E1/Ec	0.3831131		55.49	1.00	0.00088	14.33	4.26	0.00373	0.00	5.1	0.00448	-0.0009	784	
fc1/fc	0.1371478											-0.0009	896	

Ring beam 2

Stress-strain curve (Collins and Mitchel 1991)

Parameters			$f_{c,n}$	f'_c	H_c	ε^e_c	ε^p_c	ε_c
				MPa				days
n	3.95			-2.47	-1			-0.00007
k	1.53		0.00	0.00	0.00	0.0000	0.0000	0
ε_c	0.0023		0.06	3.12	0.02	0.0001	0.0000	0.0001
ε_{cu}	0.0027		0.12	6.24	0.04	0.0002	0.0000	0.0002
			0.17	9.36	0.06	0.0002	0.0001	0.0003
f_{cm28}	53.53	**MPa**	0.23	12.47	0.08	0.0003	0.0001	0.0004
w	2400	**kg**	0.29	15.58	0.10	0.0004	0.0001	0.0005
Ec	31189.68	**MPa**	0.35	18.68	0.12	0.0005	0.0001	0.0006
E_{cm28}	37609.21	**MPa**	0.41	21.77	0.14	0.0006	0.0001	0.0007
	34605.48	**MPa**	0.46	24.82	0.16	0.0007	0.0001	0.0008
f_{tm28}	2.47	**MPa**	0.52	27.84	0.18	0.0007	0.0002	0.0009
ε_t	0.00007		0.58	30.80	0.21	0.0008	0.0002	0.001
			0.63	33.69	0.23	0.0009	0.0002	0.0011
g_r	0.013		0.68	36.48	0.26	0.0010	0.0002	0.0012
g_t	0.0069		0.73	39.15	0.30	0.0010	0.0003	0.0013
g_{ct}	0.043		0.78	41.67	0.33	0.0011	0.0003	0.0014
			0.82	44.02	0.38	0.0012	0.0003	0.0015
fcr	4.61	**MPa**	0.86	46.16	0.43	0.0012	0.0004	0.0016
G_c	51.15	**kPa**	0.90	48.07	0.48	0.0013	0.0004	0.0017
G^p_c	96.39	**kPa**	0.93	49.72	0.55	0.0013	0.0005	0.0018
Gt	0.081	**kPa**	0.95	51.09	0.62	0.0014	0.0005	0.0019
G^e_c	7.67	**kN/m**	0.97	52.16	0.70	0.0014	0.0006	0.002
G^e_c	14.458	**kN/m**	0.99	52.93	0.79	0.0014	0.0007	0.0021
Gt	0.0122	**kN/m**	1.00	53.38	0.89	0.0014	0.0008	0.0022
Leq	0.15	**m**	1.00	53.50	1.00	0.0014	0.0009	0.0023
			1.00	53.53	1.00	0.0014	0.0009	0.0023
			0.93	49.84	1.34	0.0013	0.0012	0.0025
			0.88	47.26	1.54	0.0013	0.0013	0.0026
			0.83	44.33	1.74	0.0012	0.0015	0.0027
			0.77	41.17	1.95	0.0011	0.0017	0.0028
			0.71	37.90	2.16	0.0010	0.0019	0.0029
			0.65	34.62	2.38	0.0009	0.0021	0.003
			0.59	31.43	2.59	0.0008	0.0023	0.0031
			0.53	28.38	2.79	0.0008	0.0024	0.0032
			0.48	25.53	3.00	0.0007	0.0026	0.0033
			0.43	22.89	3.19	0.0006	0.0028	0.0034
			0.38	20.48	3.38	0.0005	0.0030	0.0035
			0.34	18.30	3.56	0.0005	0.0031	0.0036
			0.31	16.34	3.73	0.0004	0.0033	0.0037
			0.27	14.59	3.90	0.0004	0.0034	0.0038
				53.53	0.67	0.0017	0.0006	0.0023

Stress-strain curve (Schütz et al. 2011)

Parameters			$f'_{cy,I}$	$H_{c,I}$	ε^p_c	$f'_{cy,II}$	$H_{c,II}$	ε^p_c	$f'_{cy,III}$	$H_{c,III}$	ε^p_c	$f'_{cy,IV}$	$H_{c,III}$	ε^p_c
			MPa			MPa			MPa			MPa		
f_{c0n}	0.00	0.00	0.00	0.00	0.00000	52.53	1.08	0.00095	14.22	4.24	0.00373	0.00	5.1	0.00448
f_{cfn}	0.27	14.59	1.07	0.01	0.00001	51.53	1.17	0.00102	13.84	4.3	0.00375	0.00	100.0	0.08784
f_{cun}	0.00	0.00	2.12	0.02	0.00002	50.53	1.25	0.00110	13.47	4.3	0.00377			
f_{tun}	1		3.16	0.03	0.00003	49.53	1.33	0.00117	13.09	4.3	0.00379	f_{yt}	H_t	
H_{cf}	4.22		4.20	0.04	0.00004	48.53	1.41	0.00124	12.72	4.3	0.00381	MPa		
H_{cu}	5.11		5.22	0.05	0.00004	47.54	1.50	0.00131	12.35	4.4	0.00383	-2.47	0	
			6.23	0.06	0.00005	46.54	1.58	0.00139	11.97	4.4	0.00385	-2.47	-1	
ε_{cp}	-0.0023		7.23	0.07	0.00006	45.54	1.66	0.00146	11.60	4.4	0.00387			
ε^e_{cp}	-0.0014	**Collins**	8.22	0.08	0.00007	44.54	1.74	0.00153	11.22	4.4	0.00389	$\varepsilon(t)_{cp}$	**t**	
ε^p_{cp}	-0.00088	-0.00087	9.20	0.09	0.00008	43.54	1.83	0.00160	10.85	4.4	0.00391	MPa	Hrs	
ε^p_{cf}	-0.0037	-0.0034	10.17	0.10	0.00009	42.54	1.91	0.00168	10.47	4.5	0.00393	-0.0100	1	
ε^p_{cu}	-0.0045		11.13	0.11	0.00010	41.55	1.99	0.00175	10.10	4.5	0.00395	-0.0013	1.1	
ε^p_{tu}	0.000033	0.000066	12.08	0.12	0.00011	40.55	2.07	0.00182	9.73	4.5	0.00397	-0.0013	1	
	1.0039501		13.01	0.13	0.00011	39.55	2.16	0.00189	9.35	4.5	0.00399	-0.0012	1.3	
A	0.009		13.94	0.14	0.00012	38.55	2.24	0.00197	8.98	4.6	0.00401	-0.0012	1	
B	0.012		14.85	0.15	0.00013	37.55	2.32	0.00204	8.60	4.6	0.00403	-0.0012	1.5	
C	-0.01000		15.76	0.16	0.00014	36.55	2.40	0.00211	8.23	4.6	0.00405	-0.0012	2	
D	0.0118	**t [hrs]**	16.65	0.17	0.00015	35.56	2.49	0.00218	7.86	4.6	0.00407	-0.0010	4	
ε_{1h}	-0.01000	**1**	17.54	0.18	0.00016	34.56	2.57	0.00226	7.48	4.7	0.00409	-0.0010	8	
ε_{8h}	-0.0010	**8**	18.41	0.19	0.00017	33.56	2.65	0.00233	7.11	4.7	0.00411	-0.0010	10	
ε_{24h}	-0.00096	**24**	19.27	0.20	0.00018	32.56	2.73	0.00240	6.73	4.7	0.00413	-0.0010	12	
			20.12	0.21	0.00018	31.56	2.82	0.00247	6.36	4.7	0.00415	-0.0010	24	
G^p_c	14.46	**kN/m**	20.96	0.22	0.00019	30.56	2.90	0.00255	5.99	4.7	0.00417	-0.0009	28	
G^p_t	0.0122	**kN/m**	21.79	0.23	0.00020	29.57	2.98	0.00262	5.61	4.8	0.00419	-0.0009	48	
L_{eq}	0.15	**m**	22.61	0.24	0.00021	28.57	3.07	0.00269	5.24	4.8	0.00421	-0.0009	72	
			23.42	0.25	0.00022	27.57	3.15	0.00277	4.86	4.8	0.00423	-0.0009	96	
f_{cm28}	53.53	**MPa**	24.22	0.26	0.00023	26.57	3.23	0.00284	4.49	4.8	0.00425	-0.0009	120	
E_c	37609.21	**MPa**	25.00	0.27	0.00024	25.57	3.31	0.00291	4.12	4.9	0.00427	-0.0009	144	
f_{tm28}	2.47	**MPa**	25.78	0.28	0.00025	24.57	3.40	0.00298	3.74	4.9	0.00429	-0.0009	168	
ε_t	0.00007		26.54	0.29	0.00025	23.58	3.48	0.00306	3.37	4.9	0.00431	-0.0009	192	
	0.00008		27.30	0.30	0.00026	22.58	3.56	0.00313	2.99	4.9	0.00433	-0.0009	216	
			30.91	0.35	0.00031	21.58	3.64	0.00320	2.62	4.9	0.00435	-0.0009	240	
E_1	14396.035	**MPa**	34.26	0.40	0.00035	20.58	3.73	0.00327	2.24	5.0	0.00436	-0.0009	264	
$f_{c,1}$	7.33	**MPa**	40.14	0.50	0.00044	19.58	3.81	0.00335	1.87	5.0	0.00438	-0.0009	288	
ϕ^{cr}_{∞}	1.42		44.96	0.60	0.00053	18.58	3.89	0.00342	1.50	5.0	0.00440	-0.0009	312	
t^{cr}_{50}	9.00	**days**	48.71	0.70	0.00061	17.59	3.97	0.00349	1.12	5.0	0.00442	-0.0009	336	
t^{shr}_{50}	50	**days**	51.39	0.80	0.00070	16.59	4.06	0.00356	0.75	5.1	0.00444	-0.0009	360	28
$\varepsilon^{shr}_{\infty}$	-0.0001917		52.99	0.90	0.00079	15.59	4.14	0.00364	0.37	5.1	0.00446	-0.0009	672	
E1/Ec	0.3827795		53.53	1.00	0.00088	14.59	4.22	0.00371	0.00	5.1	0.00448	-0.0009	784	
fc1/fc	0.1370284											-0.0009	896	
t_{hyd}	54.00													

Ring beam 3

Stress-strain curve (Collins and Mitchel 1991)

Parameters			$f_{c,n}$	f'_c	H_c	ε^e_c	ε^p_c	ε_c
				MPa				days
n	4.64			-2.73	-1			-0.00007
k	1.72		0.00	0.00	0.00	0.0000	0.0000	0
ε_c	0.0025		0.05	3.37	0.02	0.0001	0.0000	0.0001
ε_{cu}	0.0026		0.10	6.74	0.04	0.0002	0.0000	0.0002
			0.15	10.12	0.06	0.0003	0.0000	0.0003
f_{cm28}	65.28	**MPa**	0.21	13.49	0.08	0.0003	0.0001	0.0004
w	2400	**kg**	0.26	16.86	0.10	0.0004	0.0001	0.0005
Ec	33723.49	**MPa**	0.31	20.23	0.11	0.0005	0.0001	0.0006
E_{cm28}	40181.24	**MPa**	0.36	23.59	0.13	0.0006	0.0001	0.0007
	38215.40	**MPa**	0.41	26.94	0.15	0.0007	0.0001	0.0008
f_{tm28}	2.73	**MPa**	0.46	30.27	0.17	0.0008	0.0001	0.0009
ε_t	0.00007		0.51	33.58	0.19	0.0008	0.0002	0.001
			0.56	36.86	0.22	0.0009	0.0002	0.0011
g_r	0.013		0.61	40.08	0.24	0.0010	0.0002	0.0012
g_t	0.0069		0.66	43.23	0.27	0.0011	0.0002	0.0013
g_{ct}	0.043		0.71	46.30	0.29	0.0012	0.0002	0.0014
			0.75	49.24	0.33	0.0012	0.0003	0.0015
fcr	5.09	**MPa**	0.80	52.04	0.36	0.0013	0.0003	0.0016
G_c	52.32	**kPa**	0.84	54.66	0.40	0.0014	0.0003	0.0017
G^p_c	115.37	**kPa**	0.87	57.07	0.45	0.0014	0.0004	0.0018
Gt	0.093	**kPa**	0.91	59.23	0.51	0.0015	0.0004	0.0019
G^e_c	7.85	**kN/m**	0.94	61.11	0.57	0.0015	0.0005	0.002
G^e_c	17.306	**kN/m**	0.96	62.67	0.64	0.0016	0.0005	0.0021
Gt	0.01392	**kN/m**	0.98	63.88	0.72	0.0016	0.0006	0.0022
Leq	0.15	**m**	0.99	64.73	0.82	0.0016	0.0007	0.0023
			1.00	65.28	1.00	0.0016	0.0008	0.0025
			0.99	64.60	1.06	0.0016	0.0009	0.0025
			0.95	61.86	1.26	0.0015	0.0011	0.0026
			0.89	58.20	1.48	0.0014	0.0013	0.0027
			0.82	53.81	1.73	0.0013	0.0015	0.0028
			0.75	48.92	2.00	0.0012	0.0017	0.0029
			0.67	43.79	2.27	0.0011	0.0019	0.003
			0.59	38.68	2.54	0.0010	0.0021	0.0031
			0.52	33.78	2.80	0.0008	0.0024	0.0032
			0.45	29.23	3.05	0.0007	0.0026	0.0033
			0.38	25.12	3.29	0.0006	0.0028	0.0034
			0.33	21.49	3.52	0.0005	0.0030	0.0035
			0.28	18.32	3.73	0.0005	0.0031	0.0036
			0.24	15.59	3.93	0.0004	0.0033	0.0037
			0.20	13.25	4.12	0.0003	0.0035	0.0038
				65.28	0.63	0.0019	0.0005	0.0025

Stress-strain curve (Schütz et al. 2011)

Parameters			$f'_{cy,I}$	$H_{c,I}$	ε^p_c	$f'_{cy,II}$	$H_{c,II}$	ε^p_c	$f'_{cy,III}$	$H_{c,III}$	ε^p_c	$f'_{cy,IV}$	$H_{c,III}$	ε^p_c
			MPa			MPa			MPa			MPa		
f_{c0n}	0.00	0.00	0.00	0.00	0.00000	63.94	1.09	0.00092	12.91	4.49	0.00380	0.00	5.3	0.00444
f_{cfn}	0.20	13.25	1.30	0.01	0.00001	62.61	1.18	0.00100	12.57	4.5	0.00382	0.00	100.0	0.08462
f_{cun}	0.00	0.00	2.58	0.02	0.00002	61.27	1.27	0.00107	12.23	4.5	0.00384			
f_{tun}	1		3.86	0.03	0.00003	59.94	1.36	0.00115	11.89	4.6	0.00385	f_{yt}	H_t	
H_{cf}	4.47		5.12	0.04	0.00003	58.61	1.45	0.00122	11.55	4.6	0.00387	MPa		
H_{cu}	5.25		6.36	0.05	0.00004	57.27	1.53	0.00130	11.21	4.6	0.00389	-2.73	0	
			7.60	0.06	0.00005	55.94	1.62	0.00137	10.87	4.6	0.00390	-2.73	-1	
ε_{cp}	-0.0025		8.82	0.07	0.00006	54.60	1.71	0.00145	10.53	4.6	0.00392			
ε^e_{cp}	-0.0016	**Collins**	10.03	0.08	0.00007	53.27	1.80	0.00152	10.19	4.7	0.00394	$\varepsilon(t)_{cp}$	**t**	
ε^p_{cp}	-0.00085	-0.00084	11.22	0.09	0.00008	51.94	1.89	0.00160	9.85	4.7	0.00395	MPa	Hrs	
ε^p_{cf}	-0.0038	-0.0035	12.40	0.10	0.00008	50.60	1.98	0.00167	9.51	4.7	0.00397	-0.0120	1	
ε^p_{cu}	-0.0044		13.57	0.11	0.00009	49.27	2.07	0.00175	9.17	4.7	0.00399	-0.0017	1.1	
ε^p_{tu}	0.000034	0.000068	14.73	0.12	0.00010	47.93	2.16	0.00183	8.83	4.7	0.00400	-0.0016	1	
	1.0038771		15.87	0.13	0.00011	46.60	2.25	0.00190	8.49	4.8	0.00402	-0.0015	1.3	
A	0.011		17.00	0.14	0.00012	45.27	2.34	0.00198	8.15	4.8	0.00404	-0.0015	1	
B	0.019		18.11	0.15	0.00013	43.93	2.42	0.00205	7.82	4.8	0.00406	-0.0014	1.5	
C	-0.01200		19.22	0.16	0.00014	42.60	2.51	0.00213	7.48	4.8	0.00407	-0.0014	2	
D	0.0194	**t [hrs]**	20.31	0.17	0.00014	41.26	2.60	0.00220	7.14	4.8	0.00409	-0.0012	4	
ε_{1h}	-0.01200	**1**	21.38	0.18	0.00015	39.93	2.69	0.00228	6.80	4.9	0.00411	-0.0011	8	
ε_{8h}	-0.0011	**8**	22.45	0.19	0.00016	38.60	2.78	0.00235	6.46	4.9	0.00412	-0.0011	10	
ε_{24h}	-0.00100	**24**	23.50	0.20	0.00017	37.26	2.87	0.00243	6.12	4.9	0.00414	-0.0011	12	
			24.54	0.21	0.00018	35.93	2.96	0.00250	5.78	4.9	0.00416	-0.0010	24	
G^p_c	17.31	**kN/m**	25.56	0.22	0.00019	34.60	3.05	0.00258	5.44	4.9	0.00417	-0.0010	28	
G^p_t	0.0139	**kN/m**	26.57	0.23	0.00019	33.26	3.14	0.00265	5.10	5.0	0.00419	-0.0010	48	
L_{eq}	0.15	**m**	27.57	0.24	0.00020	31.93	3.23	0.00273	4.76	5.0	0.00421	-0.0009	72	
			28.56	0.25	0.00021	30.59	3.32	0.00281	4.42	5.0	0.00422	-0.0009	96	
f_{cm28}	65.28	**MPa**	29.53	0.26	0.00022	29.26	3.40	0.00288	4.08	5.0	0.00424	-0.0009	120	
E_c	40181.24	**MPa**	30.49	0.27	0.00023	27.93	3.49	0.00296	3.74	5.0	0.00426	-0.0009	144	
f_{tm28}	2.73	**MPa**	31.44	0.28	0.00024	26.59	3.58	0.00303	3.40	5.1	0.00428	-0.0009	168	
ε_t	0.00007		32.37	0.29	0.00025	25.26	3.67	0.00311	3.06	5.1	0.00429	-0.0009	192	
	0.00008		33.29	0.30	0.00025	23.92	3.76	0.00318	2.72	5.1	0.00431	-0.0009	216	
			37.70	0.35	0.00030	22.59	3.85	0.00326	2.38	5.1	0.00433	-0.0009	240	
E_1	15355.118	**MPa**	41.78	0.40	0.00034	21.26	3.94	0.00333	2.04	5.1	0.00434	-0.0009	264	
$f_{c,1}$	8.93	**MPa**	48.96	0.50	0.00042	19.92	4.03	0.00341	1.70	5.2	0.00436	-0.0009	288	
ϕ^{cr}_{∞}	1.22		54.83	0.60	0.00051	18.59	4.12	0.00348	1.36	5.2	0.00438	-0.0009	312	
t^{cr}_{50}	9.00	**days**	59.40	0.70	0.00059	17.25	4.21	0.00356	1.02	5.2	0.00439	-0.0009	336	
t^{shr}_{50}	50	**days**	62.67	0.80	0.00068	15.92	4.29	0.00363	0.68	5.2	0.00441	-0.0009	360	28
$\varepsilon^{shr}_{\infty}$	-0.0002052		64.62	0.90	0.00076	14.59	4.38	0.00371	0.34	5.2	0.00443	-0.0008	672	
E1/Ec	0.3821465		65.28	1.00	0.00085	13.25	4.47	0.00378	0.00	5.3	0.00444	-0.0008	784	
fc1/fc	0.1368018											-0.0008	896	
t_{hyd}	54.00													

Ring beam 4

Stress-strain curve (Collins and Mitchel 1991)

Parameters			$f_{c,n}$	f'_c	H_c	ε^e_c	ε^p_c	ε_c
				MPa				days
n	4.49			-2.68	-1			-0.00007
k	1.68		0.00	0.00	0.00	0.0000	0.0000	0
ε_c	0.0024		0.05	3.32	0.02	0.0001	0.0000	0.0001
ε_{cu}	0.0026		0.11	6.64	0.04	0.0002	0.0000	0.0002
			0.16	9.96	0.06	0.0003	0.0000	0.0003
f_{cm28}	62.71	**MPa**	0.21	13.28	0.08	0.0003	0.0001	0.0004
w	2400	**kg**	0.26	16.59	0.10	0.0004	0.0001	0.0005
Ec	33190.51	**MPa**	0.32	19.90	0.12	0.0005	0.0001	0.0006
E_{cm28}	39647.19	**MPa**	0.37	23.21	0.13	0.0006	0.0001	0.0007
	37456.06	**MPa**	0.42	26.50	0.15	0.0007	0.0001	0.0008
f_{tm28}	2.68	**MPa**	0.47	29.77	0.18	0.0008	0.0001	0.0009
ε_t	0.00007		0.53	33.01	0.20	0.0008	0.0002	0.001
			0.58	36.21	0.22	0.0009	0.0002	0.0011
g_r	0.013		0.63	39.35	0.24	0.0010	0.0002	0.0012
g_t	0.0069		0.68	42.42	0.27	0.0011	0.0002	0.0013
g_{ct}	0.043		0.72	45.37	0.30	0.0011	0.0003	0.0014
			0.77	48.20	0.33	0.0012	0.0003	0.0015
fcr	4.99	**MPa**	0.81	50.87	0.37	0.0013	0.0003	0.0016
G_c	52.16	**kPa**	0.85	53.35	0.42	0.0013	0.0004	0.0017
G^p_c	111.18	**kPa**	0.89	55.61	0.47	0.0014	0.0004	0.0018
Gt	0.090	**kPa**	0.92	57.60	0.53	0.0015	0.0004	0.0019
G^e_c	7.82	**kN/m**	0.95	59.30	0.59	0.0015	0.0005	0.002
G^e_c	16.677	**kN/m**	0.97	60.68	0.67	0.0015	0.0006	0.0021
Gt	0.01355	**kN/m**	0.98	61.72	0.76	0.0016	0.0006	0.0022
Leq	0.15	**m**	0.99	62.39	0.86	0.0016	0.0007	0.0023
			1.00	62.71	1.00	0.0016	0.0008	0.0024
			0.98	61.27	1.12	0.0015	0.0010	0.0025
			0.93	58.46	1.33	0.0015	0.0011	0.0026
			0.88	54.87	1.55	0.0014	0.0013	0.0027
			0.81	50.70	1.79	0.0013	0.0015	0.0028
			0.74	46.15	2.04	0.0012	0.0017	0.0029
			0.66	41.45	2.30	0.0010	0.0020	0.003
			0.59	36.80	2.56	0.0009	0.0022	0.0031
			0.52	32.36	2.81	0.0008	0.0024	0.0032
			0.45	28.24	3.05	0.0007	0.0026	0.0033
			0.39	24.50	3.28	0.0006	0.0028	0.0034
			0.34	21.17	3.49	0.0005	0.0030	0.0035
			0.29	18.24	3.70	0.0005	0.0031	0.0036
			0.25	15.69	3.89	0.0004	0.0033	0.0037
			0.22	13.49	4.07	0.0003	0.0035	0.0038
				62.71	0.64	0.0019	0.0005	0.0024

Stress-strain curve (Schütz et al. 2011)

Parameters			$f'_{cy,I}$	$H_{c,I}$	ε^p_c	$f'_{cy,II}$	$H_{c,II}$	ε^p_c	$f'_{cy,III}$	$H_{c,III}$	ε^p_c	$f'_{cy,IV}$	$H_{c,III}$	ε^p_c
			MPa			MPa			MPa			MPa		
f_{c0n}	0.00	0.00	0.00	0.00	0.00000	61.45	1.09	0.00092	13.14	4.45	0.00379	0.00	5.2	0.00445
f_{cfn}	0.22	13.49	1.25	0.01	0.00001	60.18	1.18	0.00100	12.80	4.5	0.00380	0.00	100.0	0.08498
f_{cun}	0.00	0.00	2.48	0.02	0.00002	58.92	1.26	0.00107	12.45	4.5	0.00382			
f_{tun}	1		3.71	0.03	0.00003	57.66	1.35	0.00115	12.11	4.5	0.00384	f_{yt}	H_t	
H_{cf}	4.43		4.92	0.04	0.00003	56.40	1.44	0.00122	11.76	4.5	0.00386	MPa		
H_{cu}	5.23		6.11	0.05	0.00004	55.14	1.53	0.00130	11.41	4.6	0.00387	-2.68	0	
			7.30	0.06	0.00005	53.87	1.62	0.00137	11.07	4.6	0.00389	-2.68	-1	
ε_{cp}	-0.0024		8.47	0.07	0.00006	52.61	1.70	0.00145	10.72	4.6	0.00391			
ε^e_{cp}	-0.0016	**Collins**	9.63	0.08	0.00007	51.35	1.79	0.00152	10.38	4.6	0.00392	$\varepsilon(t)_{cp}$	**t**	
ε^p_{cp}	-0.00085	-0.00085	10.78	0.09	0.00008	50.09	1.88	0.00160	10.03	4.6	0.00394	MPa	Hrs	
ε^p_{cf}	-0.0038	-0.0035	11.91	0.10	0.00008	48.83	1.97	0.00167	9.68	4.7	0.00396	-0.0120	1	
ε^p_{cu}	-0.0044		13.04	0.11	0.00009	47.56	2.06	0.00175	9.34	4.7	0.00398	-0.0016	1.1	
ε^p_{tu}	0.000034	0.000068	14.15	0.12	0.00010	46.30	2.14	0.00182	8.99	4.7	0.00399	-0.0015	1	
	1.0006044		15.24	0.13	0.00011	45.04	2.23	0.00190	8.65	4.7	0.00401	-0.0014	1.3	
A	0.011		16.33	0.14	0.00012	43.78	2.32	0.00197	8.30	4.7	0.00403	-0.0014	1	
B	0.016		17.40	0.15	0.00013	42.52	2.41	0.00205	7.96	4.8	0.00405	-0.0013	1.5	
C	-0.01200		18.46	0.16	0.00014	41.25	2.50	0.00212	7.61	4.8	0.00406	-0.0013	2	
D	0.0159	**t [hrs]**	19.51	0.17	0.00014	39.99	2.58	0.00220	7.26	4.8	0.00408	-0.0011	4	
ε_{1h}	-0.01200	**1**	20.54	0.18	0.00015	38.73	2.67	0.00227	6.92	4.8	0.00410	-0.0011	8	
ε_{8h}	-0.0011	**8**	21.57	0.19	0.00016	37.47	2.76	0.00235	6.57	4.8	0.00412	-0.0010	10	
ε_{24h}	-0.00098	**24**	22.57	0.20	0.00017	36.21	2.85	0.00242	6.23	4.9	0.00413	-0.0010	12	
			23.57	0.21	0.00018	34.94	2.94	0.00250	5.88	4.9	0.00415	-0.0010	24	
G^p_c	16.68	**kN/m**	24.56	0.22	0.00019	33.68	3.03	0.00257	5.53	4.9	0.00417	-0.0010	28	
G^p_t	0.0136	**kN/m**	25.53	0.23	0.00020	32.42	3.11	0.00265	5.19	4.9	0.00419	-0.0009	48	
L_{eq}	0.15	**m**	26.49	0.24	0.00020	31.16	3.20	0.00272	4.84	4.9	0.00420	-0.0009	72	
			27.43	0.25	0.00021	29.90	3.29	0.00280	4.50	5.0	0.00422	-0.0009	96	
f_{cm28}	62.71	**MPa**	28.37	0.26	0.00022	28.63	3.38	0.00287	4.15	5.0	0.00424	-0.0009	120	
E_c	39647.19	**MPa**	29.29	0.27	0.00023	27.37	3.47	0.00294	3.80	5.0	0.00426	-0.0009	144	
f_{tm28}	2.68	**MPa**	30.20	0.28	0.00024	26.11	3.55	0.00302	3.46	5.0	0.00427	-0.0009	168	
ε_t	0.00007		31.10	0.29	0.00025	24.85	3.64	0.00309	3.11	5.1	0.00429	-0.0009	192	
	0.00008		31.98	0.30	0.00025	23.59	3.73	0.00317	2.77	5.1	0.00431	-0.0009	216	
			36.21	0.35	0.00030	22.32	3.82	0.00324	2.42	5.1	0.00433	-0.0009	240	
E_1	17887.513	**MPa**	40.13	0.40	0.00034	21.06	3.91	0.00332	2.08	5.1	0.00434	-0.0009	264	
$f_{c,1}$	12.01	**MPa**	47.03	0.50	0.00042	19.80	3.99	0.00339	1.73	5.1	0.00436	-0.0009	288	
ϕ^{cr}_{∞}	1.23		52.67	0.60	0.00051	18.54	4.08	0.00347	1.38	5.2	0.00438	-0.0009	312	
t^{cr}_{50}	9.00	**days**	57.06	0.70	0.00059	17.28	4.17	0.00354	1.04	5.2	0.00440	-0.0009	336	
t^{shr}_{50}	50	**days**	60.20	0.80	0.00068	16.01	4.26	0.00362	0.69	5.2	0.00441	-0.0009	360	28
$\varepsilon^{shr}_{\infty}$	-0.0002080		62.08	0.90	0.00076	14.75	4.35	0.00369	0.35	5.2	0.00443	-0.0008	672	
E1/Ec	0.4511672		62.71	1.00	0.00085	13.49	4.43	0.00377	0.00	5.2	0.00445	-0.0008	784	
fc1/fc	0.1914827											-0.0008	896	
t_{hyd}	59.00													

Ring beam 5

Stress-strain curve (Collins and Mitchel 1991)

Parameters			$f_{c,n}$	f'_c	H_c	ε^e_c	ε^p_c	ε_c
				MPa				days
n	4.73			-2.76	-1			-0.00007
k	1.75		0.00	0.00	0.00	0.0000	0.0000	0
ε_c	0.0025		0.05	3.40	0.02	0.0001	0.0000	0.0001
ε_{cu}	0.0026		0.10	6.81	0.04	0.0002	0.0000	0.0002
			0.15	10.21	0.06	0.0003	0.0000	0.0003
f_{cm28}	66.78	**MPa**	0.20	13.61	0.08	0.0003	0.0001	0.0004
w	2400	**kg**	0.25	17.01	0.10	0.0004	0.0001	0.0005
Ec	34029.86	**MPa**	0.31	20.41	0.11	0.0005	0.0001	0.0006
E_{cm28}	40486.61	**MPa**	0.36	23.81	0.13	0.0006	0.0001	0.0007
	38651.87	**MPa**	0.41	27.19	0.15	0.0007	0.0001	0.0008
f_{tm28}	2.76	**MPa**	0.46	30.56	0.17	0.0008	0.0001	0.0009
ε_t	0.00007		0.51	33.91	0.19	0.0008	0.0002	0.001
			0.56	37.22	0.22	0.0009	0.0002	0.0011
g_r	0.013		0.61	40.49	0.24	0.0010	0.0002	0.0012
g_t	0.0069		0.65	43.69	0.26	0.0011	0.0002	0.0013
g_{ct}	0.043		0.70	46.81	0.29	0.0012	0.0002	0.0014
			0.75	49.82	0.32	0.0012	0.0003	0.0015
fcr	5.15	**MPa**	0.79	52.70	0.36	0.0013	0.0003	0.0016
G_c	52.39	**kPa**	0.83	55.40	0.40	0.0014	0.0003	0.0017
G^p_c	117.83	**kPa**	0.87	57.90	0.44	0.0014	0.0004	0.0018
Gt	0.094	**kPa**	0.90	60.15	0.49	0.0015	0.0004	0.0019
G^e_c	7.86	**kN/m**	0.93	62.13	0.55	0.0015	0.0005	0.002
G^e_c	17.675	**kN/m**	0.96	63.80	0.62	0.0016	0.0005	0.0021
Gt	0.01413	**kN/m**	0.98	65.11	0.71	0.0016	0.0006	0.0022
Leq	0.15	**m**	0.99	66.06	0.80	0.0016	0.0007	0.0023
			1.00	66.78	1.00	0.0016	0.0008	0.0025
			1.00	66.54	1.02	0.0016	0.0009	0.0025
			0.96	63.88	1.22	0.0016	0.0010	0.0026
			0.90	60.21	1.45	0.0015	0.0012	0.0027
			0.83	55.71	1.70	0.0014	0.0014	0.0028
			0.76	50.63	1.97	0.0013	0.0016	0.0029
			0.68	45.26	2.24	0.0011	0.0019	0.003
			0.60	39.86	2.52	0.0010	0.0021	0.0031
			0.52	34.68	2.79	0.0009	0.0023	0.0032
			0.45	29.87	3.05	0.0007	0.0026	0.0033
			0.38	25.54	3.30	0.0006	0.0028	0.0034
			0.33	21.71	3.53	0.0005	0.0030	0.0035
			0.28	18.39	3.75	0.0005	0.0031	0.0036
			0.23	15.55	3.95	0.0004	0.0033	0.0037
			0.20	13.13	4.14	0.0003	0.0035	0.0038
				66.78	0.63	0.0020	0.0005	0.0025

Stress-strain curve (Schütz et al. 2011)

Parameters			$f'_{cy,I}$	$H_{c,I}$	ε^p_c	$f'_{cy,II}$	$H_{c,II}$	ε^p_c	$f'_{cy,III}$	$H_{c,III}$	ε^p_c	$f'_{cy,IV}$	$H_{c,III}$	ε^p_c
			MPa			MPa			MPa			MPa		
f_{c0n}	0.00	0.00	0.00	0.00	0.00000	65.40	1.09	0.00092	12.79	4.53	0.00381	0.00	5.3	0.00444
f_{cfn}	0.20	13.13	1.33	0.01	0.00001	64.02	1.18	0.00099	12.46	4.5	0.00382	0.00	100.0	0.08413
f_{cun}	0.00	0.00	2.64	0.02	0.00002	62.65	1.27	0.00107	12.12	4.6	0.00384			
f_{tun}	1		3.95	0.03	0.00003	61.27	1.36	0.00114	11.78	4.6	0.00386	f_{yt}	H_t	
H_{cf}	4.51		5.24	0.04	0.00003	59.90	1.45	0.00122	11.45	4.6	0.00387	MPa		
H_{cu}	5.28		6.51	0.05	0.00004	58.52	1.54	0.00130	11.11	4.6	0.00389	-2.76	0	
			7.77	0.06	0.00005	57.15	1.63	0.00137	10.77	4.6	0.00391	-2.76	-1	
ε_{cp}	-0.0025		9.02	0.07	0.00006	55.77	1.72	0.00145	10.44	4.7	0.00392			
ε^e_{cp}	-0.0016	**Collins**	10.26	0.08	0.00007	54.40	1.81	0.00152	10.10	4.7	0.00394	$\varepsilon(t)_{cp}$	**t**	
ε^p_{cp}	-0.00084	-0.00084	11.48	0.09	0.00008	53.02	1.90	0.00160	9.76	4.7	0.00396	MPa	Hrs	
ε^p_{cf}	-0.0038	-0.0035	12.69	0.10	0.00008	51.64	1.99	0.00167	9.43	4.7	0.00397	-0.0100	1	
ε^p_{cu}	-0.0044		13.88	0.11	0.00009	50.27	2.08	0.00175	9.09	4.7	0.00399	-0.0016	1.1	
ε^p_{tu}	0.000034	0.000068	15.06	0.12	0.00010	48.89	2.17	0.00182	8.75	4.8	0.00401	-0.0015	1	
	1.0023952		16.23	0.13	0.00011	47.52	2.26	0.00190	8.42	4.8	0.00402	-0.0014	1.3	
A	0.009		17.39	0.14	0.00012	46.14	2.35	0.00198	8.08	4.8	0.00404	-0.0014	1	
B	0.020		18.53	0.15	0.00013	44.77	2.44	0.00205	7.74	4.8	0.00406	-0.0013	1.5	
C	-0.01000		19.66	0.16	0.00013	43.39	2.53	0.00213	7.41	4.8	0.00407	-0.0013	2	
D	0.0202	**t [hrs]**	20.77	0.17	0.00014	42.02	2.62	0.00220	7.07	4.9	0.00409	-0.0011	4	
ε_{1h}	-0.01000	**1**	21.88	0.18	0.00015	40.64	2.71	0.00228	6.73	4.9	0.00411	-0.0011	8	
ε_{8h}	-0.0011	**8**	22.96	0.19	0.00016	39.26	2.80	0.00235	6.40	4.9	0.00412	-0.0010	10	
ε_{24h}	-0.00097	**24**	24.04	0.20	0.00017	37.89	2.89	0.00243	6.06	4.9	0.00414	-0.0010	12	
			25.10	0.21	0.00018	36.51	2.98	0.00251	5.72	4.9	0.00416	-0.0010	24	
G^p_c	17.68	**kN/m**	26.15	0.22	0.00019	35.14	3.07	0.00258	5.39	5.0	0.00417	-0.0010	28	
G^p_t	0.0141	**kN/m**	27.18	0.23	0.00019	33.76	3.16	0.00266	5.05	5.0	0.00419	-0.0009	48	
L_{eq}	0.15	**m**	28.21	0.24	0.00020	32.39	3.25	0.00273	4.71	5.0	0.00421	-0.0009	72	
			29.21	0.25	0.00021	31.01	3.34	0.00281	4.38	5.0	0.00422	-0.0009	96	
f_{cm28}	66.78	**MPa**	30.21	0.26	0.00022	29.64	3.43	0.00288	4.04	5.0	0.00424	-0.0009	120	
E_c	40486.61	**MPa**	31.19	0.27	0.00023	28.26	3.52	0.00296	3.70	5.1	0.00426	-0.0009	144	
f_{tm28}	2.76	**MPa**	32.16	0.28	0.00024	26.89	3.61	0.00303	3.37	5.1	0.00427	-0.0009	168	
ε_t	0.00007		33.11	0.29	0.00024	25.51	3.70	0.00311	3.03	5.1	0.00429	-0.0009	192	
	0.00008		34.06	0.30	0.00025	24.13	3.79	0.00319	2.69	5.1	0.00431	-0.0009	216	
			38.56	0.35	0.00029	22.76	3.88	0.00326	2.36	5.1	0.00432	-0.0009	240	
E_1	13437.177	**MPa**	42.74	0.40	0.00034	21.38	3.97	0.00334	2.02	5.2	0.00434	-0.0009	264	
$f_{c,1}$	6.93	**MPa**	50.08	0.50	0.00042	20.01	4.06	0.00341	1.68	5.2	0.00436	-0.0009	288	
ϕ^{cr}_{∞}	1.21		56.09	0.60	0.00050	18.63	4.15	0.00349	1.35	5.2	0.00437	-0.0009	312	
t^{cr}_{50}	9.00	**days**	60.77	0.70	0.00059	17.26	4.24	0.00356	1.01	5.2	0.00439	-0.0009	336	
t^{shr}_{50}	50	**days**	64.10	0.80	0.00067	15.88	4.33	0.00364	0.67	5.2	0.00441	-0.0009	360	28
$\varepsilon^{shr}_{\infty}$	-0.0002071		66.11	0.90	0.00076	14.51	4.42	0.00372	0.34	5.3	0.00442	-0.0008	672	
E1/Ec	0.3318919		66.78	1.00	0.00084	13.13	4.51	0.00379	0.00	5.3	0.00444	-0.0008	784	
fc1/fc	0.1038378											-0.0008	896	
t_{hyd}	62.00													